



BRNO UNIVERSITY OF TECHNOLOGY

VYSOKÉ UČENÍ TECHNICKÉ V BRNĚ

FACULTY OF MECHANICAL ENGINEERING

FAKULTA STROJNÍHO INŽENÝRSTVÍ

INSTITUTE OF PHYSICAL ENGINEERING

ÚSTAV FYZIKÁLNÍHO INŽENÝRSTVÍ

HYBRID MATERIALS BASED ON MAGNETICALLY BISTABLE MOLECULAR COMPOUNDS

HYBRIDNÍ MATERIÁLY NA BÁZI MOLEKULOVÝCH MAGNETICKY BISTABILNÍCH LÁTEK

MASTER'S THESIS

DIPLOMOVÁ PRÁCE

AUTHOR

AUTOR PRÁCE

Bc. Šárka Vavrečková

SUPERVISOR

VEDOUCÍ PRÁCE

Ing. Ivan Nemeč, Ph.D.

BRNO 2022

Assignment Master's Thesis

Institut: Institute of Physical Engineering
Student: **Bc. Šárka Vavrečková**
Degree program: Physical Engineering and Nanotechnology
Branch: no specialisation
Supervisor: **Ing. Ivan Nemeč, Ph.D.**
Academic year: 2021/22

As provided for by the Act No. 111/98 Coll. on higher education institutions and the BUT Study and Examination Regulations, the director of the Institute hereby assigns the following topic of Master's Thesis:

Hybrid materials based on magnetically bistable molecular compounds

Brief Description:

The use of molecular materials as information carriers in storage media or as qubits in quantum computers has gained a new perspective thanks to the preparation of single-molecule magnets with blocking temperatures higher than the boiling point of liquid nitrogen. For the practical application of such compounds, their deposition in the form of sub-monolayers on functional two-dimensional substrates is necessary. The student's task will be to develop deposition protocols for selected magnetically bistable molecular compounds and to study the prepared hybrid materials by suitable physical methods. The student will be involved in the development of measuring methods for the study of thin films using electron paramagnetic resonance.

Master's Thesis goals:

1. Literature research on the topic of deposition of molecular magnetically bistable compounds and their deposition on "2D" surfaces.
2. Deposition of selected magnetically bistable molecular compounds (for example, single-molecule magnets) on functional "2D" surfaces (for example, graphene).
3. Characterization of all prepared materials by available methods (e.g., Raman spectroscopy, XPS, SEM).
4. Study of selected materials using HF–EPR spectroscopy.

Recommended bibliography:

BADER, Katharina, Dominik DENGLER, Samuel LENZ, Burkhard ENDEWARD, Shang-Da JIANG, Petr NEUGEBAUER a Joris VAN SLAGEREN. Room temperature quantum coherence in a potential molecular qubit. *Nature Communications* [online]. 2014, 5(1), 1-5 [cit. 2021-10-8]. ISSN 2041-1723. Dostupné z: doi:10.1038/ncomms6304

BENELLI, Cristiano a Dante GATTESCHI. Introduction to molecular magnetism: from transition metals to lanthanides. Weinheim: Wiley-VCH, [2015]. ISBN 978-3-527-33540-4.

GUO, Fu-Sheng, Benjamin M. DAY, Yan-Cong CHEN, Ming-Liang TONG, Akseli MANSIKKAMÄKI a Richard A. LAYFIELD. Magnetic hysteresis up to 80 kelvin in a dysprosium metallocene single-molecule magnet. *Science* [online]. 2018, 362(6421), 1400-1403 [cit. 2021-10-8]. ISSN 0036-8075. Dostupné z: doi:10.1126/science.aav0652

MITCOV, Dmitri, Anders H. PEDERSEN, Marcel CECCATO, et al. Molecular multifunctionality preservation upon surface deposition for a chiral single-molecule magnet. *Chemical Science* [online]. 2019, 10(10), 3065-3073 [cit. 2021-10-8]. ISSN 2041-6520. Dostupné z: doi:10.1039/C8SC04917

Abstract

This thesis deals with the deposition of single-molecule magnets on graphene. The theoretical part is devoted to single-molecule magnets, selected deposition methods suitable for depositing single-molecule magnets on two-dimensional substrates, and graphene. Furthermore, the physical principles of the chosen characterization methods (atomic force microscopy, scanning electron microscopy, Raman spectroscopy, X-ray photoelectron spectroscopy and electron paramagnetic resonance) are discussed. In the experimental part, the deposition of six cobalt single-molecule magnets was carried out by thermal sublimation. Two of them were also deposited from solution by drop-casting to verify their high stability. The samples were then analyzed using the methods mentioned above, and the results were discussed. The successful depositions led to the identification of stable single-molecule magnets with promising magnetic properties.

Abstrakt

Tato diplomová práce se zabývá depozicí jednomolekulárních magnetů na grafen. Teoretická část se věnuje jednomolekulárním magnetům, vybraným způsobům depozice jednomolekulárních magnetů na dvourozměrné materiály a grafenu. Dále jsou rozebrány fyzikální principy zvolených charakterizačních metod (mikroskopie atomárních sil, elektronová skenovací mikroskopie, Ramanova spektroskopie, rentgenová fotoelektronová spektroskopie a elektronová paramagnetická rezonance). V praktické části byla provedena depozice šesti kobaltových jednomolekulárních magnetů pomocí termální sublimace. U dvou z nich byla provedena také depozice z roztoku metodou „drop-casting“ k ověření jejich vysoké stability. Poté byly vzorky analyzovány pomocí již výše zmíněných metod a diskutovány výsledky. Díky úspěšným depozicím se podařilo identifikovat stabilní jednomolekulární magnety se slibnými magnetickými vlastnosti.

Keywords

SMM, deposition, graphene, magnetochemistry

Klíčová slova

JMM, depozice, grafen, magnetochemie

VAVREČKOVÁ, Š. *Hybrid materials based on magnetically bistable molecular compounds*. Brno: Brno University of Technology, Faculty of Mechanical Engineering, 2022. 59 p. Supervisor Ing. Ivan Nemeč, Ph.D.

Prohlašuji, že jsem diplomovou práci s názvem "Hybridní materiály na bázi molekulových magneticky bistabilních látek" vypracovala samostatně pod vedením Ing. Ivana Nemce, Ph.D. a že veškerou použitou literaturu a ostatní zdroje uvádím v seznamu literatury.

V Brně dne 19. 5. 2022

Bc. Šárka Vavrečková

This work could not have been undertaken without the excellent supervision and comments on the thesis by Ing. Ivan Nemeč, Ph.D. Special thanks should also go to Ing. Jakub Hrubý, Ph.D., who introduced me to deposition and helped me, especially with XPS and SEM measurements in the beginning of my work. I am also grateful to Ing. Lubomír Havlíček and Mgr. Ondřej Fellner for synthesizing the compounds and providing the VSM measurements. Thanks should also go to colleagues from the MOTES group who helped me with EPR measurement. Lastly, I would like to thank my family, friends, cat and cacti for their emotional support.

This work was supported by the research infrastructure CzechNanoLab (ID LM2018110, MŠMT, 2020–2022), CEITEC Brno University of Technology and The Sublimable Single-Molecule-Magnets for Preparation of Nanostructured Thin Films project funded by GAČR Standard (22-23760S).

Bc. Šárka Vavrečková

Contents

1	Introduction	1
2	Theoretical part	2
2.1	Single-molecule magnets (SMMs)	2
2.1.1	Brief history and current state of the art	3
2.2	Deposition methods	4
2.2.1	”Wet” chemistry	4
2.2.2	Thermal sublimation	5
2.2.3	Electrospray deposition	5
2.3	Graphene	6
2.3.1	Graphene bolometer	7
2.4	Characterization methods	8
2.4.1	Atomic force microscopy (AFM)	8
2.4.2	Scanning electron microscopy (SEM)	10
2.4.3	Raman spectroscopy	10
2.4.4	X-ray photoelectron spectroscopy (XPS)	12
2.4.5	Electron paramagnetic resonance (EPR)	14
3	Experimental part	16
3.1	Measurement parameters	16
3.2	Substrate	17
3.3	Deposition	18
3.4	Compound (1a)	19
3.5	Compound (1b)	23
3.6	Compound (2a)	27
3.7	Compound (2b)	32
3.8	Compound (3a)	37
3.9	Compound (3b)	41
4	Conclusions	45
5	Attachments	53
5.1	Synthesis	53
5.2	VSM measurements	54
5.3	TGA measurements	57

1. Introduction

Three decades have passed since the discovery of the first single-molecule magnet, the Mn_{12} -ac molecule, by R. Sessoli's team in the 1990s, and several hundred others have seen the light of day [1, 2]. Even so, their behavior on surfaces is still an unexplored area. These molecules exhibit magnetic hysteresis of purely molecular origin below a certain blocking temperature. With the recent achievement of raising the blocking temperature above the boiling point of liquid nitrogen, molecular magnets are becoming increasingly promising in the field of magnetic data storage, molecular spintronics, or quantum computing [3, 4, 5].

The second challenge is to find a way to transfer bulk material to functional surfaces. Current efforts are focused on creating thin layers, ordered arrays, or self-organized monolayers that will lead to technological applications [6]. Understanding the behavior and adsorption of complex molecules on surfaces is crucial, as many problems occur during deposition processes, such as decomposition, oxidation or degradation under ambient conditions.

The single-molecule magnet consists of central atoms surrounded by organic ligands. An analog with only one paramagnetic center is referred to as a single-ion magnet (SIM). One of the promising groups is Co(II)-based SIMs because of large magnetic anisotropies, as well as they can be easily chemically modified to influence their magnetic properties [7]. Therefore, the six different Co(II)-based SIMs with bidentate ligands are investigated in terms of deposition on surfaces in this thesis. Graphene was chosen as a substrate, which is suitable for use in electrical addressing or as a detector in electron paramagnetic resonance, where it could allow more sensitive measurements of magnetic properties directly on the surface [8].

The theoretical part describes the nature of the behavior of single-molecule magnets, their brief history, and methods of deposition. The structure and properties of graphene are also described, and the motivation for its use is explained. In addition, the physical principles of characterization methods such as atomic force microscopy (AFM), scanning electron microscopy (SEM), Raman spectroscopy, photoelectron spectroscopy (XPS), and electron paramagnetic resonance (EPR) are introduced.

The experimental part is devoted to the fabrication and characterization of samples consisting of - CVD graphene on silicon dioxide and a layer of SIMs. The deposition was performed by thermal sublimation and drop-casting. The aim of the thesis is to perform a successful deposition and then characterize the prepared samples in terms of morphology (AFM, SEM), chemical composition (XPS, Raman spectroscopy), and magnetic properties (EPR).

2. Theoretical part

The theoretical part contains properties of single-molecule magnets, deposition methods, and information about graphene. Further, the physical principles of the selected characterization methods (atomic force microscopy, electron scanning microscopy, Raman spectroscopy, X-ray photoelectron spectroscopy and electron paramagnetic resonance) are described.

2.1. Single-molecule magnets (SMMs)

SMMs are coordination complexes of transition metals, or lanthanides or actinides, consisting of central atoms (e.g., Co, Mn, Fe, Cu, Gd, Er, Tb, Dy), which are surrounded by organic ligands. If a molecule contains one paramagnetic central atom, it is called single-ion magnet (SIM). SMMs, like macroscopic magnets, exhibit high magnetic anisotropy, which means that the magnetization depends on the direction of the external magnetic field. When the external magnetic field is applied along the "easy" axis of magnetization, magnetization is most easily achieved. SMMs show a slow relaxation of magnetization and magnetic hysteresis of purely molecular origin at temperatures lower than the so-called blocking temperature T_b . [2]

The magnetic behavior of SMMs is controlled by anisotropic parameters of energy level splitting in zero magnetic field - Zero Field Splitting (ZFS), and is described using the spin Hamiltonian in the form

$$\hat{H} = D[\hat{S}_z^2 - S(S + 1)/3] + E(\hat{S}_x^2 - \hat{S}_y^2), \quad (2.1)$$

where D is the parameter of axial magnetic anisotropy, E rhombicity, S total spin quantum number and S_x , S_y , S_z are spin projections to individual axes of the Cartesian coordinate system. According to the value of D we distinguish two basic types of magnetic anisotropy: 1. $D < 0$ - magnetization of molecules is in the direction of the "easy" magnetization axis, 2. $D > 0$ - magnetization of molecules is in the direction perpendicular to "easy" magnetization axis. The characteristic behaviour of SMMs is the most often observed for compounds possessing axial type of magnetic anisotropy ($D < 0$). The process of magnetization and relaxation is usually illustrated by a double potential well (shown in Fig. 2.1) with an effective energy barrier of size

$$U_{\text{eff}} = |D|S^2 \quad (2.2)$$

for molecules with an integer total spin, and

$$U_{\text{eff}} = |D|(S^2 - 1/4) \quad (2.3)$$

for molecules with non-integer total spin. The double well contains $2S + 1$ levels, which are characterized by the spin quantum number m_S , where $-S \leq m_S \leq S$. In zero field, $\pm m_S$ levels represent degenerate pairs, and these wells are equally populated by unpaired spins of the molecules. When a magnetic field is applied, the spins align in its direction, leading to stabilization of the $-m_S$ and destabilization of the $+m_S$ levels (Zeeman effect - explained in Section 2.4.5). When the field is removed, the spin must overcome the energy barrier U_{eff} to reverse the magnetization. At temperatures lower than the T_b ,

the magnetization will persist for a certain time. The higher the barrier, the longer the magnetization persists. [2]

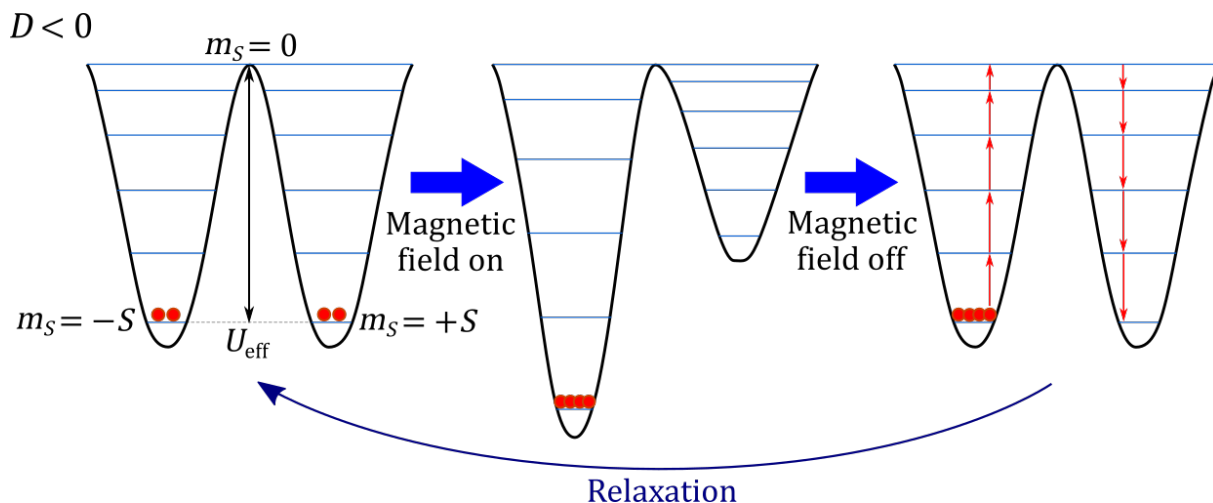


Fig. 2.1: Schematic diagram of magnetization and relaxation of magnetization of SMMs. Inspired from [9].

As already mentioned, SMMs exhibit magnetic hysteresis at temperatures lower than T_b (in the order of tens of Kelvins) and can preserve its magnetization for years [10]. Such a phenomenon makes SMMs interesting in terms of magnetic memory [1]. One molecule, which would represent one bit, is of nanometre size. Therefore, the storage density would be significantly higher than current technologies. SMMs can also be used in molecular spintronics or due to quantum behavior in quantum computing as quantum bits called qubits [4, 5]. In contrast to the classical bit, which takes values 0 and 1, qubit uses the superposition of these two states.

2.1.1. Brief history and current state of the art

Magnetic behavior of the first single-molecular magnet $[\text{Mn}_{12}\text{O}_{12}(\text{O}_2\text{CCH}_3)_{16}(\text{H}_2\text{O})]$ (shown in Fig. 2.2b), shortly $\text{Mn}_{12}\text{-ac}$, was observed by R. Sessoli and co-workers in 1993 [1]. Magnetic measurements of this $\text{Mn}^{\text{III}}/\text{Mn}^{\text{IV}}$ cluster revealed a slow relaxation of magnetization and magnetic hysteresis below $T_b \approx 3$ K, with $S = 10$, $D = -0.51$ cm^{-1} resulting in $U_{\text{eff}} = 51$ cm^{-1} (73.4 K) [1]. With regard to applicability, the aim was to increase U_{eff} and T_b . With respect to equations 2.2 and 2.3, it was assumed that increasing S value would increase the U_{eff} . Therefore, it was an effort to prepare SMMs with more paramagnetic centers. However, this assumption proved to be uncorrect, as SMMs with higher S values showed poorer magnetic properties in terms of U_{eff} and T_b . For example, $\text{Mn}^{\text{II}}_7\text{Mn}^{\text{III}}_{12}$ cluster with record $S = 83/2$ exhibited $U_{\text{eff}} = 4$ cm^{-1} (5.8 K) [11].

It has been reported that D depends on S as $D \propto 1/S^2$ [9]. This dependence has shifted the interest from relatively large molecules with many central atoms to their analogues with only one paramagnetic center, SIMs. The first SIMs, which were phthalocyanine double-decker lanthanide (Tb and Dy) complexes, were prepared in 2003 and exhibited $U_{\text{eff}} = 230$ cm^{-1} and $T_b = 1.7$ K [12]. These results led to a shift in research direction to Ln-based SIMs. In addition, the focus has also shifted to SIMs based on 3d and 4f transition metals, with the first one being a trigonal pyramidal complex of Fe(II) prepared in 2011 [13]. Although these complexes do not show such high U_{eff} and T_b values, their

2.2. DEPOSITION METHODS

simplicity allows us to better understand the magnetic behaviour and then apply this knowledge to more complex systems.

An important milestone in terms of increasing the T_b occurred in 2018 when a dysprosium metallocene (illustrated in Fig. 2.2b) was prepared, that exhibited a $T_b = 80$ K, and also exceptionally high $U_{\text{eff}} = 1541$ cm⁻¹ [3]. This temperature exceeding the boiling point of liquid nitrogen (77 K) is a great promise for potential applicability.

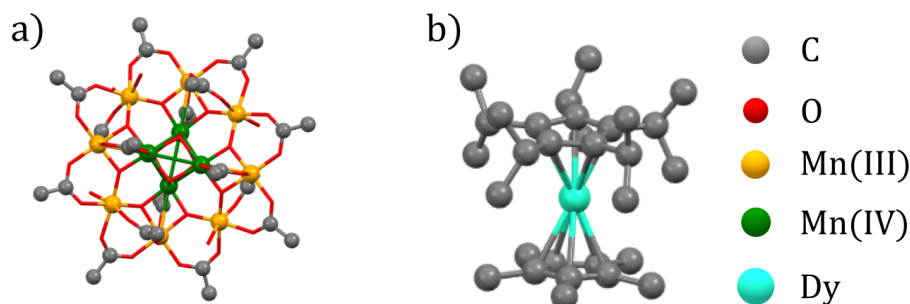


Fig. 2.2: Chemical structure of the first SMM Mn₁₂-ac, and SMM with the highest T_b dysprosium metallocene. Reproduced from [14] and [3].

2.2. Deposition methods

SMMs are synthesized in the form of crystalline powder, which is not suitable for applications. In order to explore their application potential, it is suitable to make films and patterns. Therefore the ability to transfer SMM on substrates is crucial. The most common methods are described in the following paragraphs.

2.2.1. "Wet" chemistry

The basis of the "wet" chemistry transfer is a solution of a complex and a solvent. Solution is applied to the substrate, and the solvent evaporates. The most straightforward way of the application is so-called drop-casting shown in 2.3. Its principle consists in dropping the solution by pipette onto the substrate. It can be carried out either under ambient conditions or inert (protective) atmosphere (glove-box with Ar or N₂) if the complex is reactive. Spin-coater can be used for obtaining thinner and more homogeneous layers. [15]

This method was used in the experimental part of this thesis. The advantages of this method are speed, financial availability, room temperature performance (no risk of decomposition due to high temperatures) and the possibility of covering larger areas, as we are limited only by the size of the glove-box. The disadvantage may be the inability to control the thickness of the layer accurately.

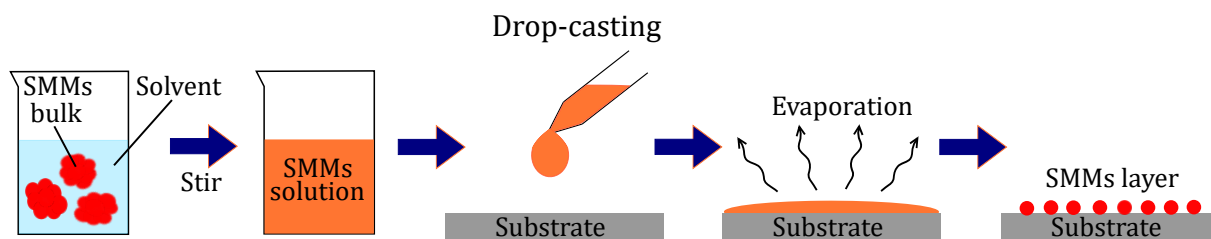


Fig. 2.3: Principle of the drop-casting method.

Another way how to make thin films using "wet" chemistry is the dip-and-dry technique. The substrate is dipped into the solution and immediately removed, causing a thin layer of solution to form on the surface. Solvent evaporates, and solid thin films of SMMs are obtained. Homogeneous and ultra-thin films in order of a few molecular monolayers can be obtained. [16]

Another more sophisticated "wet" chemistry method is the Langmuir-Blodgett (LB) method shown in Fig. 2.4b. The substrate is immersed in the liquid, which is in a trough with movable barriers. A layer of SMMs is placed on the surface of the liquid. By using the holder, the substrate emerges in a controlled manner, and the barriers control the concentration of the SMMs molecules adhering to the sample. With each successive dipping and surfacing, another layer is applied. An analog of the LB method is the Langmuir-Schaefer (LS) method, where the immersed sample is oriented parallel to the liquid surface. [17]

Solution-based methods were successfully used to transfer molecules to surface, for example $\text{Mn}_{12}\text{-ac}$: [15, 17, 18].

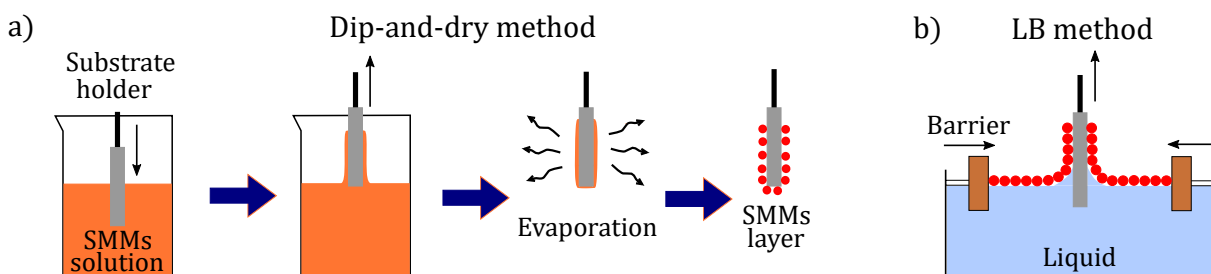


Fig. 2.4: Principle of the dip-and-dry method on the left and LB method on the right.

2.2.2. Thermal sublimation

The cleanest deposition method is thermal sublimation in ultra-high vacuum (UHV) [19]. The principle is shown in 2.5b. Crucible is filled with SMMs powder, placed in a UHV vacuum chamber, and heated by a ceramic heater whose temperature is monitored by a thermocouple. SMMs molecules sublime, leave the crucible and form a layer onto a substrate attached to the sample holder. The thickness of the layer is determined by quartz crystal microbalance (QCM), which measures the change in frequency of oscillation due to the mass change caused by the adhesion of molecules [20].

This method was used in the experimental part of this thesis. Compared to the drop-cast method, we are able to monitor the growth rate and thus a specific required thickness. However, this method is more demanding in terms of instrumentation and time.

2.2.3. Electrospray deposition

Another successful method for UHV deposition is electrospray deposition [21]. The schematic principle is shown in Fig. 2.5a. The SMMs solution flows through an emitter capillary, where the high voltage is applied. Under the influence of the electric field, droplets with a high surface charge are emitted into the vacuum. As the solvent evaporates, the surface charge density increases. If it reaches a critical value, a so-called Coulombic explosion occurs, i.e., the splitting into smaller droplets. The process repeats, forming smaller and smaller droplets until they reach the sample. [22]

2.3. GRAPHENE

This method is used for molecules that are not suitable for thermal sublimation due to their decomposition at lower than sublimation temperatures, as it can be carried out at room temperature.

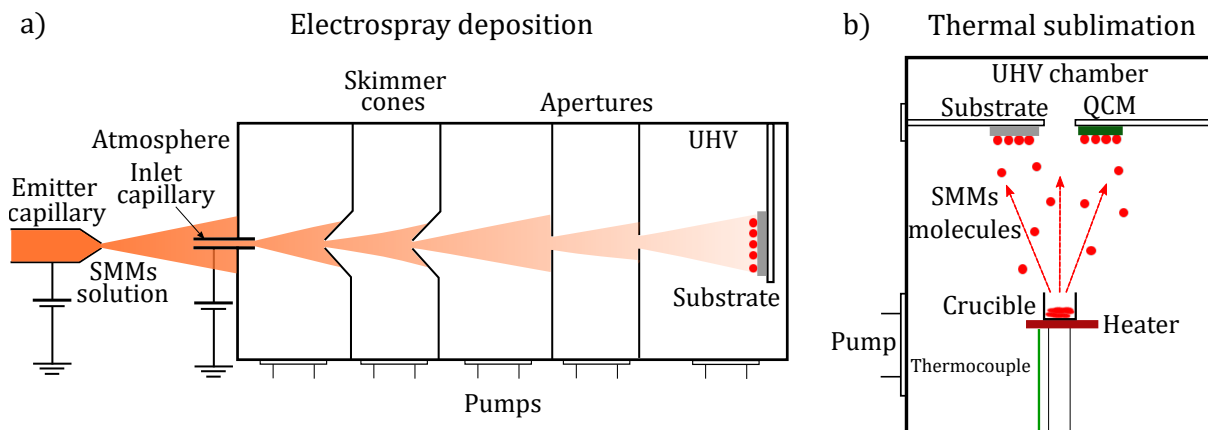


Fig. 2.5: Principle of the a) electro spray deposition (inspired by [22]) and b) thermal sublimation method.

There are a number of other less used deposition methods whose principle would be beyond the scope of this thesis. The curious reader can read more about them, for example, here: [16], [23].

2.3. Graphene

SMMs on surface can be electrically addressed by a conductive substrate. A promising candidate is a graphene, which is an interesting two-dimensional material whose properties are described in this chapter.

Two-dimensional (2D) materials are defined as substances consisting of a single layer of atoms. Graphene was the first experimentally obtained 2D material in 2004 by K. Novoselov¹ and A. Geim¹ at the University of Manchester [24]. It is an allotrope of carbon formed of hexagonally arranged carbon atoms. The primitive unit cell is composed of two carbon atoms, A and B, which are 1.42 Å apart. Carbon atoms have four valence electrons, where three of them (located in 2s, 2p_x, 2p_y valence orbitals) are involved in σ covalent bonds with the three nearest atoms. The remaining valence electron is in a 2p_z orbital, which would participate in a weak π bond perpendicular to the σ bond plane. The 2p_z orbitals from adjacent atoms hybridize and form π (valence) or π^* (conduction) bands, as shown in Fig. 2.6b) of the graphene band structure. The valence and conduction bands touch at points K and K' (known as Dirac points), which are the hexagon corners of the first Brillouin zone of the reciprocal lattice. Close to the Dirac point, the band structure has a Dirac cone shape, resulting in graphene's unique electronic properties. [25]

¹2010 The Nobel Prize in Physics “for groundbreaking experiments regarding the two-dimensional material graphene”

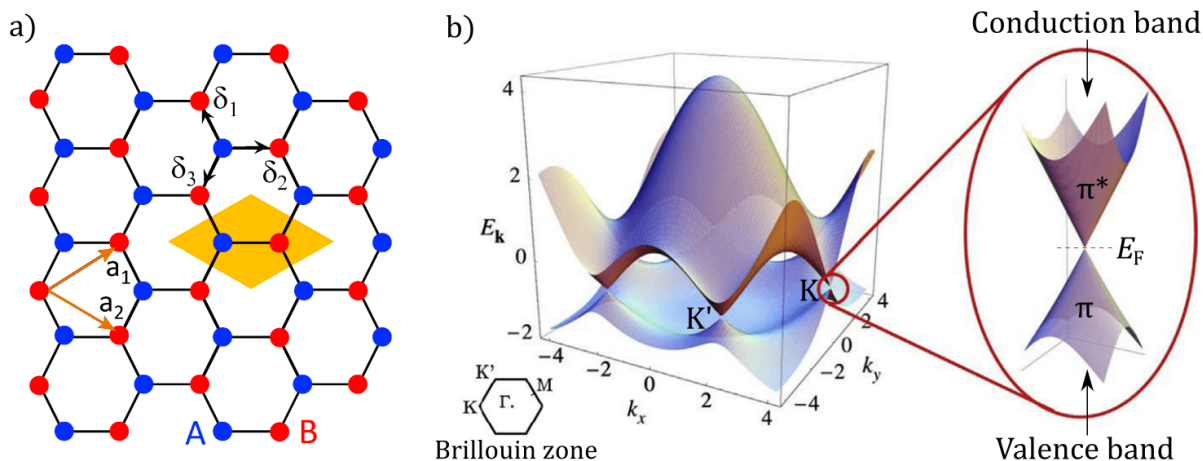


Fig. 2.6: a) The lattice of graphene consists of two atoms (A and B). The primitive unit cell is marked in yellow, primitive lattice vectors in orange, and the vectors connecting adjacent carbon atoms in black. b) Graphene band structure showing valence and conduction bands. On the right: zoom in on the energy bands close to one of the Dirac points. Adapted from [26, 25].

In intrinsic graphene, the valence band meets the conduction band at the Fermi level E_F , so graphene is considered a zero band gap semiconductor. Room-temperature electron mobility of $2.5 \times 10^5 \text{ cm}^2 \text{V}^{-1} \text{ s}^{-1}$ is the highest of all materials [27]. With heat conductivity above $3000 \text{ Wm}^{-1} \text{K}^{-1}$ it is excellent heat conductor [28]. Graphene can absorb radiation of all frequencies of the electromagnetic spectrum. One layer absorbs 2.3 % of the light, so it appears transparent [29]. Because of the strong carbon covalent bonds, graphene with Young's modulus of 1 TPa and intrinsic strength of 130 GPa is the second strongest material after another 2D material, borophene [30, 31].

These characteristics (especially the zero band gap, which is not suitable for some applications - e.g., transistor), however, can be affected by various defects in the crystal structure, external electromagnetic field, doping, substrate, or a number of layers [32]. Graphene quality can be examined by Raman spectroscopy or atomic force microscopy [33].

Since 2004, when graphene was first isolated by mechanical exfoliation of graphite, other widely used methods for its preparation have been developed [32]. These differ mainly in quality, size of the graphene produced, and cost. In terms of cost for mass production and quality of graphene, chemical vapor deposition (CVD) is worth mentioning [34]. It allows the preparation of high-quality graphene with an area of the order of cm^2 . Current CVD technologies use metallic (often copper) substrates to grow graphene. The graphene thus prepared must then be transferred to the desired substrate, which is most often Si with a SiO_2 layer. The oxide layer thickness of $\approx 300 \text{ nm}$ makes the graphene visible in the optical region, which simplifies further work with the sample [36].

2.3.1. Graphene bolometer

This thesis was carried out within a group MOTES CEITEC (Magneto-Optical and THz Spectroscopy) that also focuses on electron paramagnetic resonance (EPR; explained in chapter 2.4.5), which is based on the absorption of electromagnetic radiation. One of the research directions of the group and its partners is a new generation of graphene-based bolometers that can be used as a detector in EPR spectrometer [8, 37].

2.4. CHARACTERIZATION METHODS

A bolometer is a device that works on the principle of measuring the change in resistance with changing temperature on the bolometer chip, which is caused by the absorption of radiation. A schematic of such a device can be seen in Fig. 2.7a. Graphene in the shape of a bowtie with a quantum dot in the middle is placed on silicon carbide (SiC). As can be seen from Fig. 2.7b, such arrangement exhibits a very high variation of electrical resistance with temperature (higher than $430 \text{ M}\Omega \text{ K}^{-1}$ below 6 K), which leads to much higher sensitivity than commercially cooled bolometers [37].

SMMs layer can be deposited directly on a graphene bolometer, which makes the bolometer an ideal tool for characterizing and studying SMMs on surfaces.

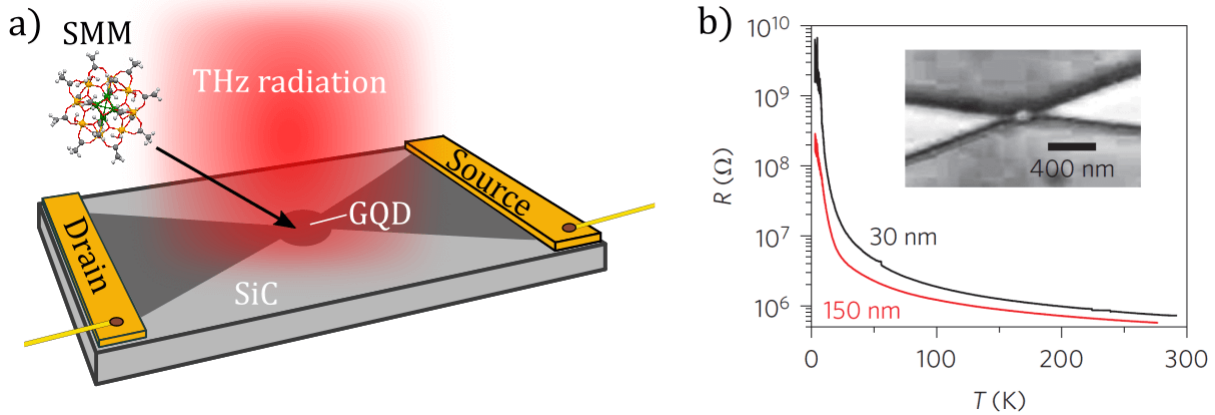


Fig. 2.7: a) Scheme of the graphene quantum dot (GQD) bolometer with SMM on its surface. b) Resistance versus temperature for two quantum dots with different diameters. Inset: scanning electron microscopy image of a typical graphene quantum dot. Adapted from [8, 37].

2.4. Characterization methods

The following section presents the physical principles of the methods used to characterize SMM's films on graphene in the experimental part. Atomic force microscopy (AFM) and scanning electron microscopy (SEM) were used for topography, Raman spectroscopy for vibration studies, X-ray photoelectron spectroscopy (XPS) for elemental representation on the surface and bond analysis, and electron paramagnetic resonance (EPR) for magnetic properties.

2.4.1. Atomic force microscopy (AFM)

Atomic force microscopy is mainly used to study the topography of samples with resolution more than $1000\times$ higher than classical optical microscope [38]. It was first implemented in 1986 by G. Binnig², C.F. Quate and Ch. Gerber [39]. The principle of this method is to map the attractive and repulsive forces between the atoms on the surface of the sample and the atoms of the sharp tip. The tip is mounted on a flexible cantilever which is deflected by these interactions. The deflection of the cantilever is detected by a laser beam that points on the tip of the cantilever and is reflected onto a sensitive photodiode,

²1986 The Nobel Prize in Physics “for the design of the scanning tunneling microscope” (The precursor to the AFM)

which is divided into four quadrants. When the cantilever is in the equilibrium position, the measured intensity of the incident laser beam is the same in each quadrant. If the cantilever is deflected, the laser beam moves from the center, and the intensity measured in each quadrant is different. The arrangement is illustrated in Fig. 2.8a.

Depending on the distance of the tip from the surface, either repulsive or attractive interactions predominate. These are often approximated by the so-called Lennard-Jones potential

$$\omega(r) = 4\omega_0 \left[\left(\frac{\sigma}{r} \right)^{12} - \left(\frac{\sigma}{r} \right)^6 \right], \quad (2.4)$$

where r is the distance between the tip and surface atoms, σ is the equilibrium distance between the atoms, and ω_0 is the minimum potential energy. The relation for the applied force is obtained by taking the negative derivative of the potential by r as

$$F(r) = -\frac{d\omega(r)}{dr} = 24\omega_0 \left[\left(\frac{2\sigma^{12}}{r^{13}} \right) - \left(\frac{\sigma^6}{r^7} \right) \right]. \quad (2.5)$$

Repulsive forces (a consequence of Pauli exclusion principle) are proportional to r^{-13} and attractive forces (van der Waals forces) are proportional to r^{-7} . Fig. 2.8b shows the dependence of the Lennard-Jones potential $\omega(r)$ and the force $F(r)$ acting between atoms. For the force curve, the force above the axis is repulsive and below the axis is attractive. At a distance of r_e the potential minimum is reached and the resulting force is zero. The measurement modes are also indicated in the figure. [40]

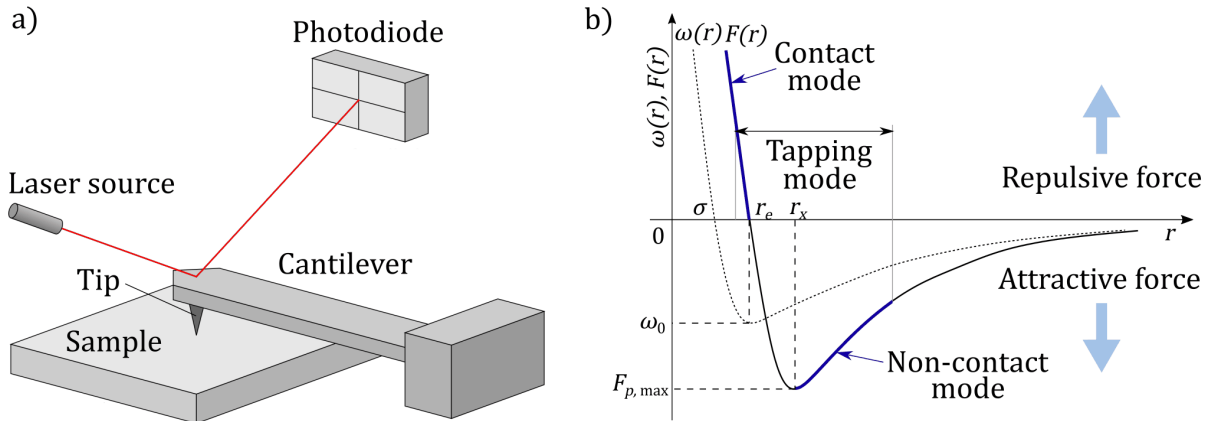


Fig. 2.8: a) Basic principle of the AFM. b) Dependence of Lennard-Jones potential and force F on the distance r of two particles. The regions of action of the different measurement modes are also shown. Adapted from [41].

Measurement modes

Depending on the distance of the tip from the surface and the dominant forces, AFM measurements are divided into three modes: contact, non-contact and tapping. The tapping mode was used in the experimental part of this thesis. This mode combines contact and non-contact modes, that is, the cantilever oscillates at a resonant frequency above the sample and occasionally touches the surface. By monitoring changes of frequency and amplitude, the surface of the sample can be determined. It attempts to compensate for sample damage and resolution. [42]

2.4. CHARACTERIZATION METHODS

2.4.2. Scanning electron microscopy (SEM)

Scanning electron microscopy is an imaging method that uses electrons instead of photons. Because the resolution is directly dependent on the wavelength, electrons with a wavelength much shorter than the wavelength of the photons in the visible spectrum provide much greater magnification. In 1924, L. de Broglie³ stated the hypothesis about the wave nature of matter [43]. According to the de Broglie hypothesis, the wavelength of the electron is related to momentum as

$$\lambda = \frac{h}{p} = \frac{h}{m_e v} = \frac{h}{\sqrt{2m_e eU}}, \quad (2.6)$$

where λ is the wavelength, h is the Planck's constant, m_e is the mass of the particle, v is its velocity, e elementary charge and U accelerating voltage used in SEM chamber. This relationship is valid only for non-relativistic particles [44]. Taking into account the typical accelerating voltage $U = 30$ keV, the wavelength of the electron is $\lambda = 0.0073$ nm. In contrast, the photon wavelength used in optical microscope is approximately $\lambda = 360$ – 700 nm. With respect to aberrations, SEM can provide sub-nanometer resolution, while optical can provide a maximum of 200 nm [44, 45].

The first SEM was developed by V. Zworykin in 1942 [46]. A typical arrangement of a current SEM is shown in Fig. 2.9a. The surface of the sample is scanned with an electron beam. The electrons interact with the atoms of the sample to produce different types of signal, which provide specific information about the sample (see Fig. 2.9b). These are: secondary electrons, backscattered electrons, Auger electrons and X-rays. Secondary electrons, which carry information about its topography, are most often detected.

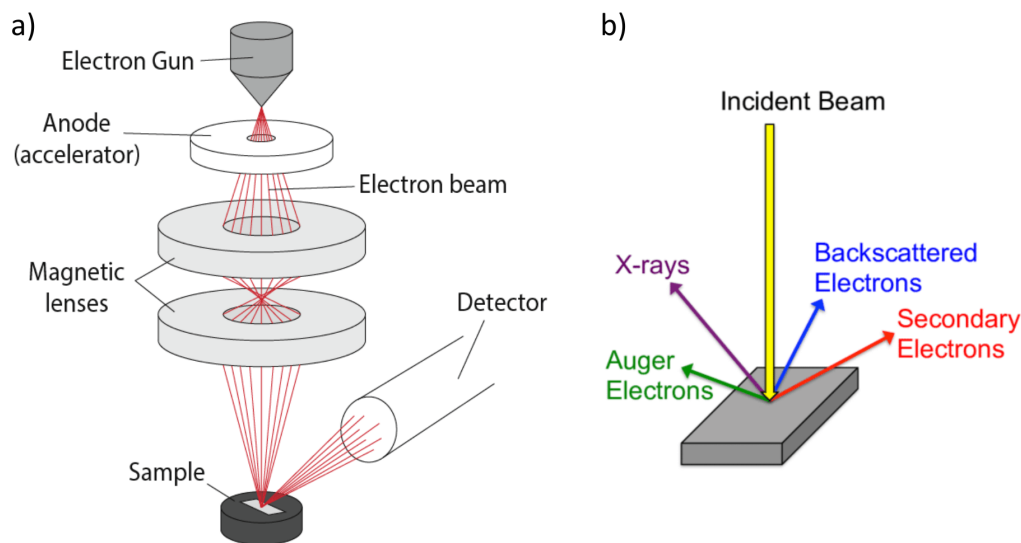


Fig. 2.9: a) Schematic illustration of SEM. b) Electron beam interaction with the sample. Taken from [47, 48].

2.4.3. Raman spectroscopy

Raman spectroscopy is a non-destructive method for investigating the composition and structure of substances. As the name suggests, the basis of the method is Raman scat-

³1929 The Nobel Prize in Physics “for his discovery of the wave nature of electrons”

tering (inelastic light scattering). It is named after the Indian physicist Ch. V. Raman⁴, who first observed it with his collaborator K. S. Krishnan in 1928 [49].

When the laser beam hits the sample, the elastic or inelastic scattering of photons can occur (see Fig. 2.10a). Elastic scattering is much more common, in which the incident photon transfers energy to an electron, which is excited to a higher energy level. Subsequently, the electron relaxes (de-excites) to its original energy level and a photon of the same energy (same wavelength) as the incident photon is emitted. This scattering is known as Rayleigh scattering and provides no analytical information in the Raman spectrum. Inelastic scattering occurs when an electron also excites to a higher energy level, here interacts with a molecular vibrations (schematically in the figure: vibration with frequency Ω), deexcites to a different energy level than the original, and a photon with a different wavelength than the incident photon is emitted. If the electron returns to a higher energy level than the original, the scattered photon has a lower energy (longer wavelength). This scattering is called Stokes scattering. Conversely, when the electron returns to a lower energy level than the original, the scattered photon has a higher energy (shorter wavelength) and the scattering is called anti-Stokes scattering. Because the electron is excited to so-called virtual levels that are not stable, the subsequent relaxation occurs immediately, and this phenomenon does not depend on the wavelength of the incident radiation. From the law of conservation of energy, the difference in energy of the incident and scattered photon corresponds to the appearance or disappearance of a phonon, which is reflected in a change in the vibrational state of the molecule. [50]

The Raman spectrum thus consists of symmetrically placed peaks relative to the peak of elastic scattering of radiation with frequency λ_0 (see Fig. 2.10b).

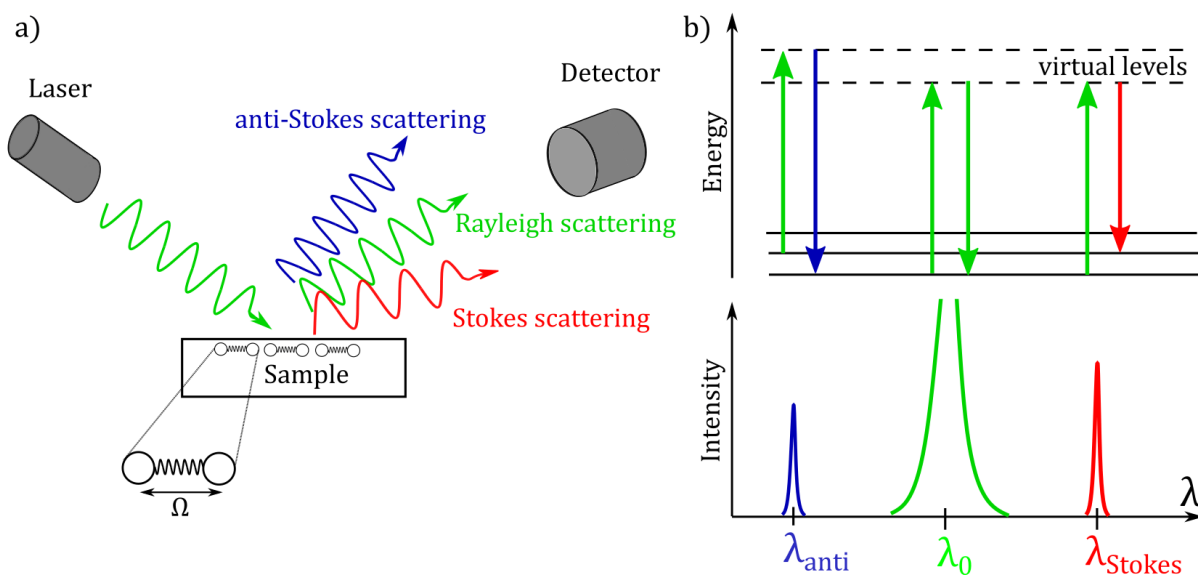


Fig. 2.10: a) Scattering of the laser beam. b) Diagram of the energy transitions of the excited electron and corresponding peaks in Raman spectrum.

The higher wavelength region is called the Stokes branch and the lower wavelength region the anti-Stokes branch of the Raman spectrum. In practice, Raman spectra are plotted as the dependence of the Raman shift (the difference in reciprocal wavelength

⁴1930 The Nobel Prize in Physics “for his work on the scattering of light and for the discovery of the effect named after him”

2.4. CHARACTERIZATION METHODS

of the incident and scattered radiation) on the intensity of the signal, and usually the spectrum of the Stokes branch of the Raman spectrum is measured, since it has a slightly higher intensity. The positions of these peaks give us information about the nature of the bonds in the molecule. Since each substance has its own characteristic spectrum, it can be considered as a chemical fingerprint [51]. Raman spectroscopy also plays an important role in the characterization of graphene. It can be used to determine, for example, the number and orientation of layers, defects or dopants [33].

2.4.4. X-ray photoelectron spectroscopy (XPS)

X-ray photoelectron spectroscopy (XPS), often referred to as ESCA (Electron Spectroscopy for Chemical Analysis), is a widely used method for determining the chemical composition of the surface of a solid. The basis of this method is the photoelectric effect, which was first observed by H. Hertz in 1887. The explanation of this phenomenon by quantization of the energy of electromagnetic radiation was given by A. Einstein⁵ in 1905 [52]. The method itself was developed in the 1960s by a research group led by K. Siegbahn⁶ at Uppsala University [53].

XPS involves irradiating the sample with an X-ray beam of specific wavelength that penetrates to a depth of tens of nanometres below the surface, depending on the instrument settings. In this region, photons interact with atoms and cause the emission of electrons due to photoelectric effect. The emitted electrons have kinetic energy

$$E_k = h\nu - E_b - \phi_s, \quad (2.7)$$

where $h\nu$ is the energy of the incident electromagnetic radiation (h is Planck's constant and ν frequency), E_b is the binding energy of the electron relative to the Fermi level, and ϕ_s is the output work, which expresses the energy required to release the electron from the Fermi level to the vacuum level. The course of the photoelectric effect is shown in Fig. 2.11. [53]

In the photoelectron spectrum there are also often so-called Auger peaks, which are the result of the Auger effect (see Fig. 2.11). When an electron is knocked out of the inner level during a photoelectric effect, an electron from a higher level replace its place. This releases energy, which can be emitted as a photon or can be passed to another electron. Electrons emitted in this way are called Auger electrons.

⁵1921 The Nobel Prize in Physics “for his services to theoretical physics, and especially for his discovery of the law of the photoelectric effect”

⁶1981 The Nobel Prize in Physics “for his contribution to the development of high-resolution electron spectroscopy”

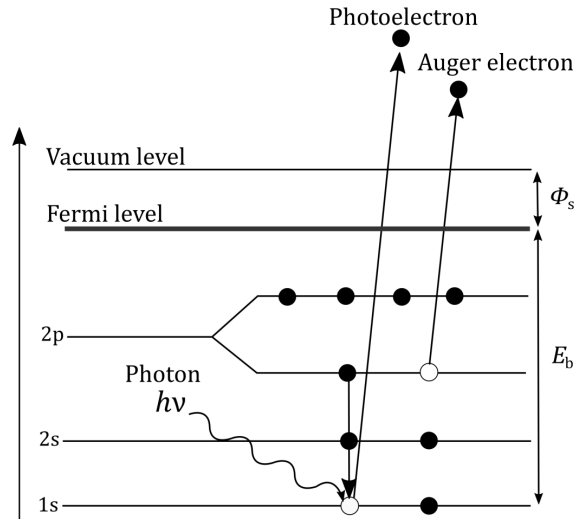


Fig. 2.11: Photoelectric and Auger effect.

Typical X-ray photoelectron spectrometer configuration is shown in Fig. 2.12. Kinetic energy distribution of the photoelectrons is measured by hemispherical analyzer. From the knowledge of the kinetic energy we are then able to obtain the value of the binding energy. The result is a photoelectron spectrum containing photoelectron lines (peaks) from whose position, intensity and shape we can obtain information about the chemical nature of the atoms.

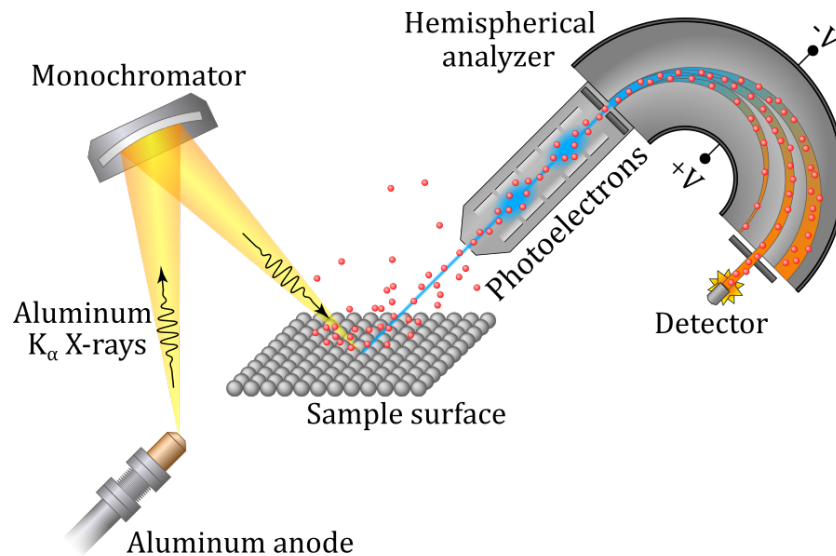


Fig. 2.12: Scheme of XPS instrumentation. Adapted from [54].

This method can be used for non-destructive surface analysis. Since each element has characteristic binding energy values, this method provides information on the qualitative composition of the sample surface. Using quantitative analysis of peak intensities, we are even able to determine the concentration of elements. XPS can also distinguish between differently bonded atoms of the same element because they cause a measurable shift of the lines (called chemical shift).

2.4. CHARACTERIZATION METHODS

2.4.5. Electron paramagnetic resonance (EPR)

The electron paramagnetic resonance method is based on the absorption of electromagnetic radiation by a material containing at least one unpaired electron. The first EPR measurement was made by the Russian physicist J. K. Zavoisky in 1944. To understand it, it is important to explain the following phenomena. [55]

Zeeman effect

If the system is exposed to an external non-zero magnetic field B , the degenerate levels split according to the spin quantum number. For simplicity, Fig. 2.13 shows the Zeeman effect for a free electron. This electron at a given level has potential energy

$$E = m_s g_e \mu_B B, \quad (2.8)$$

where g_e is the g -factor of the free electron and μ_B Bohr's magneton. The difference of energies of these levels follows a resonant condition, which describes what energy the incident photon must have in order for the excitation of the electron to take place:

$$\Delta E = g_e \mu_B B = h\nu, \quad (2.9)$$

where h is Planck's constant and ν frequency of the photon.

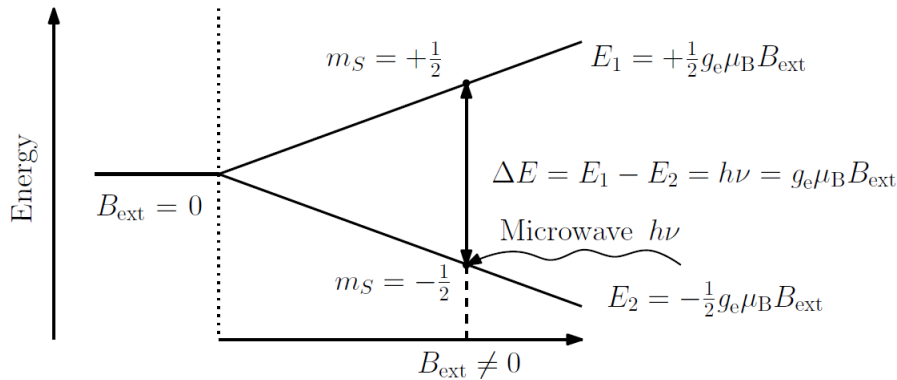


Fig. 2.13: Representation of Zeeman effect for free electron. Taken with permission of my colleague Ing. Jakub Hrubý, Ph.D. [56].

Zero field splitting (ZFS)

A system with $n > 1$ unpaired electrons has spin $S = n/2$, and $2S + 1$ energy levels characterized by the spin quantum number m_S . If no external magnetic field acts on the system, the m_S and $-m_S$ levels are degenerate. Individual levels differing in $|m_S|$ split, so they have energy gaps between them. Spin Hamiltonian of such system was introduced in chapter 2.1.

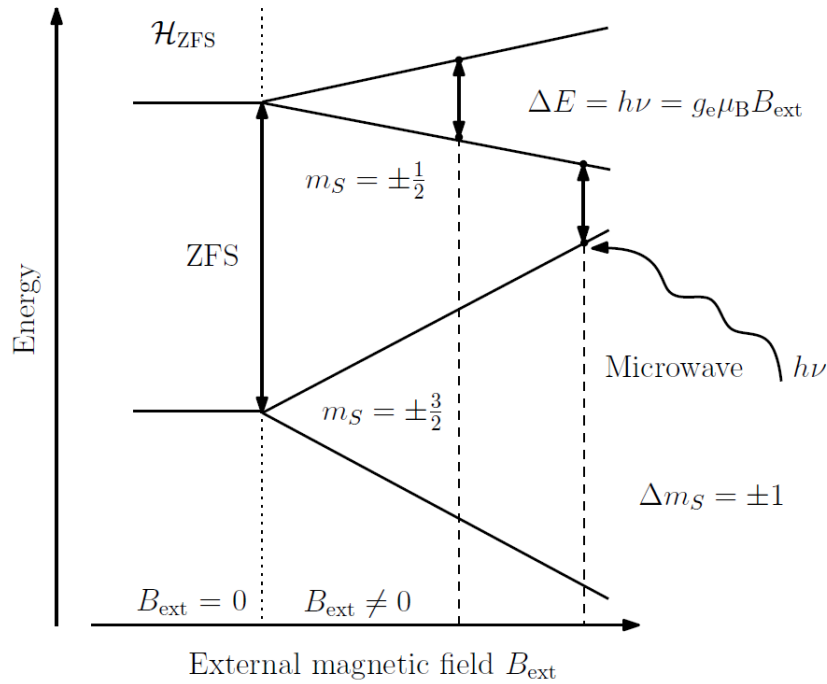


Fig. 2.14: Representation of ZFS for the system with electron spin $S = 3/2$ and $D < 0$. Taken with permission of my colleague Ing. Jakub Hrubý, Ph.D. [56].

Principle of the measurement

When measuring EPR, the sample is irradiated with electromagnetic waves of constant frequency (often microwaves), and the magnitude of the applied magnetic field changes. At a certain value of B , the resonant condition is met, the photon is absorbed, and the transition of the electron to a higher energy level occurs while following the selection rules: $\Delta m_S = 1$ and $\Delta m_S = 0$. The transitions between Zeeman-split levels apply the most. The derivative of the absorption line is measured. The substance information is then provided by the g-factor (orientation of the substance in the magnetic field) and D , E , whose values are determined by fitting the spectra.

3. Experimental part

In the experimental part, six selected cobalt(II)-based SIMs with bidentate ligands deposited on graphene were studied. The resulting samples form the so-called hybrid material (schematically shown in Fig. 3.1), which consists of a SiO₂/Si, graphene, and a SIMs layer. The production process and characterization are described on the following pages.

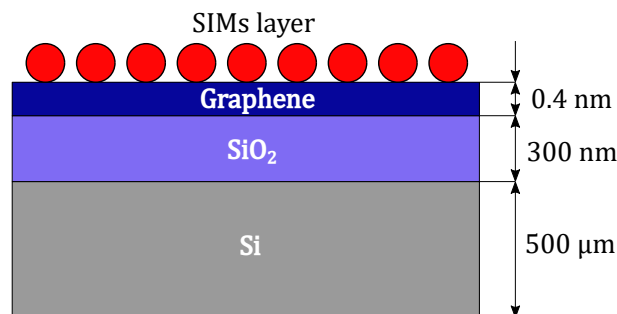


Fig. 3.1: Scheme of the prepared hybrid material.

3.1. Measurement parameters

Samples were characterized by methods that were described in the theoretical part 2.4. All measurements were carried out at CEITEC Nano.

AFM

AFM was measured on the ICON-SPM (Bruker, USA), and tapping mode was used. The acquired data were processed in Gwyddion.

SEM

SEM images were acquired using a high-resolution Scanning Electron Microscope FEI Verios 460L (ThermoFisher Scientific, USA). Everhart–Thornley detector was used for the detection of secondary electrons.

Raman spectroscopy

Raman spectra were measured using a confocal Raman microscope Alpha300 R+ (WITec, Germany). A 532 nm laser with a power of 1 mW was used in all measurements. This microscope was also used to take optical images with a 100× objective (NA 0.9, 142 WD 0.31 mm).

XPS

XPS measurements were performed on a Kratos Axis Supra instrument (Kratos Analytical, United Kingdom) at room temperature in UHV. Monochromatic source Al K α 1486.6 eV (15 mA, 15 kV), hemispherical analyzer, and charge neutralizer were used. All peaks were corrected for the carbon peak 284.8 eV. The background was subtracted using the

Shirley method [57] and the individual peak components were fit with the standard deconvolution method using a mixed Gaussian (G) and Lorentzian (L) line shapes (G = 70% and L = 30%). The fitting was performed using CasaXPS 2.3.18.

EPR

EPR spectra were measured on a newly built high-frequency EPR spectrometer at MOTES CEITEC with a magnetic field range 0-15 T. The bulk sample of SIM was studied as a pressed powder pellet with a diameter of 5 mm.

Vibrating sample magnetometer (VSM)

Measurements were acquired using Low-Temperature Vibrating Sample Magnetometer (Cryogenic Limited, United Kingdom) with a temperature range from 1.6 K to 400 K and a magnetic field from 0 to 9 T. The sample was mixed with icosane and studied in the form of a sphere with a 4 mm diameter. All data were simulated using EasySpin 5.2.33 [58]. The measurements and fitting were done by Mgr. Lubomír Havlíček and Ing. Ivan Nemeč, Ph.D., and the graphs are attached in the attachment to this thesis. The resulting parameters are given in the main text to give an insight into the magnetic properties of each SIM.

3.2. Substrate

A commercially produced silicon wafer covered by graphene purchased from the company Graphenea (Spain) was used as a substrate. It is a monolayer chemical vapor deposition (CVD)-grown graphene transferred on SiO₂/Si substrate. SiO₂ is 300 nm thick. The silicon wafer with graphene was cut into rounds of a 5 mm diameter to fit into the EPR sample holder (photo shown in Fig. 3.2a). As a prevention against damage during laser cutting, the surface was first covered with a layer of gold, and after cutting, it was etched away with an aqua regia (HNO₃ + 3 HCl).

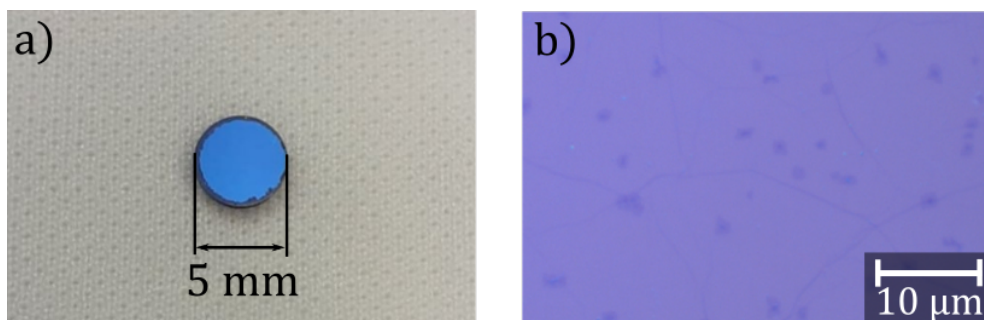


Fig. 3.2: a) Photo of a sample used as a substrate: CVD graphene on SiO₂/Si. b) Image from the optical microscope of the same sample.

Raman spectrum in Fig. 3.3 of the substrate was measured for quality verification and future comparison with deposited samples. The SiO₂/Si Raman spectrum has a strong peak at 520 cm⁻¹, two medium peaks at 301 cm⁻¹ and in the region 940–980 cm⁻¹ and weak peaks at 431 cm⁻¹, 619 cm⁻¹ and 672 cm⁻¹ [59]. A spectrum of CVD graphene exhibited the strong peaks D at 1346 cm⁻¹, G at 1594 cm⁻¹, and 2D at 2689 cm⁻¹, with the weaker

3.3. DEPOSITION

peaks D' at 1622 cm^{-1} , D+D'' at 2464 cm^{-1} , D+D' at 2950 cm^{-1} and 2D' at 3255 cm^{-1} [60]. The presence of a strong G peak and a weak D' peak indicates that defects occur in the graphene [35].

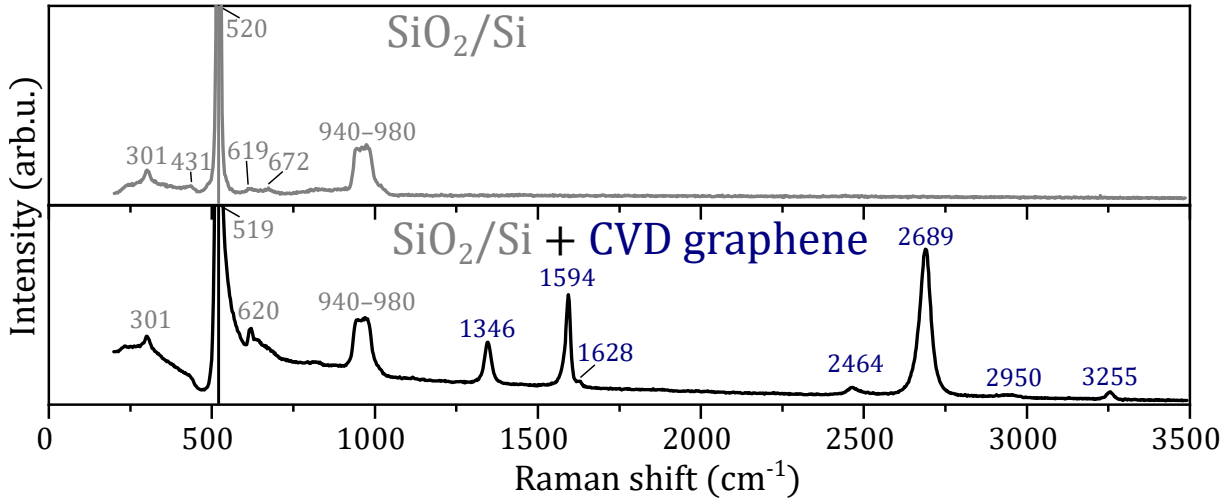


Fig. 3.3: Comparison of Raman spectra of SiO_2/Si (Raman shift values marked in grey) and CVD graphene on SiO_2/Si (Raman shift values marked in dark blue).

3.3. Deposition

The following two approaches were chosen from the deposition methods presented in the theoretical part 2.2. Thermal sublimation of six different SIMs was carried out in a home-built high-vacuum sublimation chamber (Activair, Czech Republic) shown in Fig. 3.4a. High vacuum (1×10^{-6} – 1×10^{-7} mbar) was achieved by pumping with a diaphragm pump and then a turbomolecular pump. After reaching the required pressure, a quartz crucible with SIM's powder was heated by a ceramic heater (BACH RC, Seefeld, Germany) pictured in Fig. 3.4c. The temperature was monitored by a thermocouple in thermal contact with the heater. At a specific temperature, SIM's molecules start to sublime. A layer of molecules formed on the surface of the substrate (mounted on a sample holder in Fig. 3.4b), and its thickness was monitored using a QCM. It was necessary to pay attention to the temperature, as decomposition could occur at higher temperatures. The temperature limit can be set with respect to the thermogravimetric analysis (TGA - a technique that monitors the mass of the sample as a function of temperature, from which we can determine the temperature at the beginning of the decomposition).

Two of the six selected SIMs were also deposited using a drop-casting method to verify their stability under ambient conditions.

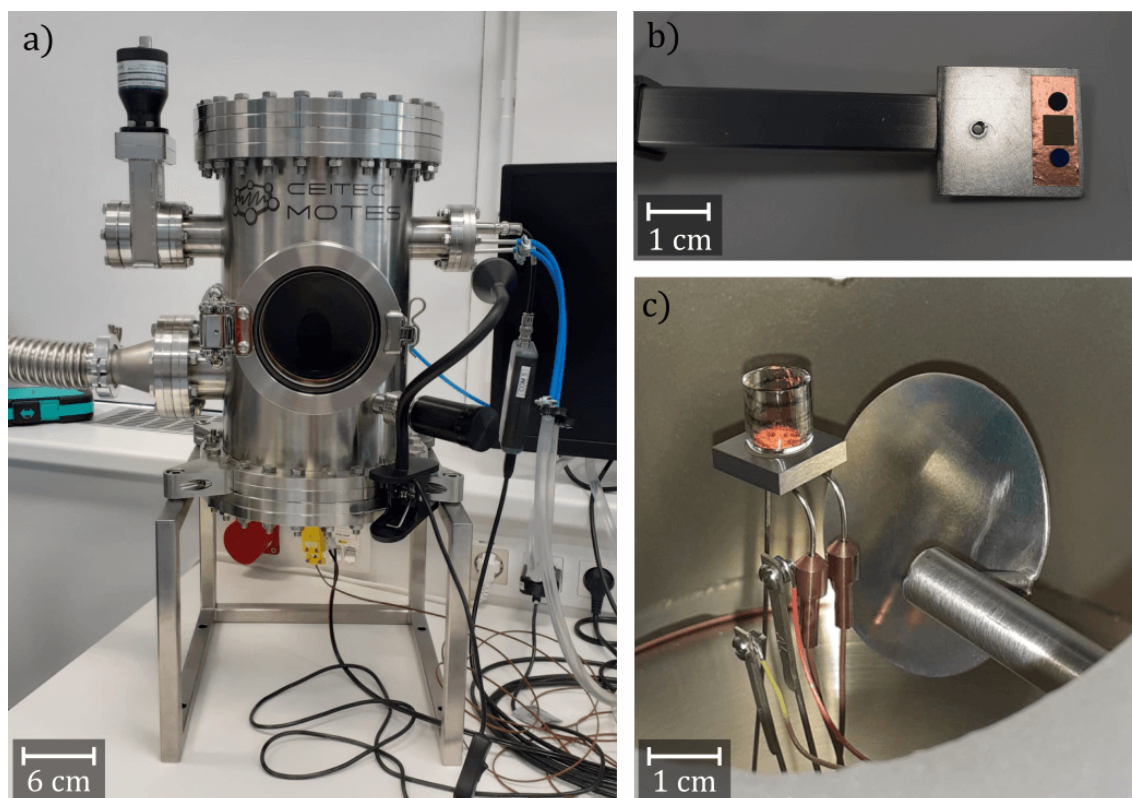


Fig. 3.4: a) Sublimation chamber used for all thermal sublimations, b) sample holder and c) quartz crucible with SIMs powder placed on the ceramic heater next to the shutter.

3.4. Compound (1a)

The first examined SIM was azido-(tris((2-benzylamino)ethyl)amine)-cobalt(II) chloride, shortly $[\text{Co}(\text{trenb})\text{N}_3]\text{Cl}$ whose chemical structure is shown in the Fig. 3.5. Within this thesis, this compound is referred to as (1a). The molecular formula of this compound is $\text{C}_{27}\text{H}_{36}\text{ClCoN}_7$ and molar mass 569.07 g/mol. Compound 1a was synthesized in the form of turquoise powder by Mgr. Lubomír Havlíček (CEITEC VUT) adapting previously reported synthetic procedure [61]. The synthesis procedure is described in the attachment to this thesis.

By measuring and fitting the VSM data, the magnetic properties were determined as $g_{\text{iso}} = 2.24$ $D = -5.64 \text{ cm}^{-1}$ and $E/D = 0$. The figure of the measured and fitted data is provided in the attachment to this thesis.

Thermal sublimation was carried out at $344 \text{ }^\circ\text{C}$ at a pressure in the order of 10^{-6} mbar. At this temperature, the substance starts to sublime considerably. The TGA analysis of this substance was not measured due to a possible azide explosion that could damage the instrument [62]. However, later TGA measurements for a similar substance (1b) show that it is already decomposed at this temperature (displayed in the attachment).

The sublimation ended when QCM showed a layer thickness of 150 \AA .

3.4. COMPOUND (1A)

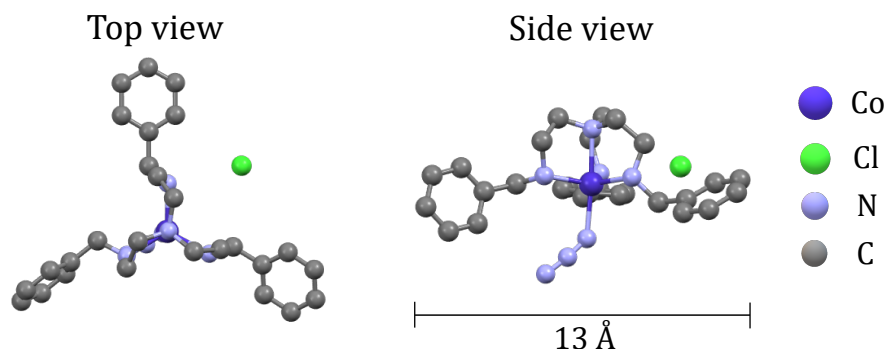


Fig. 3.5: Molecular structure of the compound (1a). Hydrogen atoms are omitted for the sake of clarity.

An optical image of the resulting sample is shown in Fig. 3.6a, where we can see that we are not able to observe the surface coverage using an optical microscope. Therefore, the sample was examined by SEM, wherein Fig. 3.6b we can see black spots representing the areas covered by deposited material. AFM was used to determine the thickness of these spots. Fig. 3.6c, along with the height profile, shows that the spots are several nanometers high, and more material accumulates at the graphene grain boundaries.

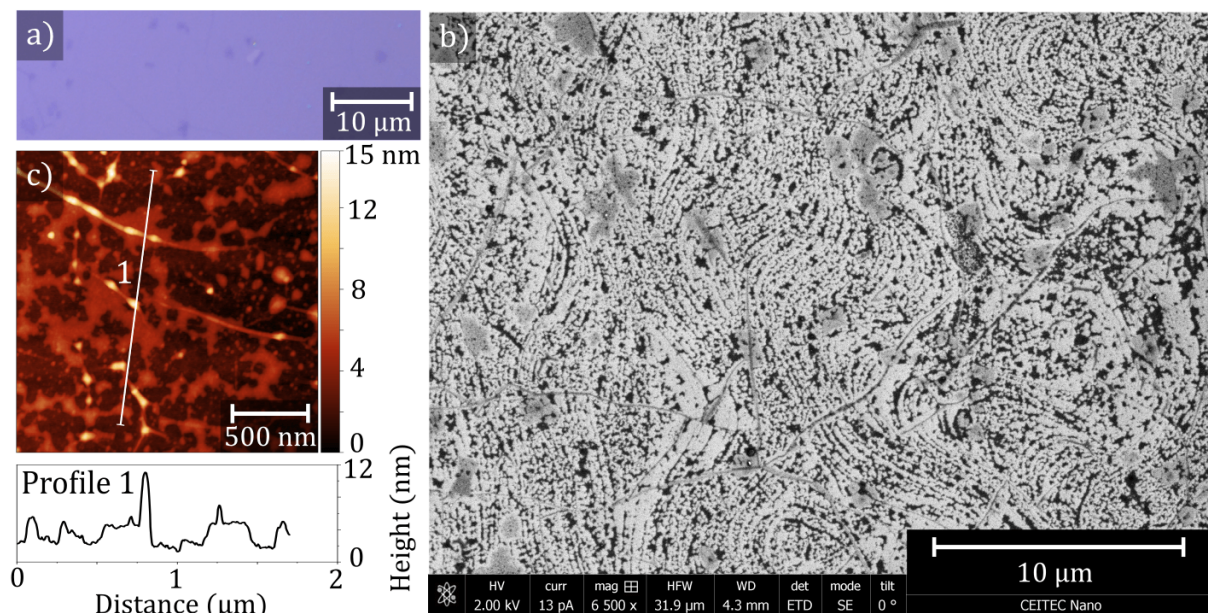


Fig. 3.6: a) Optical image of compound (1a) sublimated on graphene. b) SEM image of the same sample. c) AFM image and height profile along the white line 1.

To verify the intactness of the studied compound, Raman spectroscopy was performed to compare the vibrational modes of the individual components of the resulting hybrid material. Fig. 3.7 shows Raman spectra, from top to bottom, of a SiO₂/Si + CVD graphene, powder of (1a) and deposited (1a) by thermal sublimation. The Raman spectrum of CVD graphene on SiO₂/Si was described in 3.2. The Raman spectrum of the bulk compound (1a) contains peaks characteristic of the ligand's functional groups such as benzyl, amine, and azide [50, 63, 64]. The strongest peaks around 1000, 1600, 3000 cm⁻¹ originate mainly from benzyl group [50].

In the Raman spectrum of the sublimated sample, we can also observe these peaks, but their relative ratios are different. For example, the peak around 1000 cm⁻¹ is no longer

the strongest and the peaks around 3000 cm^{-1} are dominated by aliphatic C-H bonds ($<3000\text{ cm}^{-1}$) over aromatic ($>3000\text{ cm}^{-1}$) [50]. This could indicate that the compound (1a) has undergone a change during deposition.

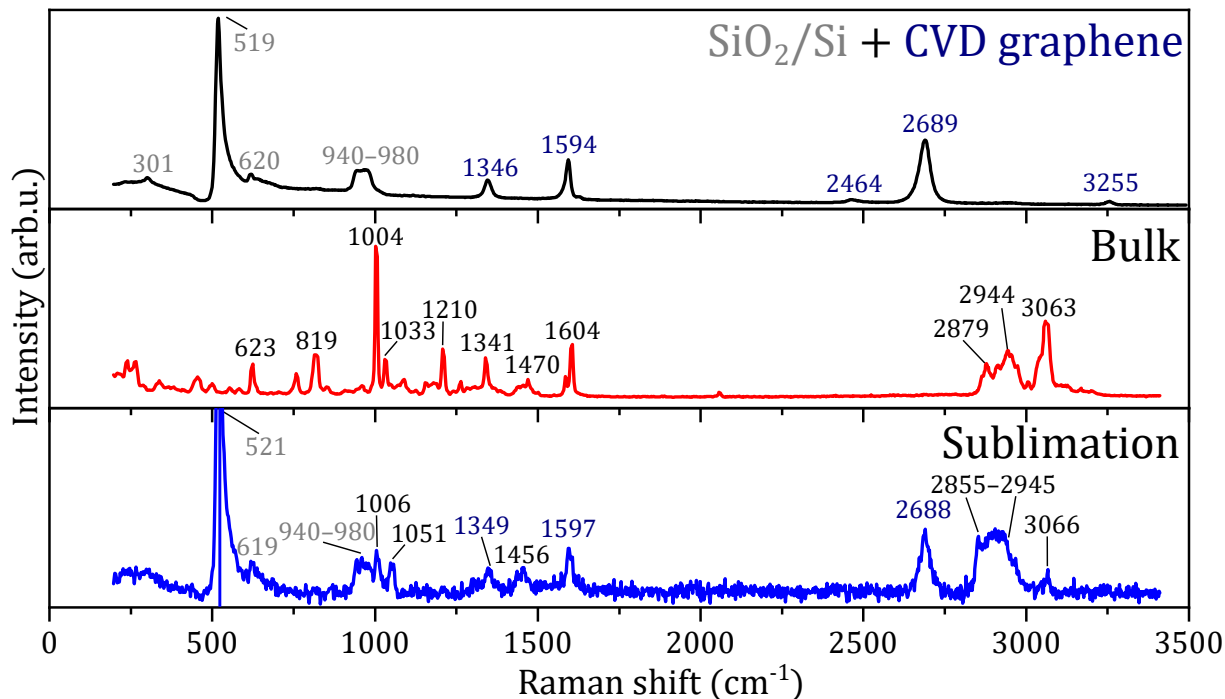


Fig. 3.7: Comparison of Raman spectra, from top to bottom, of the substrate: CVD graphene (Raman shift values marked in dark blue) on SiO_2/Si (marked in grey), bulk (1a) and deposited (1a) by thermal sublimation (marked in black).

The chemical composition was probed by XPS. Fig. 3.8 shows the comparison of XPS spectra for bulk and sublimated sample. Both survey spectra exhibit photoelectron peaks: Co 2p, N 1s, Cl 2p, C 1s, and O 1s; and Augers peaks: O_{KLL} and Co_{LMM} . In the case of bulk spectrum, Sn 3d peak is observed. This contamination likely originates from a synthetic process, when tin was most likely present in hydrochloric acid during the synthesis of the ligand.

The detailed spectra of the selected peaks unveil specific chemical composition. The photoelectron peaks originating from the electronic levels p, d and f are split into two components in a certain ratio and shift due to spin-orbit interactions [53].

Co 2p peak of the bulk exhibits two main components Co $2p_{3/2}$ and Co $2p_{1/2}$ and shake-up satellites, which are common with paramagnetic states [53]. The oxidation state depends on spin-orbit splitting of the main components Co $2p_{3/2}$ and Co $2p_{1/2}$, and with $\Delta = 15.5\text{ eV}$, it corresponds to Co(II) in the high-spin state [65]. In the case of the sublimated sample, the Co 2p signal is weak (the surface is not densely covered, and there is only one Co atom per one SIMs molecule, whereas the other elements are more abundant). However, we could observe and fit the peak Co $2p_{3/2}$ and the satellite, which was shifted with respect to the peak of the bulk (0.9 eV and 1.4 eV to higher binding energy, respectively).

As for chloride Cl 2p, two pairs of Cl $2p_{3/2}$ and Cl $2p_{1/2}$ components with spin-orbit splitting $\Delta = 1.6\text{ eV}$ are observed [53]. The positions of the peaks ($\approx 198\text{ eV}$) are consistent with inorganic chloride [66].

3.4. COMPOUND (1A)

In the case of N 1s of the bulk, the peak includes five components. The main component corresponds to the amine at 399.9 eV, and two smaller peaks at 398.5 eV and 402.8 eV are attributed to the azido group [67, 68]. The smallest peak at 406.3 eV may be attributed to chemisorbed nitrogen [70]. The origin of the fifth peak at 397.1 eV may correspond to unreacted azide [71]. In the case of the sublimated sample, the main component and chemisorbed nitrogen are shifted by 0.5 eV and 0.8 eV to higher binding energy, and a new peak appears at 401.9 eV. Azide components are no longer present.

Detailed spectra of O 1s and C 1s are not shown since they are affected by adventitious contaminations due to the ex-situ preparation procedures.

Considering the changes in the ratio of the peaks in the Raman spectrum and especially in the XPS spectrum of nitrogen, where we do not observe peaks of the azide group and a new peak appears, it can indicate possible sample decomposition during the sublimation.

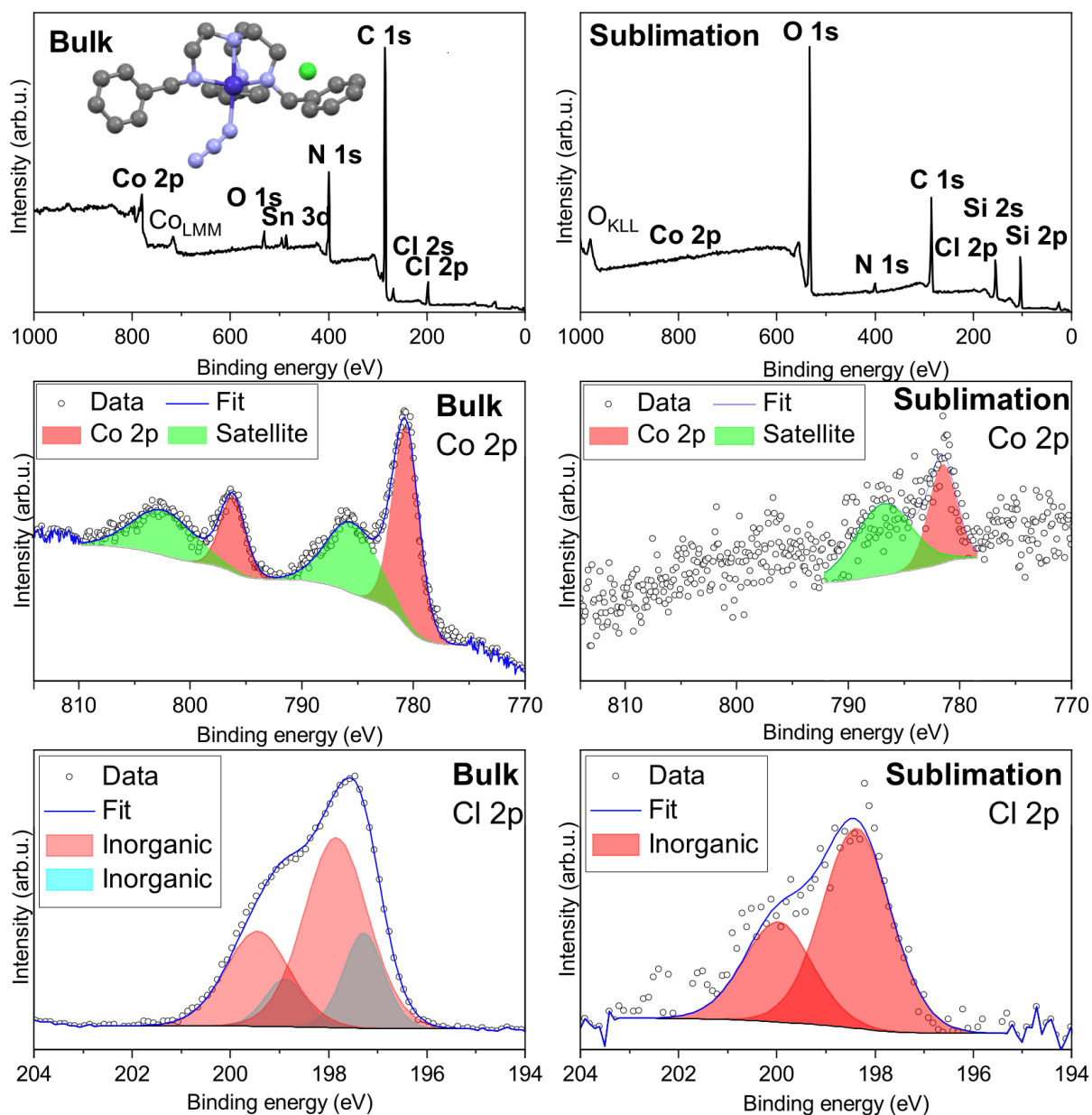


Fig. 3.8: Comparison of XPS spectra of the bulk (2a) and sublimated (2a) on graphene.

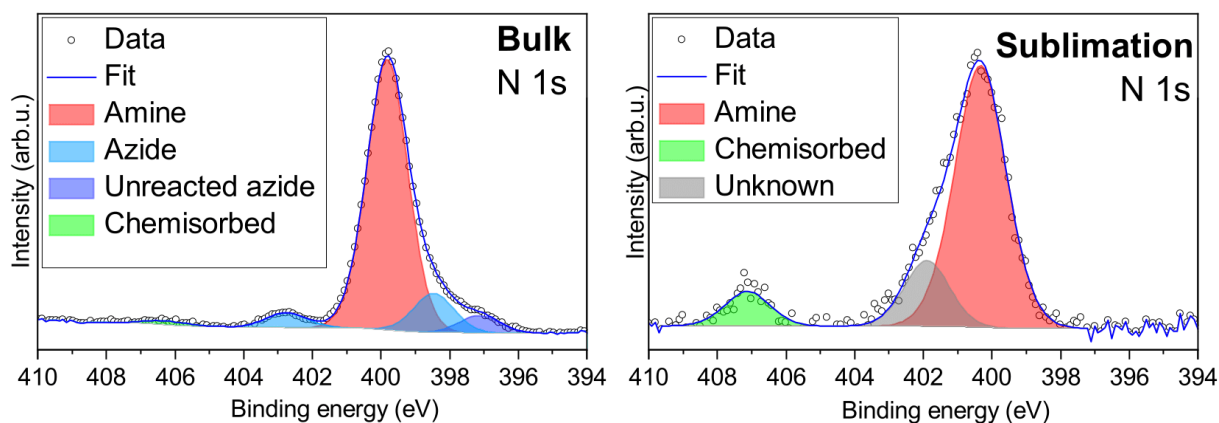


Fig. 3.9: Comparison of XPS spectra of N 1s peak of the bulk (1a) and sublimated (1a) on graphene.

3.5. Compound (1b)

The second examined SIM was isothiocyanato-(tris((2-benzylamino)ethyl)amine)-cobalt(II) chloride, shortly $[\text{Co}(\text{trenb})(\text{NCS})]\text{Cl}$ whose chemical structure is shown in the Fig. 3.10. As can be seen, the compound is similar to the previous compound 1a, except that the azide group has been replaced by a thiocyanate group. Therefore this compound is labeled 1b. The molecular formula of compound (1b) is $\text{C}_{28}\text{H}_{36}\text{ClCoN}_5\text{S}$ and molar mass 569.07 g/mol. Compound (1b) was synthesized in the form of light blue powder by Mgr. Lubomír Havlíček (CEITEC VUT) on the basis of an article [61]. The synthesis procedure is described in the attachment to this thesis.

By measuring and fitting the VSM data, the magnetic properties were determined as $g_{\text{iso}} = 2.192$, $D = -1.5 \text{ cm}^{-1}$ and $E/D = 0.33$. The figure is provided in the attachment to this thesis.

Thermal sublimation was carried out at 352 °C at the pressure in the order of 10^{-6} mbar. At this temperature, the substance began to sublime considerably. However, later measurements of the TGA analysis at atmosphere pressure revealed that compound (1b) is already decomposed at this temperature (a graph is provided in the attachment). The sublimation ended when QCM showed a layer thickness of 500 Å.

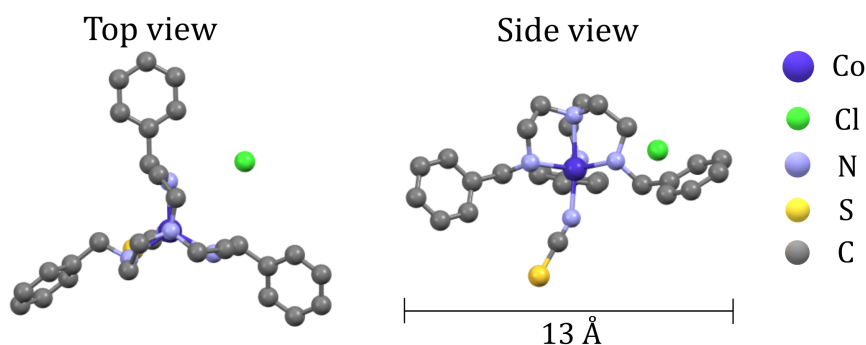


Fig. 3.10: Molecular structure of the compound (1b). Hydrogen atoms are omitted for the sake of clarity.

A comparison of the Raman spectra (see Fig. 3.13) showed that graphene was not present in the resulting hybrid material. This is most likely due to the process of cutting

3.5. COMPOUND (1B)

the graphene wafer into rounds (described in the section: 3.2). During this process, the graphene was probably distorted and was washed away with the gold when it was etched away. We were unaware of this prior deposition attempts, and therefore, we used it as a regular substrate with graphene. Therefore, we will refer to the sample missing graphene as modified SiO₂/Si. Thermal sublimation was also performed on SiO₂/Si (280 nm) as a comparison sample.

An optical image of the resulting sample is shown in Fig. 3.11a, where we can see a densely covered surface in the form of merging irregular shapes. Moreover, the sample was examined by SEM, wherein Fig. 3.11b we can see black areas showing the areas covered by molecules of (1b). In contrast, optical and SEM images in Fig. 3.11c revealed that smaller round islands form on the SiO₂/Si.

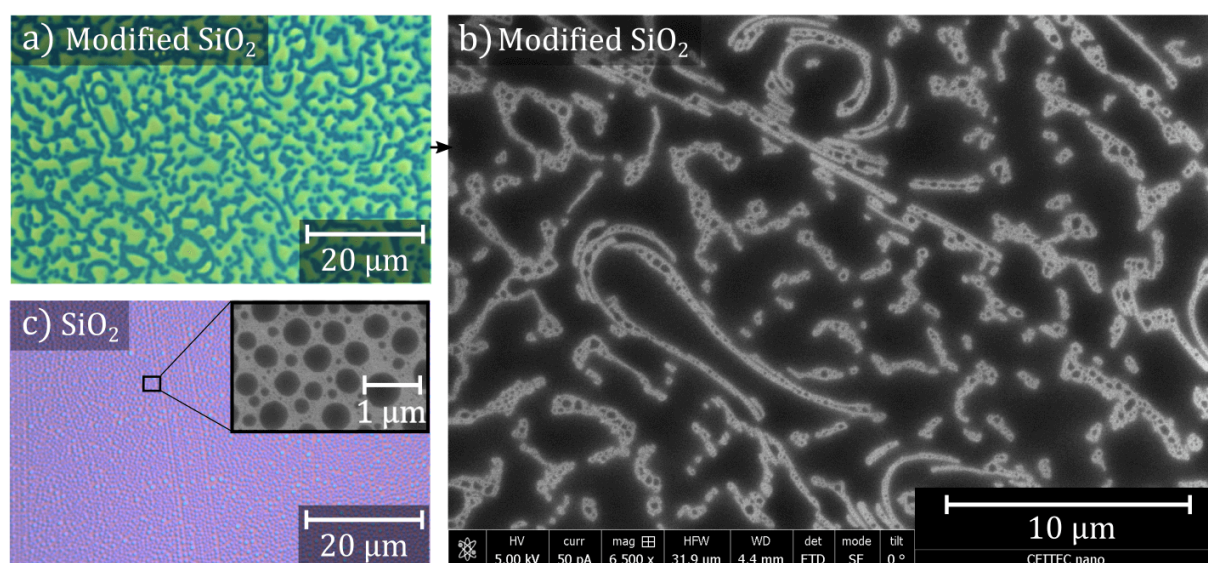


Fig. 3.11: a) Optical image of (1b) sublimated on modified SiO₂/Si. b) SEM image of the same sample. c) Optical image of (1b) sublimated on clear SiO₂/Si sample and zoomed cutout by SEM.

The thickness of the coverage on the modified SiO₂/Si was determined by AFM. Fig. 3.12 and the height profile shows a height of up to 100 nanometers.

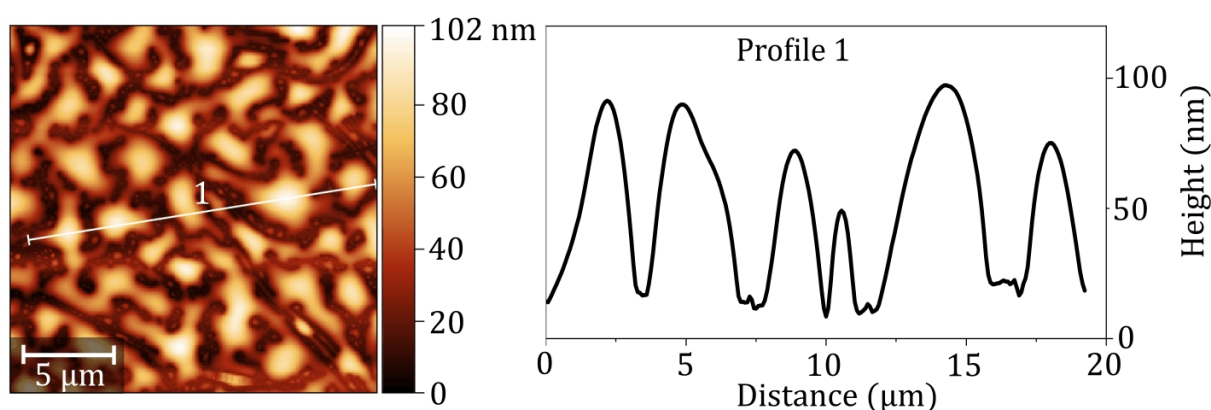


Fig. 3.12: AFM image of compound (1b) sublimated on modified SiO₂/Si on the left and its height profile along the white line 1 on the right.

Raman spectroscopy was performed to compare the vibrational modes of the individual components of the resulting hybrid material. Fig. 3.13 shows Raman spectra, from top to bottom, of a SiO₂/Si + CVD graphene, powder of (1b) and deposited (1b) by thermal sublimation. The Raman spectrum of CVD graphene on SiO₂/Si was described in 3.2. The Raman spectrum of the bulk compound (1b) contains peaks characteristic of the ligand's functional groups such as benzyl, amine and thiocyanato group [50, 63, 64]. The strongest peaks around 1000, 1600, 3000 cm⁻¹ originate mainly from benzyl group [50].

In the case of a sublimated sample, only peaks of SiO₂/Si are present. Missing graphene peaks were explained earlier. The signal from the molecule was either below the detection limit or the molecule had degraded.

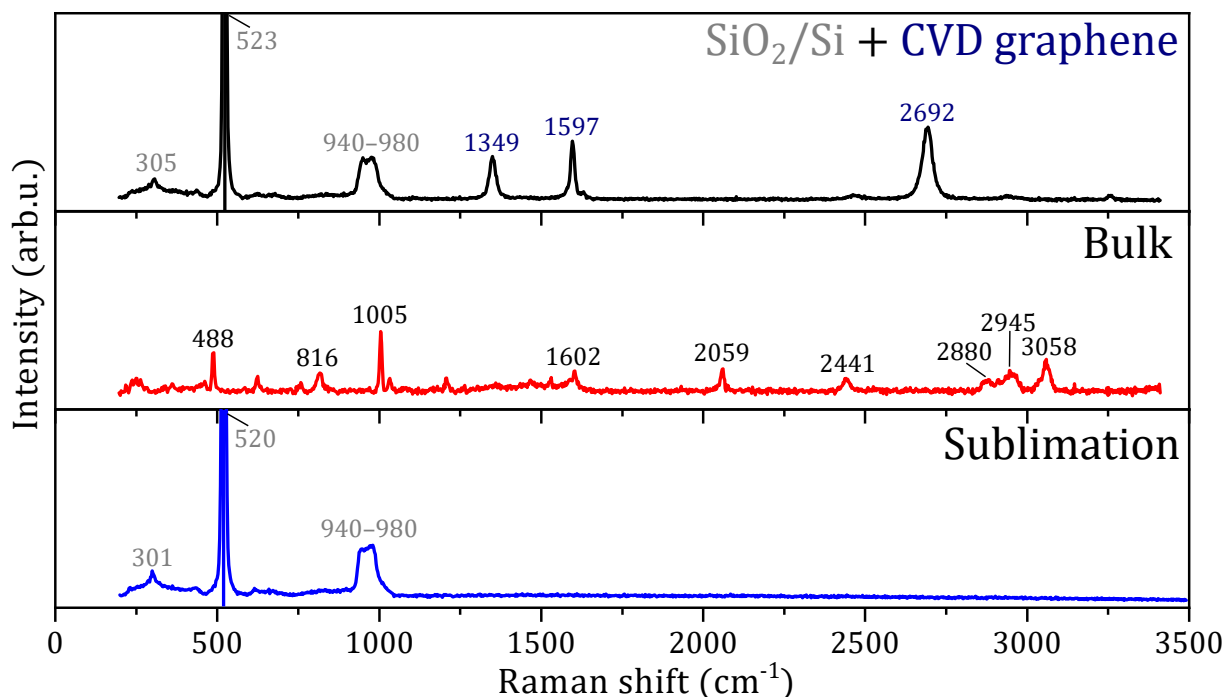


Fig. 3.13: Comparison of Raman spectra, from top to bottom, of the substrate: CVD graphene (Raman shift values marked in dark blue) on SiO₂/Si (marked in grey), bulk (1b) and deposited (1b) by thermal sublimation (marked in black).

The chemical composition was also probed by XPS. Fig. 3.8 shows the comparison of XPS spectra for bulk and sublimated sample. Both survey spectra exhibit photoelectron peaks: Co 2p, N 1s, S 2p, Cl 2p, C 1s, and O 1s; and Augers peaks: O_{KLL} and Co_{LMM}. In the case of bulk spectrum, Sn 3d peak is observed. This contamination likely originates from a synthesis process, when tin was most likely present in hydrochloric acid during the synthesis of the ligand.

The detailed Co 2p peak of the bulk exhibits two main components Co 2p_{3/2} and Co 2p_{1/2} and shake-up satellites, which are common with paramagnetic states [53]. The spin-orbit shift of the main components Co 2p_{3/2} and Co 2p_{1/2} $\Delta = 15.5$ eV corresponds to Co(II) in the high-spin state [65]. In case of sublimated sample, the Co 2p signal is not detected.

As for chloride Cl 2p, two pairs of Cl 2p_{3/2} and Cl 2p_{1/2} components with spin-orbit splitting $\Delta = 1.6$ eV are observed [53]. The positions of the 2p_{3/2} peaks ($\approx 197.5 - 198.5$ eV) are consistent with inorganic chloride [66].

3.5. COMPOUND (1B)

In the case of N 1s of the bulk, the peak includes three components. The main component corresponds to the amine at 399.9 eV, and smaller peak at 398.3 eV is attributed to the isothiocyanato group (NCS) [67, 72]. The smallest peak at 406.3 eV may be attributed to chemisorbed nitrogen [70]. In the case of the sublimated sample, the amine and NCS components are shifted by 0.6 eV to lower binding energy, and a new peak appears at 401.2 eV.

As for sulfur S 2p, two S 2p_{3/2} and S 2p_{1/2} components with spin-orbit splitting $\Delta = 1.18$ eV are observed for the bulk [53]. The position (S 2p_{3/2} at 162.7 eV) of the peaks is consistent with sulphur in (NCS) group [72]. After the deposition, the position of S 2p_{3/2} shifted to 162.2 eV, which may indicate a separation of the NCS group from the cobalt [72].

Detailed spectra of O 1s and C 1s are not shown since they are affected by adventitious contaminations due to the ex-situ preparation procedures.

Considering the changes in the XPS spectrum, especially no detection of Co 2p, a shift of the initial peaks of N 1s and S 2p, and the appearance of the new peak in N 1s, it seems that the compound had degraded during sublimation.

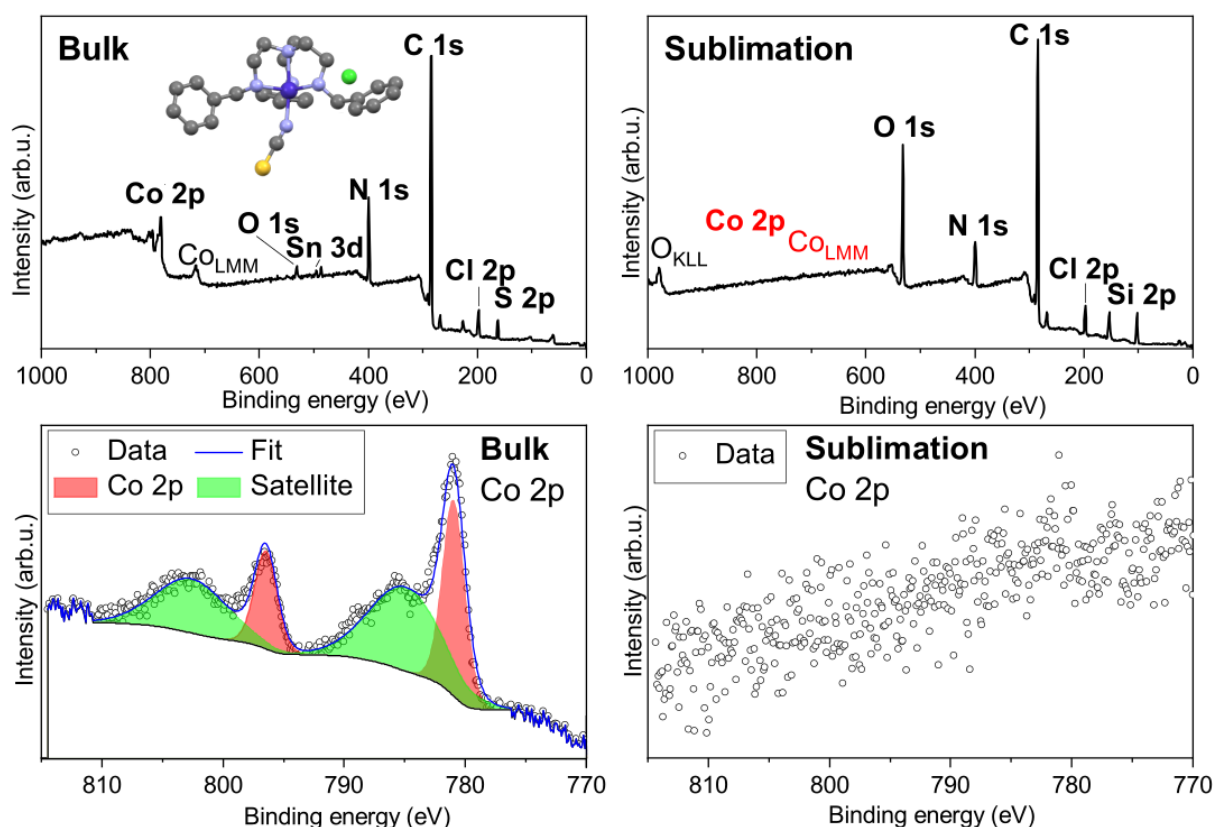


Fig. 3.14: Comparison of XPS survey spectra and Co 2p peak of the bulk (1b) and sublimated (1b) on graphene.

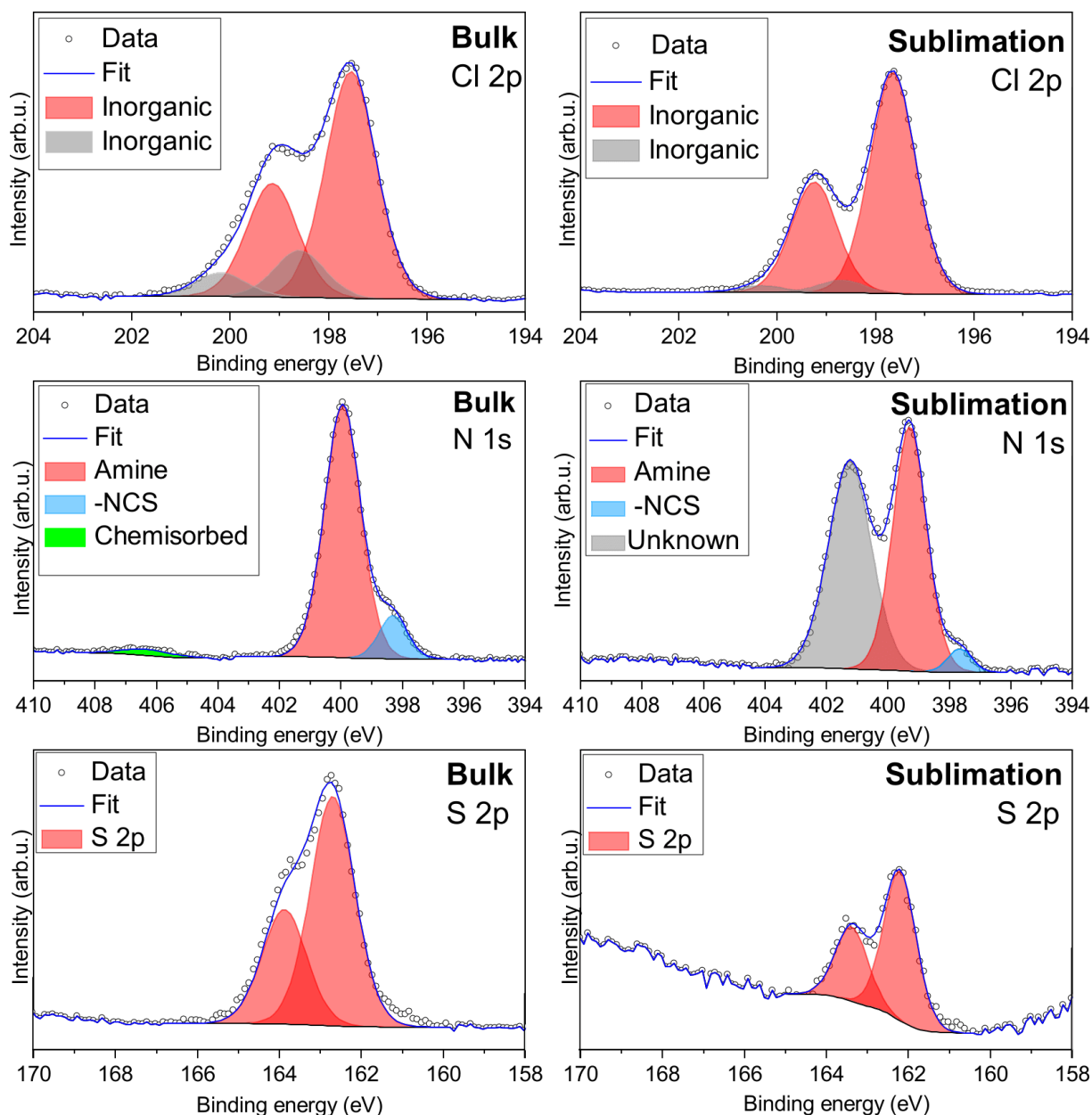


Fig. 3.15: Comparison of XPS spectra of Cl 2p, N 1s and S 2p peaks of the bulk (1b) and sublimated (1b) on graphene.

3.6. Compound (2a)

The third examined SIM was bis(2-Methyl-6-(2'-oxybenzylideneamino)pyridine-N,O)-cobalt(II), shortly [Co(salapi)₂] whose chemical structure is shown in the Fig. 3.16. Within this thesis, this compound is denoted (2a). The molecular formula of this compound 2a is C₂₆H₂₂Cl₂CoN₄O₂ and molar mass 481.41 g/mol. Compound 2a was synthesized in a form of red powder by Mgr. Ondřej František Fellner (Palacký University) adapting previously reported synthetic procedure [69].

3.6. COMPOUND (2A)

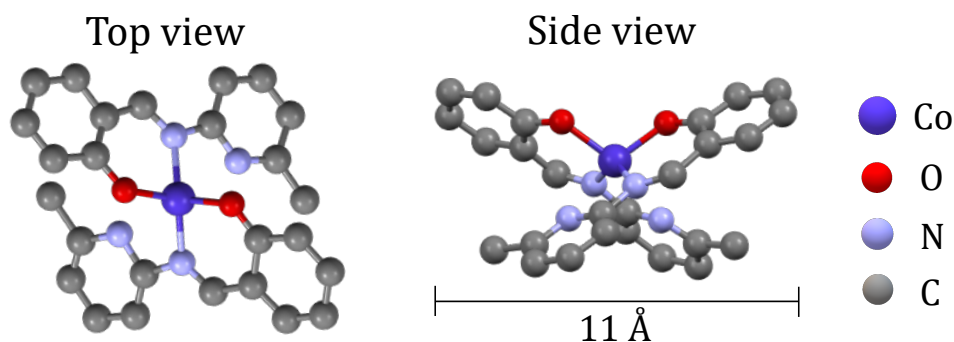


Fig. 3.16: Molecular structure of the compound (2a). Hydrogen atoms are omitted for the sake of clarity.

The powder of (2a) was measured using HF-EPR to verify the magnetic properties. The 18 mg of synthesized powder was compressed under a pressure of 2 tons into a pellet and placed in a cryostat. The sample was measured at 7 K at four different frequencies 150 GHz, 210 GHz, 320 GHz, and 420 GHz. The occurrence of absorption peaks in the spectra in Fig. 3.17a proves that the compound is paramagnetic.

By measuring and fitting the VSM data, the magnetic properties were determined as $g_{\text{iso}} = 2.20$ $D = -19.2 \text{ cm}^{-1}$ and $E/D = 0.079$. The figure of the measured and fitted data is provided in the attachment to this thesis.

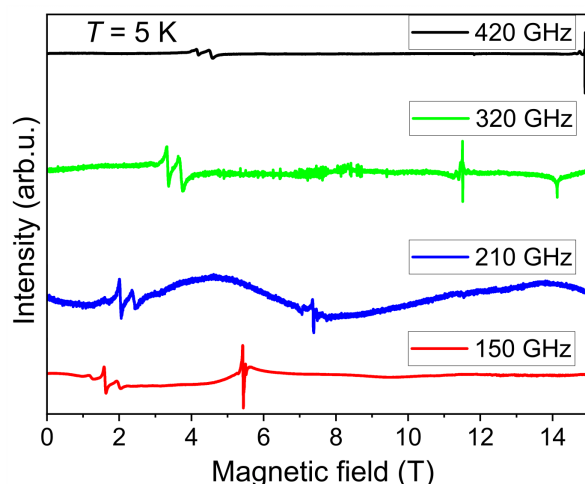


Fig. 3.17: EPR spectra of the bulk (2a) for four different frequencies.

To test the compound's (2a) stability during deposition at ambient conditions, it was deposited by drop-casting. The bulk was dissolved in acetone ($\text{C}_3\text{H}_6\text{O}$, 99%, Penta, Czech Republic) to make a final solution with a 1 mM concentration. The actual drop-casting was conducted in ambient conditions as $4 \times 10 \mu\text{L}$ was drop-casted onto a substrate. To test its thermal stability, deposition by thermal sublimation at pressure in the order of 10^{-6} mbar at 273 °C was performed. In this case, the TGA analysis was previously measured, which indicates the onset of decomposition of the molecule above this temperature (a graph is provided in the attachment). The sublimation was ended when QCM showed a layer thickness of 200 Å.

Optical images of the resulting samples can be seen in Fig. 3.18.

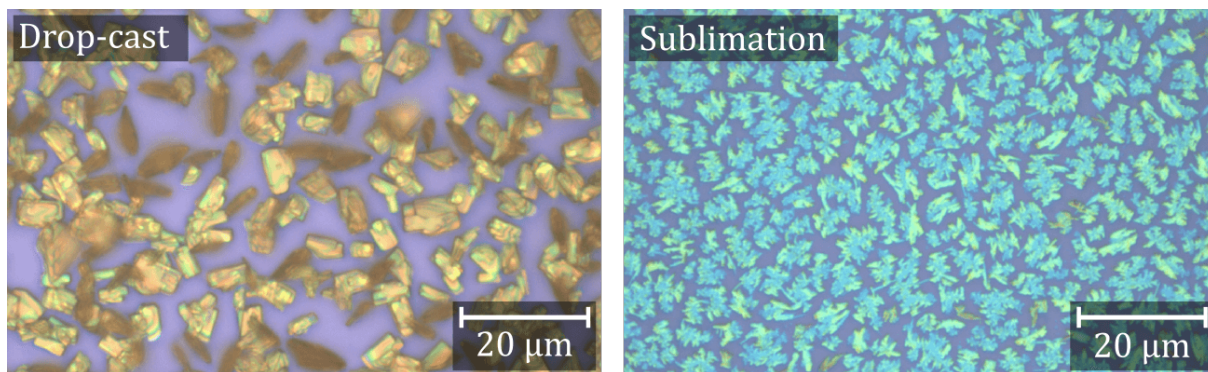


Fig. 3.18: Optical images of the compound (2a) drop-casted and sublimated on graphene.

Topography of both samples was investigated by AFM. As can be seen in Fig. 3.19, drop-cast led to the formation of crystals a few micrometers high, while thermal sublimation led to the formation of islands several micrometers in size and up to 150 nanometers in height. The difference may be due to a different amount of the deposited material.

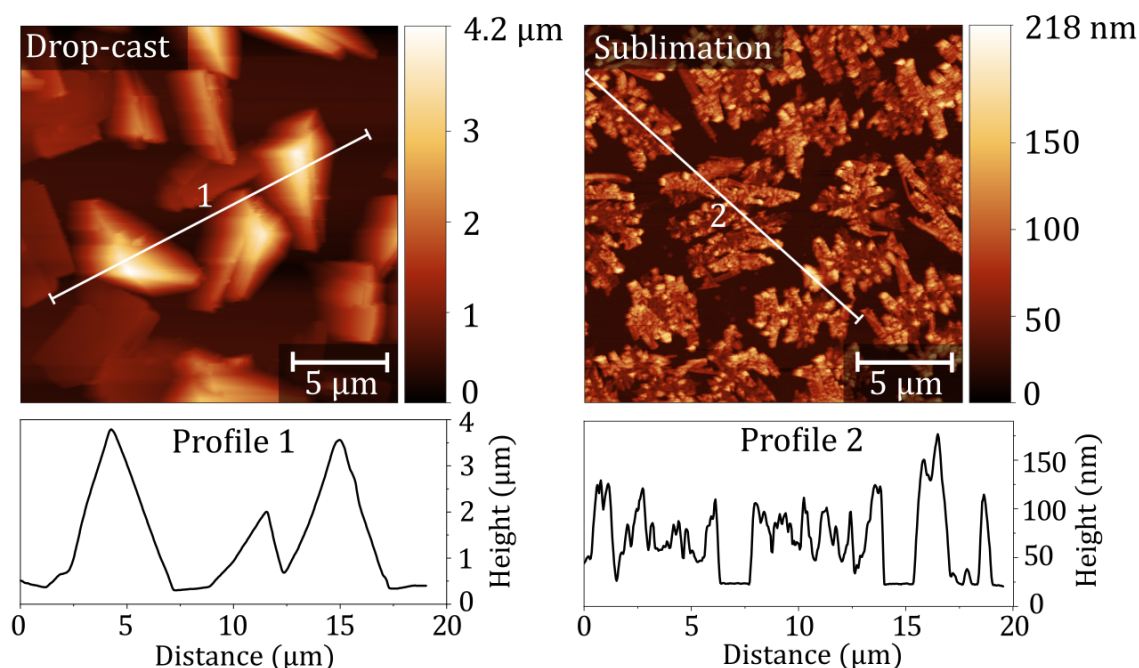


Fig. 3.19: AFM of the compound (2a) drop-casted and sublimated on graphene and height profiles along white lines 1 and 2.

Raman spectroscopy was performed to compare the vibrational modes of the individual components of the resulting hybrid material. Fig. 3.20 shows Raman spectra from top to bottom of a SiO₂/Si + CVD graphene, powder of (2a), deposited (2a) by drop-casting and by thermal sublimation on graphene. The Raman spectrum of CVD graphene on SiO₂/Si was described in 3.2. The Raman spectrum of the bulk compound (2a) contains peaks characteristic for the ligand's functional groups such as imino or aromatic C=C/N bonds (ca. 1400–1620 cm⁻¹) or the phenolic group (1200–1300 cm⁻¹) [64]. We chose to use following the most intensive peaks for comparison of the bulk and deposited materials (in cm⁻¹): 1227, 1355, 1385, 1435, 1523, 1563, 1604 and 1612 (Fig. 3.20). As can be seen from Fig. 3.20 the Raman spectra of hybrid materials prepared either by wet or sublimation

3.6. COMPOUND (2A)

techniques confirmed the presence of all the peaks observed for the bulk material and also all the spectral patterns agree exceptionally well.

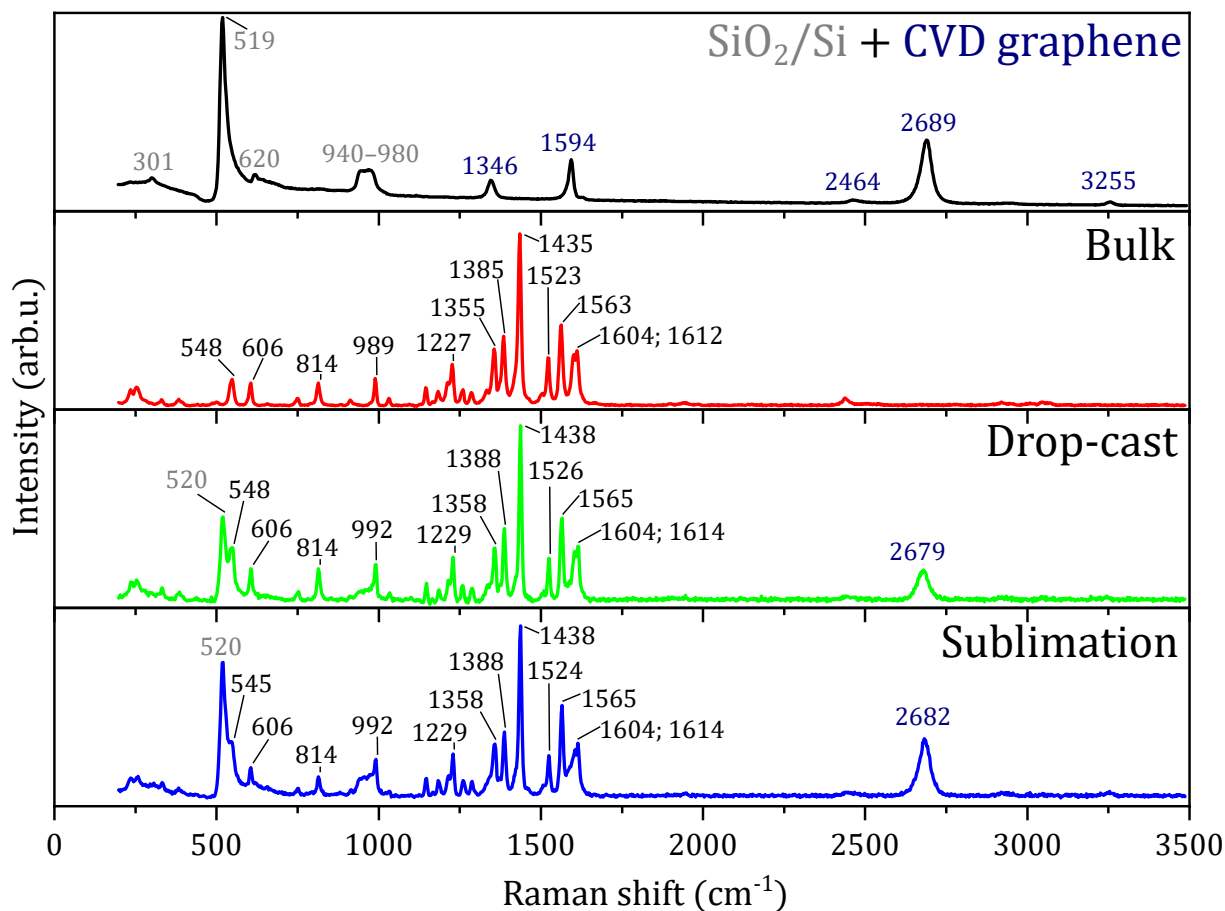


Fig. 3.20: Comparison of Raman spectra, from top to bottom, of SiO₂/Si substrate (Raman shift values marked in grey) and CVD graphene (marked in dark blue), bulk (2a), deposited (2a) on graphene by drop-casting and by thermal sublimation (marked in black).

The chemical composition of resulted hybrid material was probed by XPS. Fig. 3.21 shows the comparison of XPS spectra for bulk (2a) and sublimated sample. All survey spectra exhibited photoelectron peaks: Co 2p, N 1s, C 1s, and O 1s; and Augers peaks: O_{KLL} and Co_{LMM}. Both detailed Co 2p peaks exhibited two main components Co 2p_{3/2} and Co 2p_{1/2} and shake-up satellites. The spin-orbit shift of the main components Co 2p_{3/2} and Co 2p_{1/2} $\Delta = 15.5$ eV corresponds to Co(II) in the high-spin state [65]. In case of N 1s, peak is deconvoluted by four components: at 399.1 eV – corresponding to pyridinic nitrogen in the ligand [74], the smallest peak at 405.7 eV may be attributed to shake-up satellite [73]. Small peaks at 400-404 eV may be corresponding to a nitrogen impurities.

Detailed spectra of O 1s and C 1s are not shown since they are affected by adventitious contaminations due to the ex-situ preparation procedures.

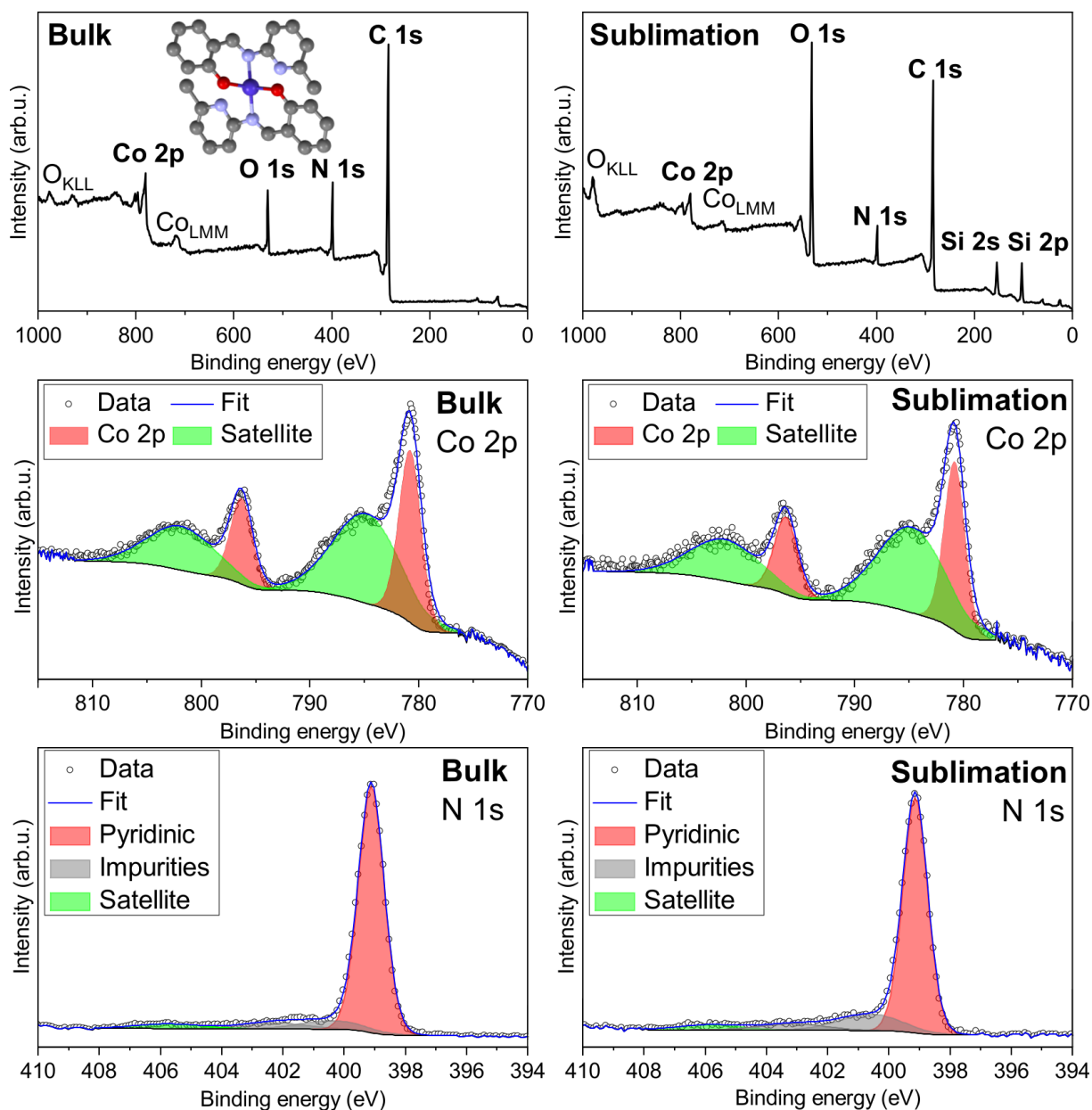


Fig. 3.21: Comparison of XPS spectra of the bulk (2a) and sublimated (2a) on graphene.

In case of drop-cast sample, the same peaks were observed except for chlorine Cl 2p peak (see Fig. 3.22). This contamination likely originates from a manufacturing process where a silicon wafer with CVD graphene was coated with gold, cut into smaller samples, and then the gold was dissolved with aqua regia ($\text{HNO}_3 + 3 \text{HCl}$) and insufficiently washed.

No significant change of N 1s shape or position is noticed in the cases of drop-cast and sublimated samples. In agreement with Raman spectroscopy, we can assume that compound (2a) was successfully deposited on graphene substrate both by drop-cast and thermal sublimation.

3.7. COMPOUND (2B)

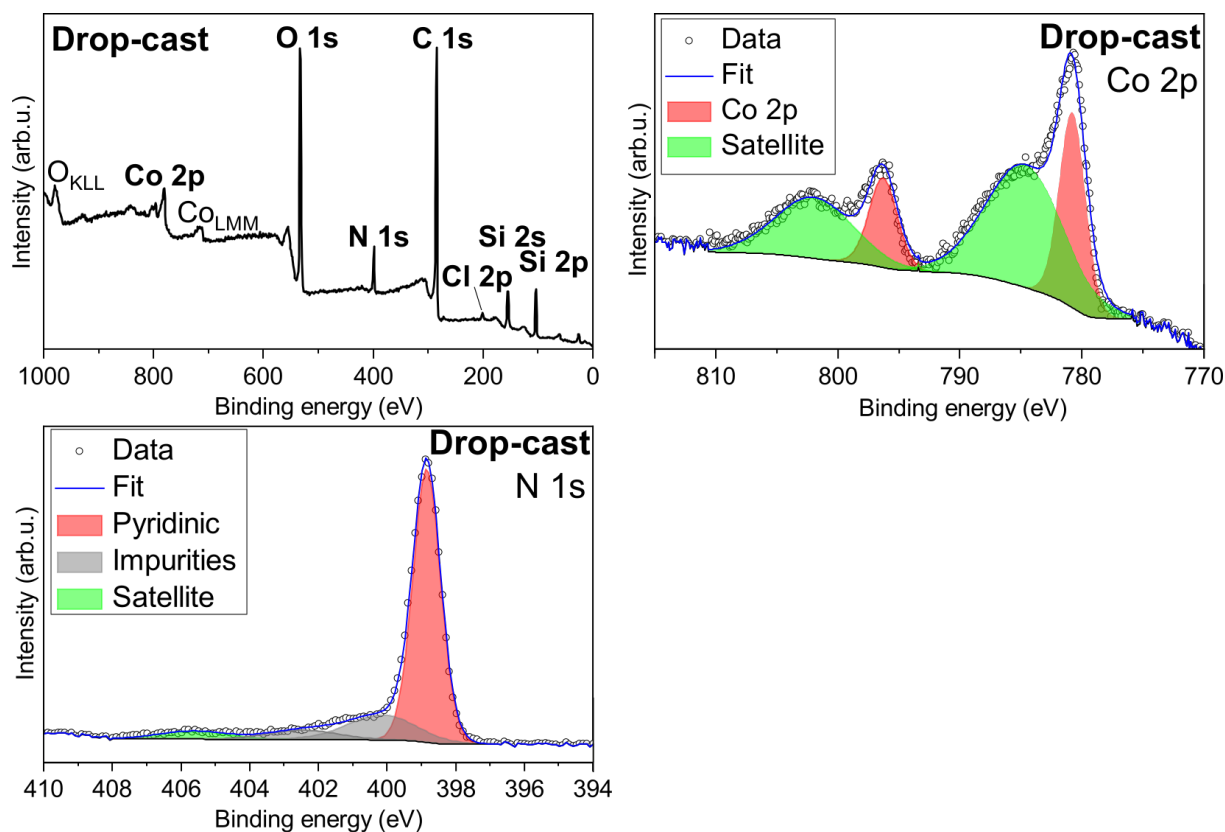


Fig. 3.22: XPS spectra of the drop-casted (2a) on graphene.

3.7. Compound (2b)

The fourth examined SIM was bis(2-Methyl-6-(2'-oxy-5'-methylbenzylideneamino)pyridine-N,O)-cobalt(II), shortly [Co(mesalapi)₂], whose chemical structure is shown in the Fig. 3.23. As can be seen, the compound is similar to the previous compound except that the two hydrogens has been replaced by the methyl groups. Therefore the compound is labeled (2b). The molecular formula of this compound is C₂₈H₂₆Cl₂CoN₄O₂ and molar mass 509.46 g/mol. This compound 2b was synthesized in a form of red powder by Mgr. Ondřej František Fellner (Palacký University) adapting previously reported synthetic procedure [69].

The magnetic properties were not measured due to a non-functioning magnetometer. However, the magnetic properties will be probably analogous to compound (2a) as it has a very similar structure.

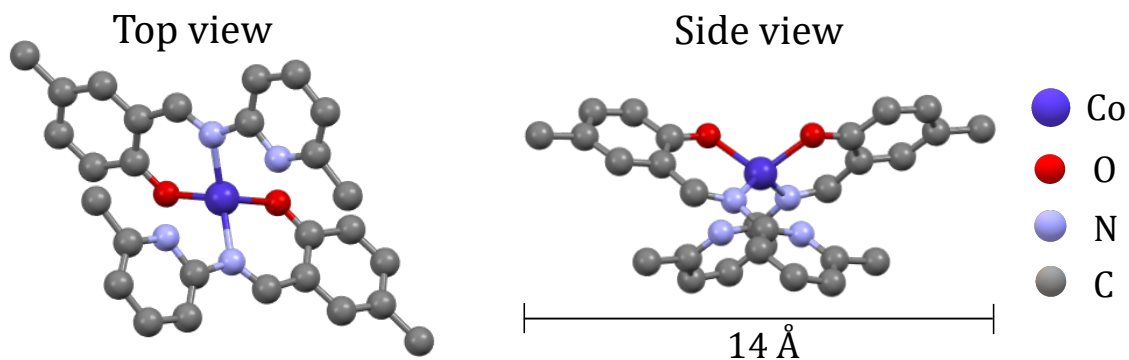


Fig. 3.23: Molecular structure of the compound (2b). Hydrogen atoms are omitted for the sake of clarity.

To test the compound's (2b) stability during deposition at ambient conditions, it was deposited by drop-casting. The bulk was dissolved in acetone (C_3H_6O , 99%, Penta, Czech Republic) to make a final solution with a 1 mM concentration. The actual drop-casting was conducted in ambient conditions as $4 \times 10 \mu\text{L}$ was drop-casted onto a substrate. To test its thermal stability, deposition by thermal sublimation at pressure in the order of 10^{-7} mbar at $283 \text{ }^\circ\text{C}$ was performed. In this case, the TGA analysis was previously measured, which indicates the onset of decomposition of the molecule above this temperature (a graph is provided in the attachment). The sublimation ended when QCM showed a layer thickness of 200 \AA .

Optical images of the resulting samples can be seen in Fig. 3.18.

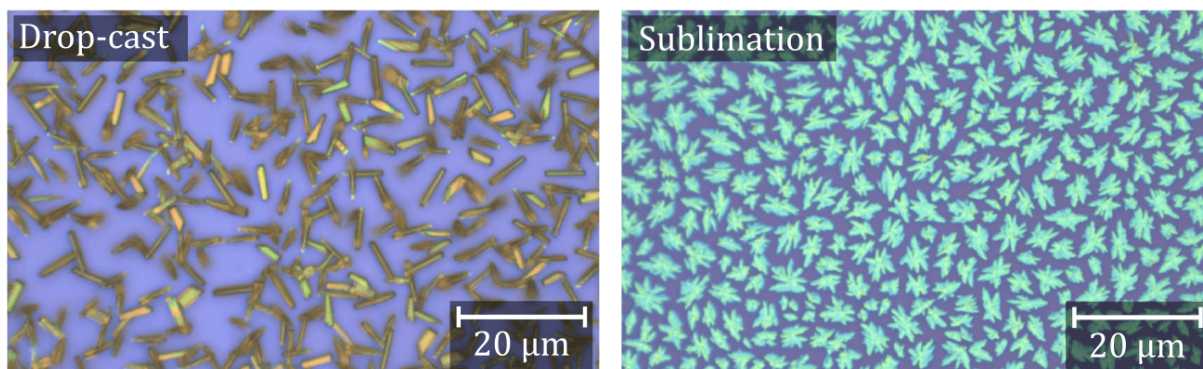


Fig. 3.24: Optical images of the compound (2b) drop-casted and sublimated on graphene.

Topography of both samples was investigated by AFM. As can be seen in Fig. 3.25, drop-cast led to the formation of crystals a few micrometers high, while thermal sublimation led to the formation of flaky islands several micrometers in size and up to 100 nanometers in height. The difference may be due to a different amount of deposited material.

3.7. COMPOUND (2B)

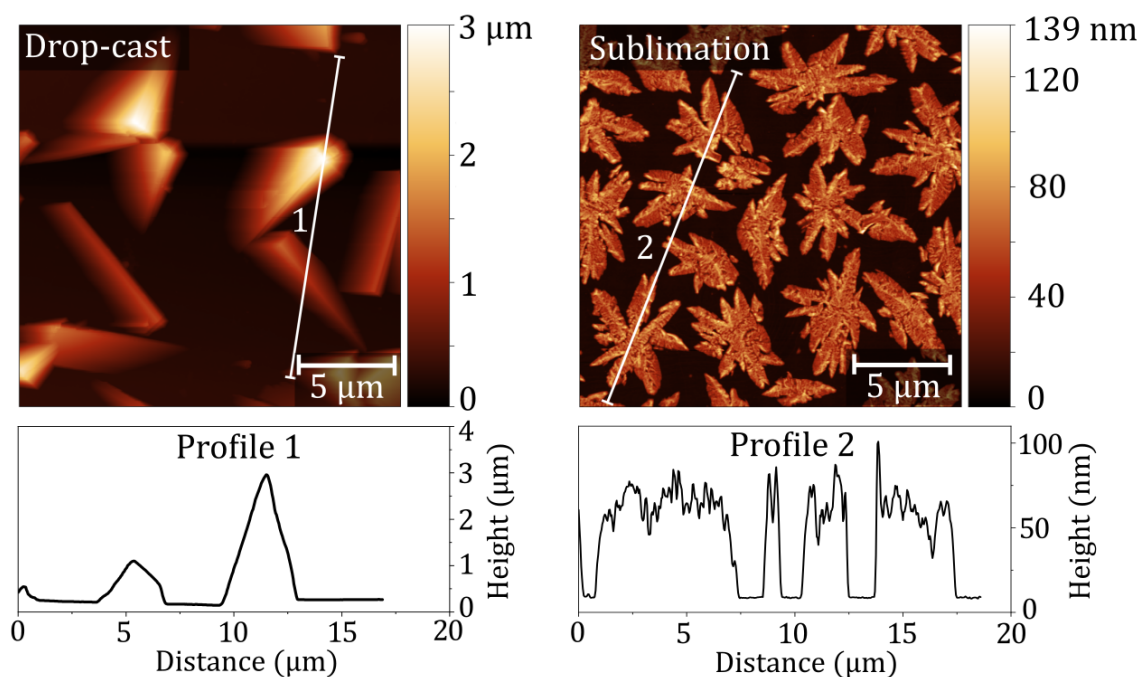


Fig. 3.25: AFM of the compound (2b) drop-casted and sublimated on graphene and height profiles along white lines 1 and 2.

Raman spectroscopy was performed to compare the vibrational modes of the individual components of the resulting hybrid material. Fig. 3.26 shows Raman spectra from top to bottom of a SiO₂/Si + CVD graphene, powder of (2b), deposited (2b) on graphene by drop-casting and by thermal sublimation. The Raman spectrum of CVD graphene on SiO₂/Si was described in 3.2. The Raman spectrum of the bulk compound (1) contained peaks characteristic for the ligand's functional groups such as imino or aromatic C=C/N bonds (ca. 1400–1620 cm⁻¹) or the phenolic group (1200–1300 cm⁻¹) [64]. We chose to use following the most intensive peaks for comparison of the bulk and deposited materials (in cm⁻¹): 1226, 1349, 1421, 1561 and 1603 (Fig. 3.20). As can be seen from Fig. 3.26 the Raman spectra of hybrid materials prepared either by wet or sublimation techniques confirmed the presence of all the peaks observed for the bulk material and also all the spectral patterns agree exceptionally well.

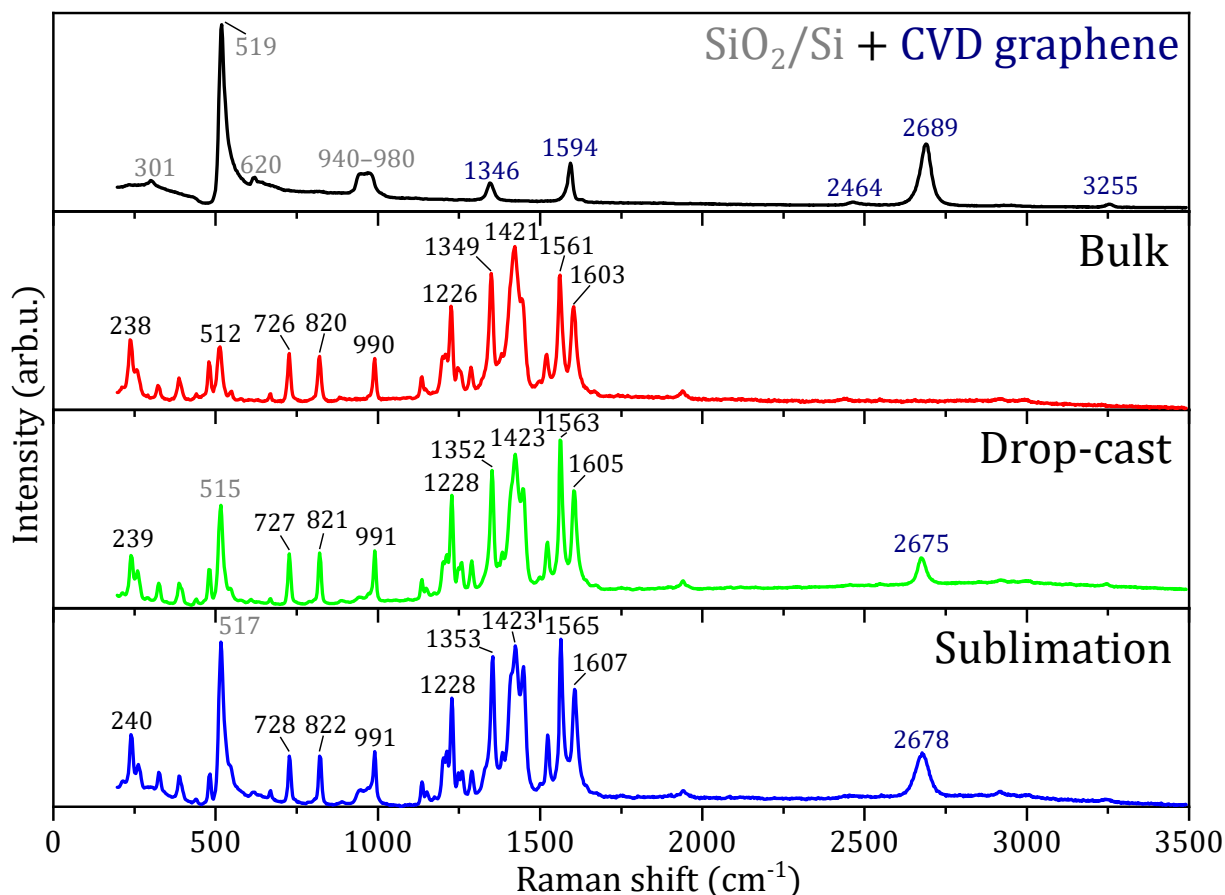


Fig. 3.26: Comparison of Raman spectra, from top to bottom, of SiO₂/Si substrate (Raman shift values marked in grey) and CVD graphene (in dark blue), bulk (2b), deposited (2b) on graphene by drop-casting and by thermal sublimation (marked in black).

The chemical composition was probed by XPS. Fig. 3.27 shows the comparison of XPS spectra for bulk and sublimated samples. All survey spectra exhibited photoelectron peaks: Co 2p, N 1s, C 1s, and O 1s; and Augers peaks: O_{KLL} and Co_{LMM}. Both Co 2p peaks exhibited two main components Co 2p_{3/2} and Co 2p_{1/2} and shake-up satellites. The spin-orbit shift of the main components Co 2p_{3/2} and Co 2p_{1/2} $\Delta = 15.5$ eV corresponds to Co(II) in the high-spin state [65]. Satellites intensity slightly increased after sublimation.

In case of N 1s, peak is deconvoluted by 4 components: at 399.1 eV – corresponding to pyridinic nitrogen in the ligand [74], the smallest peak at 405.7 eV may be attributed to shake-up satellite [73]. Small peaks at 400–404 eV may be corresponding to a nitrogen impurity. As the peak position of these nitrogen types varies in a relatively wide range in different studies, we were unable to determine the exact type [77]. In case of sublimated sample, one unidentified peaks appears at 399.9 eV.

Detailed spectra of O 1s and C 1s are not shown since they are affected by adventitious contaminations due to the ex-situ preparation procedures.

3.7. COMPOUND (2B)

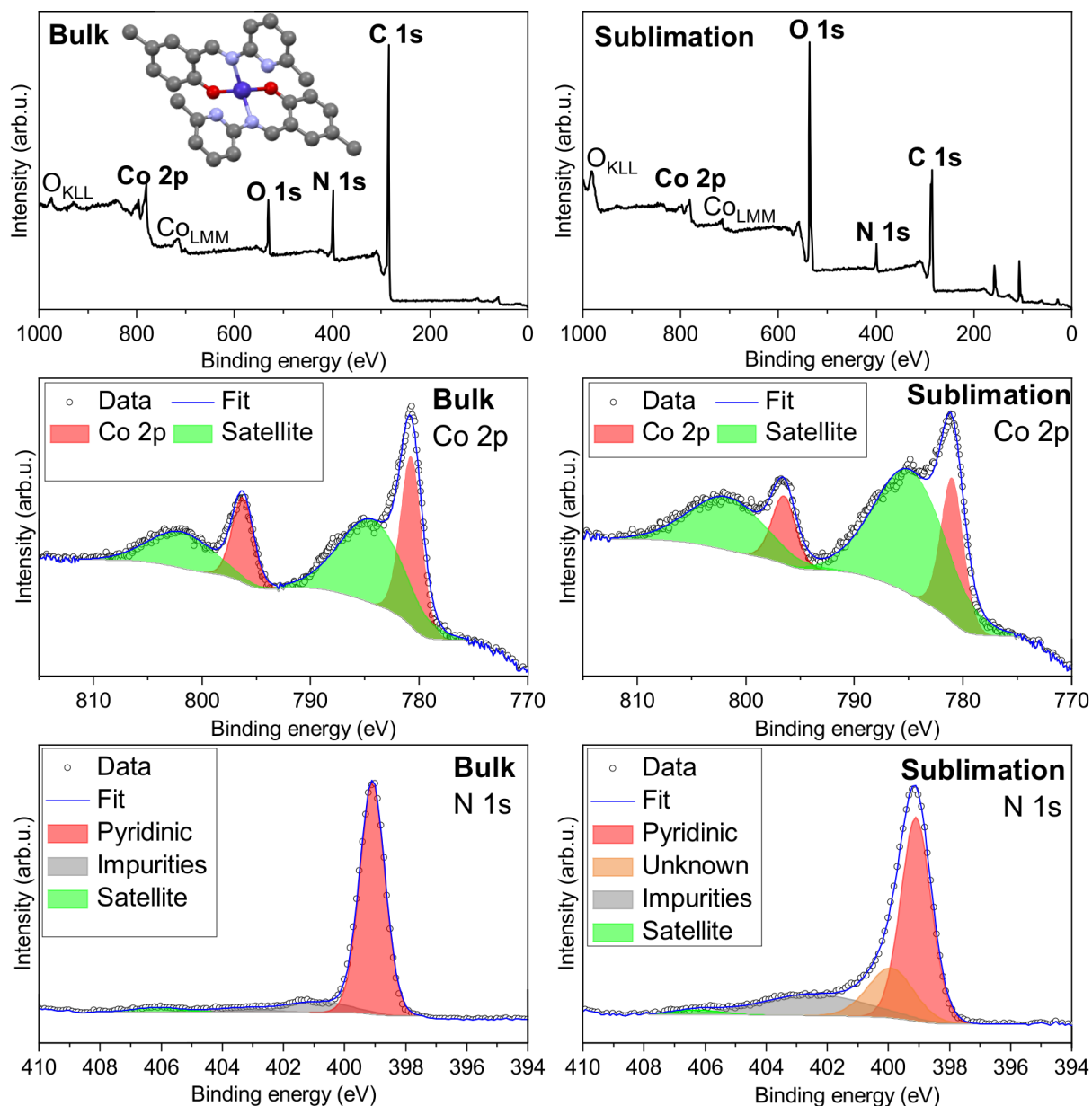


Fig. 3.27: Comparison of XPS spectra of the bulk (2b) and sublimated (2b) on graphene.

In the case of the drop-cast, it was not possible to compare the spectra because we found that the sample was X-ray damaged or partially charged during the measurements. This is shown in Fig. 3.28 of the detailed nitrogen spectrum, where on the left – the peak after 2 scans is composed of two components, while on the right – after 25 scans, another component appears.

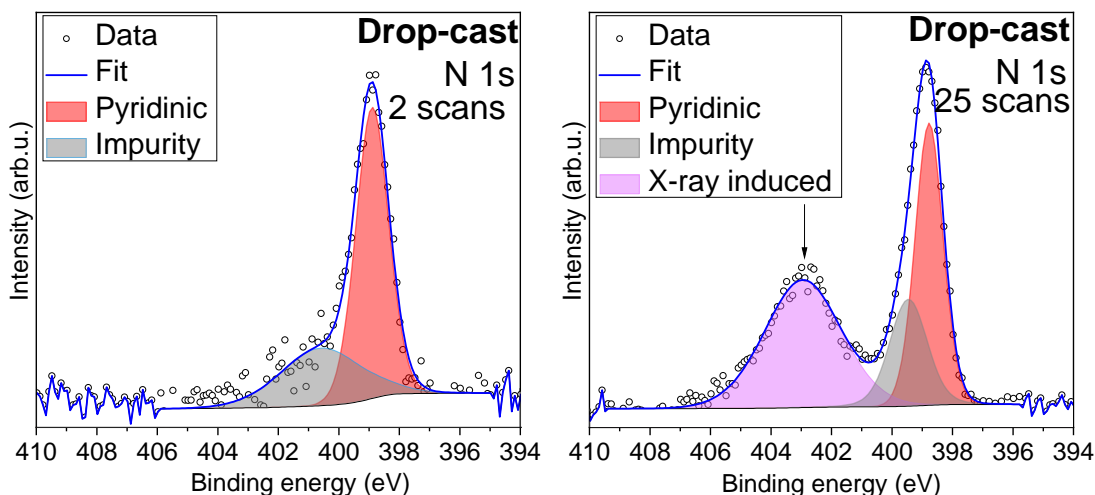


Fig. 3.28: Comparison of XPS spectra of the compound (2b) drop-casted on graphene depending on the number of scans.

In the case of sublimation, we observed subtle changes in the nitrogen and cobalt peaks. Considering the agreement of the Raman spectra, we can assume that most of the molecules of compound (2b) are preserved. In the case of the drop-cast, we cannot rely on XPS measurements, but the agreement of the Raman spectra suggests that the molecules could also remain stable during the deposition by wet chemistry.

3.8. Compound (3a)

The fifth examined SIM was dichloro-bis(2-dimethylaminoethyl)methylamine-cobalt(II), shortly $[\text{Co}(\text{Me}_5\text{dien})\text{Cl}_2]$ whose chemical structure is shown in the Fig. 3.29. Within this thesis, this compound is denoted 3a. The molecular formula of this compound is $\text{C}_9\text{H}_{23}\text{Cl}_2\text{CoN}_3$ and molar mass 303.138 g/mol. This compound was synthesized in the form of dark blue powder by Mgr. Lubomír Havlíček (CEITEC VUT) adapting previously reported synthetic procedure [75].

By measuring and fitting the VSM data, the magnetic properties were determined as $g_{\text{iso}} = 2.166$, $D = -20.60 \text{ cm}^{-1}$ and $E/D = 0.23$. The figure is provided in the attachment to this thesis.

Thermal sublimation was carried out at 203 °C at the pressure in the order of 10^{-7} mbar. The TGA analysis of a similar compound (3b) was previously measured, which indicates the beginning of the decomposition of the molecule above this temperature (a graph is provided in the attachment). The sublimation ended when QCM showed a layer thickness of 150 Å.

3.8. COMPOUND (3A)

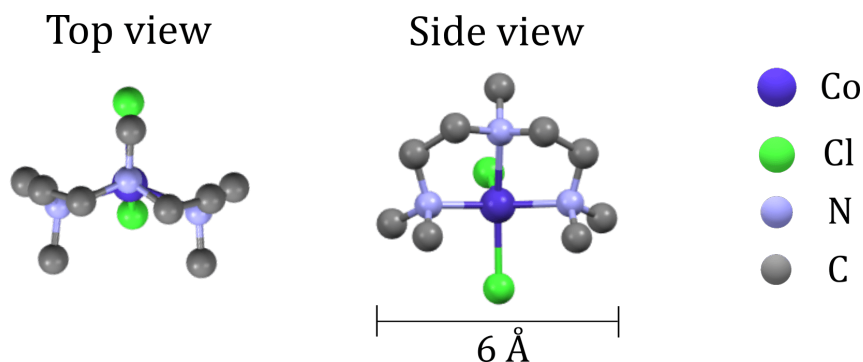


Fig. 3.29: Molecular structure of the compound (3a). Hydrogen atoms are omitted for the sake of clarity.

A comparison of the Raman spectra (see Fig. 3.32) showed that graphene was not present in the resulting hybrid material. This situation has been explained and described for the second compound in section 3.5. Therefore, we will refer to the sample missing graphene as modified SiO₂/Si.

An optical image of the resulting sample is shown in the Fig. 3.30a, where we can see that round islands have formed on the surface along with less common elongated crystals. Using AFM (Fig. 3.30b), the height of the round islands was determined to be within 100 nm.

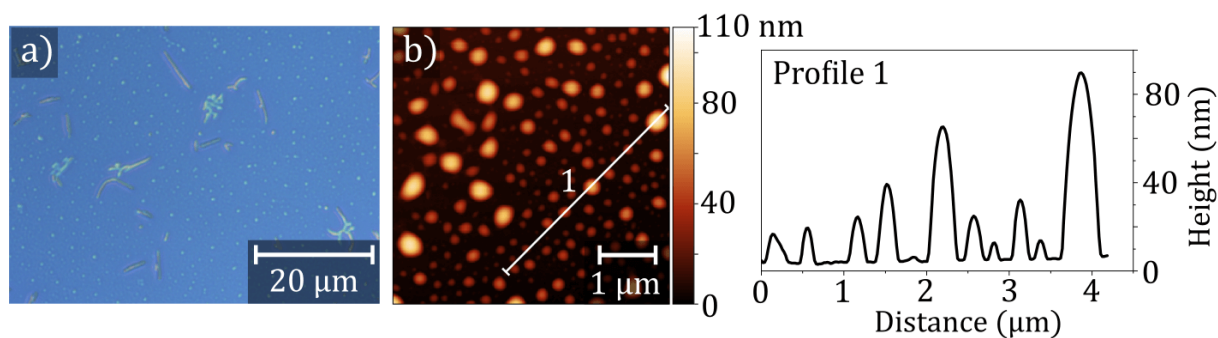


Fig. 3.30: a) Optical image of the (3a) sublimated on modified SiO₂/Si. b) AFM image of the same sample and the height profile along the white line 1.

A more detailed perspective and comparison of surfaces were provided by SEM. From Fig. 3.31a and 3.31b we see that there is no difference between the samples with SiO₂/Si and modified SiO₂/Si. For comparison of what this could look like on graphene, an image from thermal sublimation of (3a) on graphene was performed at Georgetown University by Mgr. Lubomír Havlíček is shown in Fig. 3.31c.

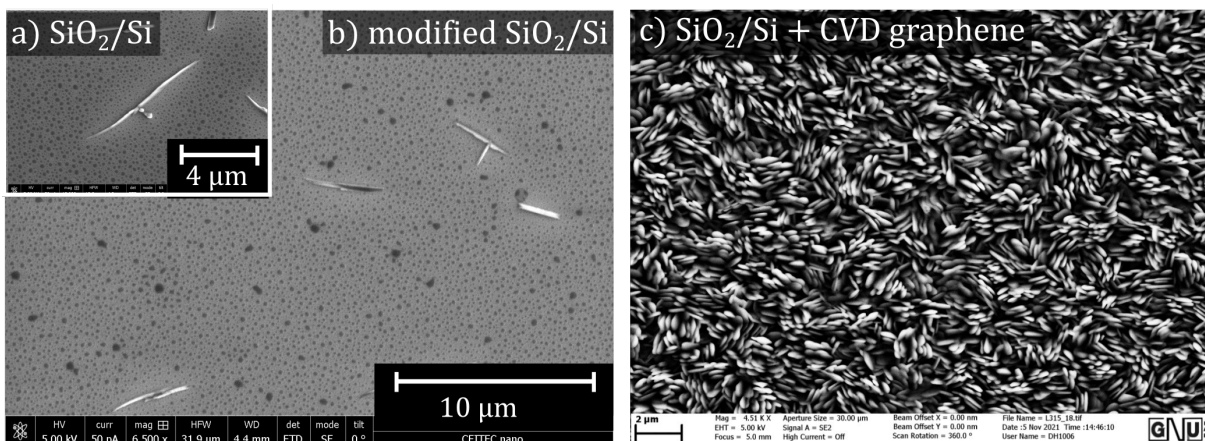


Fig. 3.31: Comparison of SEM images of (3a) sublimated on a) SiO₂/Si, b) sample with modified SiO₂/Si and c) on graphene performed at Georgetown University by Mgr. Lubomír Havlíček.

Raman spectroscopy was performed to compare the vibrational modes of the individual components of the resulting hybrid material. Fig. 3.32 shows Raman spectra, from top to bottom, of a SiO₂/Si + CVD graphene, powder of (3a) and deposited (3a) by thermal sublimation. The Raman spectrum of CVD graphene on SiO₂/Si was described in 3.2. The Raman spectrum of the bulk compound (3a) contains peaks characteristic of the ligand's functional groups such as amine, ethyl, and methyl (the strongest peaks at 2800-3000 cm⁻¹ are attributed to aliphatic C-H bonds) [50, 64].

In the case of a sublimated sample, except for the SiO₂/Si peaks, the weak signal of the strongest vibrations of the deposited molecules of (3a) is distinguished.

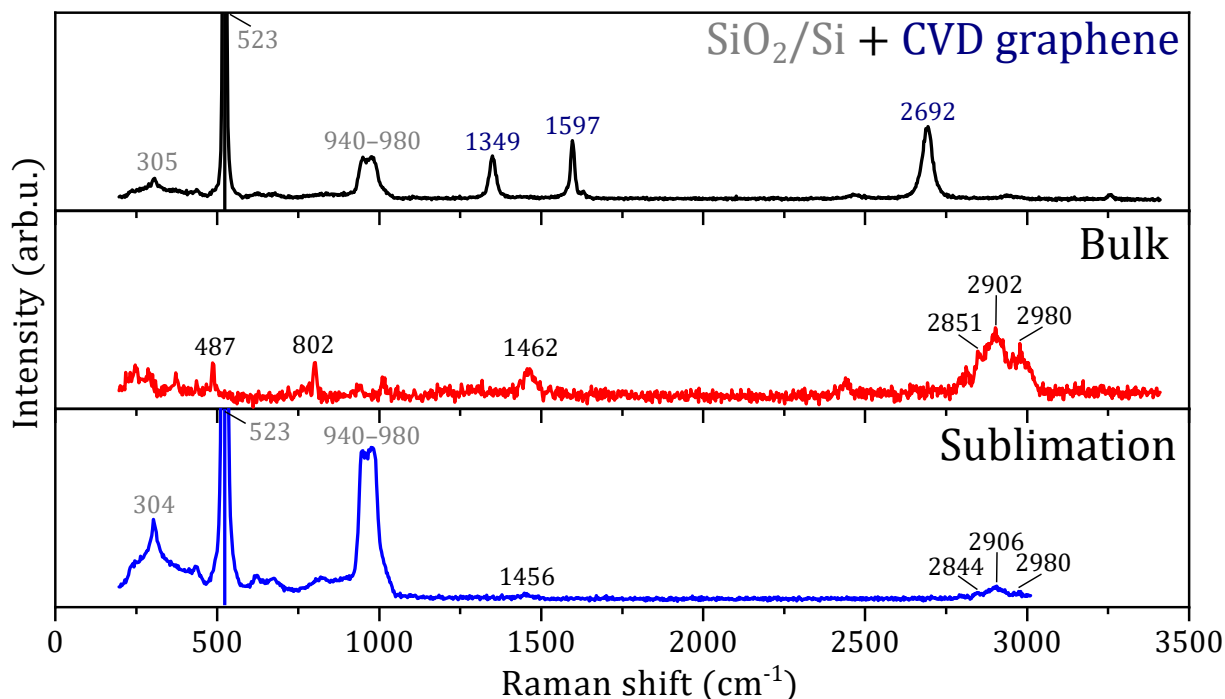


Fig. 3.32: Comparison of Raman spectra, from top to bottom, of SiO₂/Si substrate (Raman shift values marked in grey) and CVD graphene (marked in dark blue), bulk (3a) and deposited (3a) by thermal sublimation (marked in black).

3.8. COMPOUND (3A)

The chemical composition was also probed by XPS. Fig. 3.33 shows the comparison of XPS spectra for bulk and sublimated sample. Both survey spectra exhibit photoelectron peaks: Co 2p, N 1s, C 1s, and O 1s; and Augers peaks: O_{KLL} and Co_{LMM}.

The detailed Co 2p peak of the bulk exhibits two spin-orbit split peaks Co 2p_{3/2} and Co 2p_{1/2} and shake-up satellites, which are common with paramagnetic states [53]. The spin-orbit shift of the main components Co 2p_{3/2} and Co 2p_{1/2} $\Delta = 15.5$ eV corresponds to Co(II) in the high-spin state [65]. For simplicity, only the Co 2p_{3/2} peak is fit. Both Co 2p_{3/2} peaks of the bulk and sublimated sample consist of two main components and three satellites.

As for chloride Cl 2p, two pairs of Cl 2p_{3/2} and Cl 2p_{1/2} components with spin-orbit splitting $\Delta = 1.6$ eV are observed [53]. The position of the 2p_{3/2} main peak (≈ 198 eV) is consistent with metal chloride [76]. In the case of the sublimated sample, the main metal chloride component is still present and a smaller component at higher binding energy appears at 199.9 eV, which can be attributed to organic chloride [66].

In the case of N 1s of the bulk, the peak includes two components. The main component corresponds to the amine at 400.1 eV, and the origin of the smaller peak at 402.4 eV remains unknown [67].

Detailed spectra of O 1s and C 1s are not shown since they are affected by adventitious contaminations due to the ex-situ preparation procedures.

No significant change in the XPS spectra after sublimation was observed and we can therefore assume the conservation of the compound (3a) after deposition.

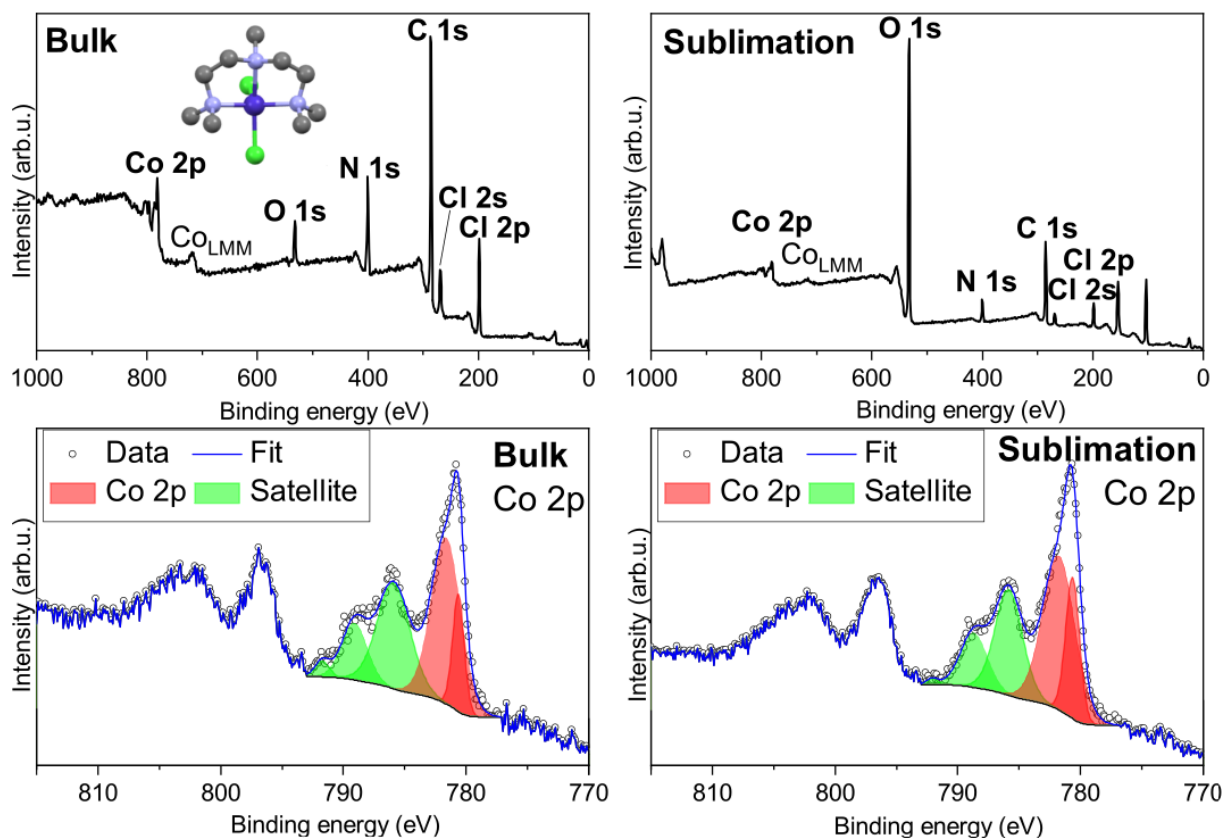


Fig. 3.33: Comparison of XPS survey spectra and Co 2p peak of the bulk (3a) and sublimated (3a) on modified SiO₂/Si.

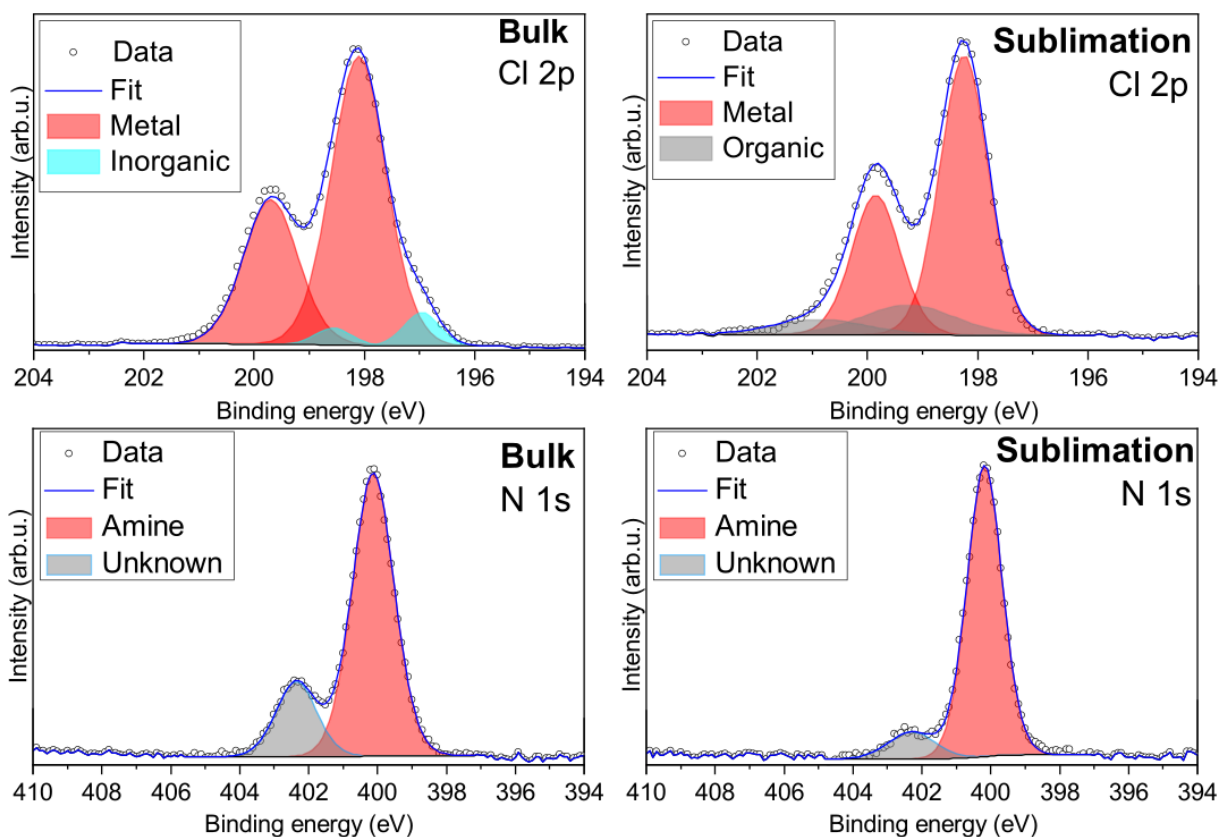


Fig. 3.34: Comparison of XPS spectra of the Cl 2p and N 1s peaks of the bulk (3a) and sublimated (3a) on modified SiO₂/Si.

3.9. Compound (3b)

The sixth examined SIM was 1,1,7,7-Tetraethyldiethylenetriamine-cobalt(II)-chloride, shortly [Co(Et₄dien)Cl₂] whose chemical structure is shown in the Fig. 3.35. As can be seen, the compound is similar to the previous compound, except that the methyl groups were replaced by ethyl substituents. Therefore this compound is labeled 3b. The molecular formula of this compound is C₁₂H₂₉Cl₂CoN₃ and molar mass 345.218 g/mol. This compound was synthesized in the form of purple powder by Mgr. Lubomír Havlíček (CEITEC VUT) adapting previously reported synthetic procedure [75].

By measuring and fitting the VSM data, the magnetic properties were determined as $g_{\text{iso}} = 2.32$, $D = -13.0 \text{ cm}^{-1}$ and $E/D = 0.26$. The figure is provided in the attachment to this thesis.

Thermal sublimation was carried out at 216 °C at a pressure in the order of 10⁻⁷ mbar. The measured TGA analysis of this compound demonstrates the initiation of the decomposition of the molecules at a higher temperature than this (a graph is provided in the attachment). The sublimation ended when QCM showed a layer thickness of 210 Å.

3.9. COMPOUND (3B)

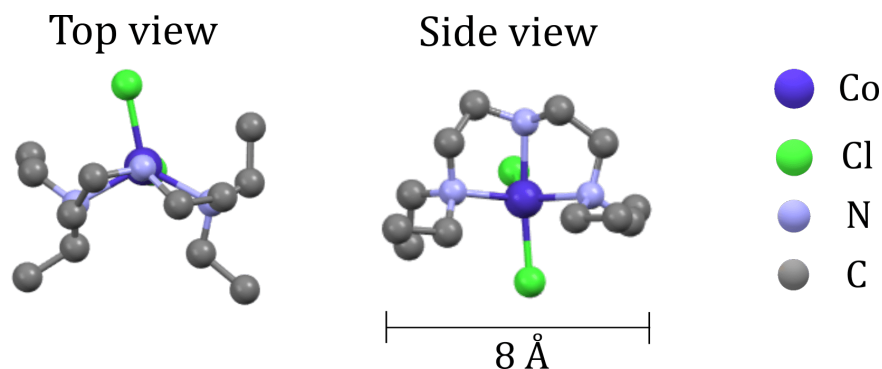


Fig. 3.35: Molecular structure of the compound (3b). Hydrogen atoms are omitted for the sake of clarity.

From Fig. 3.36 can be observed that the substrate is inhomogeneously covered. In one part of the sample, there are mounds up to 200 nm high, while in the other, there are 2-3× higher and less abundant mounds.

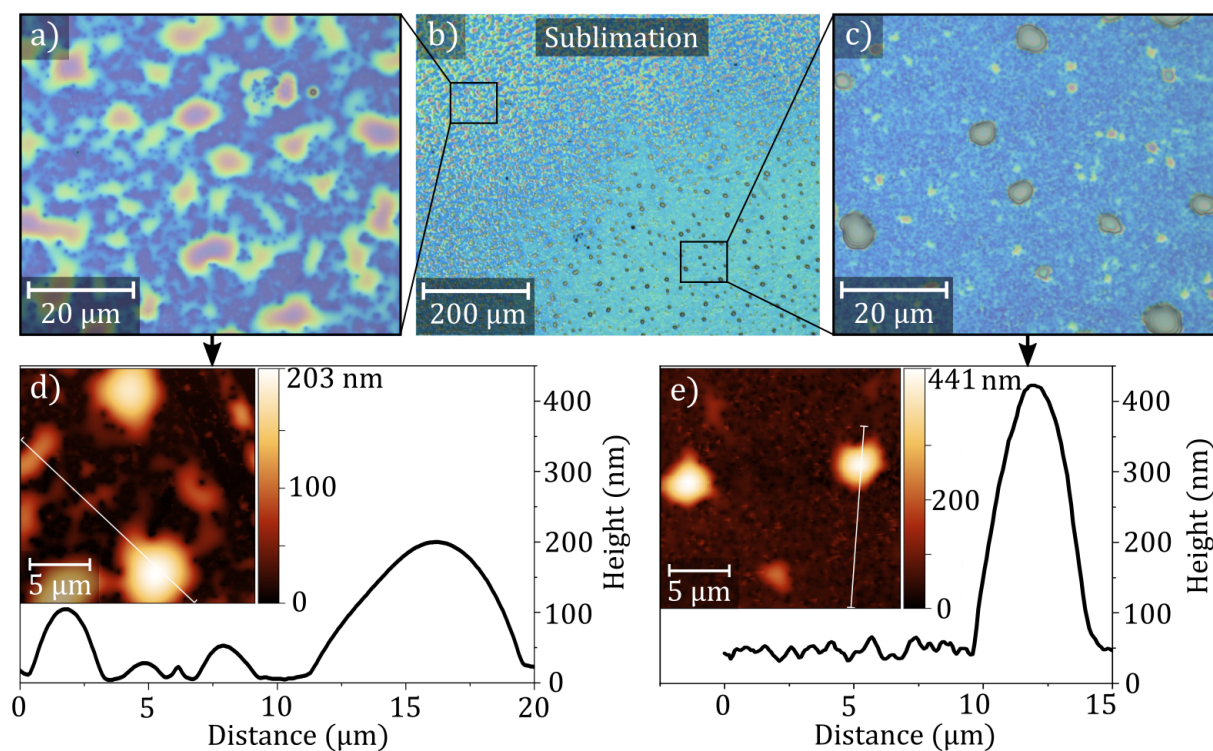


Fig. 3.36: b) Optical image of the (3b) sublimated on graphene, a) and c) shows the details of the different coverage. d) and e) represent AFM images of the coverage type from an area above and the height profiles along the white lines.

Raman spectroscopy was performed to compare the vibrational modes of the individual components of the resulting hybrid material. Fig. 3.37 shows the comparison of Raman spectra, from top to bottom, of a SiO₂/Si + CVD graphene, powder of (3b) and deposited (3b) by thermal sublimation. The Raman spectrum of CVD graphene on SiO₂/Si was described in 3.2. The Raman spectrum of the bulk compound (3a) contains peaks characteristic of the ligand's functional groups such as amine, ethyl and methyl (the strongest peaks at 2800-3000 cm⁻¹ are attributed to aliphatic C-H bonds) [50, 64].

In the case of a sublimated sample, the weak signal of the strongest vibrations of the deposited molecules of (3b) is distinguished.

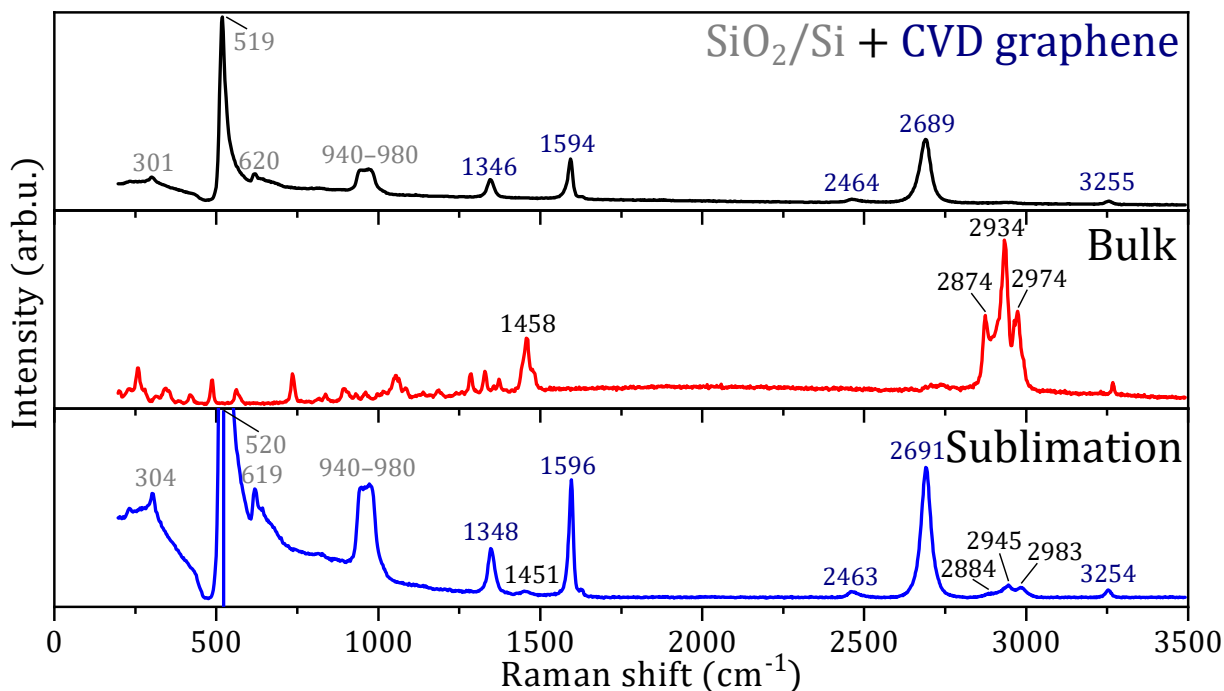


Fig. 3.37: Comparison of Raman spectra, from top to bottom, of SiO_2/Si substrate (Raman shift values marked in grey) and CVD graphene (marked in dark blue), bulk (3b), deposited (3b) by drop-cast and by thermal sublimation (marked in black).

The chemical composition was also probed by XPS. Fig. 3.38 shows the comparison of XPS spectra for bulk and sublimated sample. Both survey spectra exhibit photoelectron peaks: Co 2p, N 1s, C 1s, and O 1s; and Augers peaks: O_{KLL} and Co_{LMM} .

The detailed Co 2p peak of the bulk exhibits two spin-orbit split peaks Co 2p_{3/2} and Co 2p_{1/2} and shake-up satellites, which are common with paramagnetic states [53]. The spin-orbit shift of the main components Co 2p_{3/2} and Co 2p_{1/2} $\Delta = 15.5$ eV corresponds to high-spin state [65]. Both Co 2p_{3/2} peaks of the bulk and sublimated sample consist of two main components and two satellites.

As for chloride Cl 2p, two pairs of Cl 2p_{3/2} and Cl 2p_{1/2} components with spin-orbit splitting $\Delta = 1.6$ eV are observed [53]. The position of the 2p_{3/2} main peak (≈ 198 eV) is consistent with metal chloride [76]. Smaller peak at 198.9 may be attributed to inorganic chloride [66]. In the case of the sublimated sample, the main metal chloride component is still present and a smaller component at higher binding energy appears at 199.9 eV, which can be attributed to organic chloride [66].

In the case of N 1s of the bulk, the peak includes two components. The main component corresponds to the amine at 399.9 eV, and the origin of the smaller peak at 401.2 eV may be attributed to impurity [67]. In the case of the sublimated sample, N 1s consists of the main amine peak, and the second unidentified peak at 402 eV appears.

Detailed spectra of O 1s and C 1s are not shown since they are affected by adventitious contaminations due to the ex-situ preparation procedures.

From the change in the peak of N 1s after sublimation, one can speculate that the part of the deposited molecules was chemically affected during the deposition process.

3.9. COMPOUND (3B)

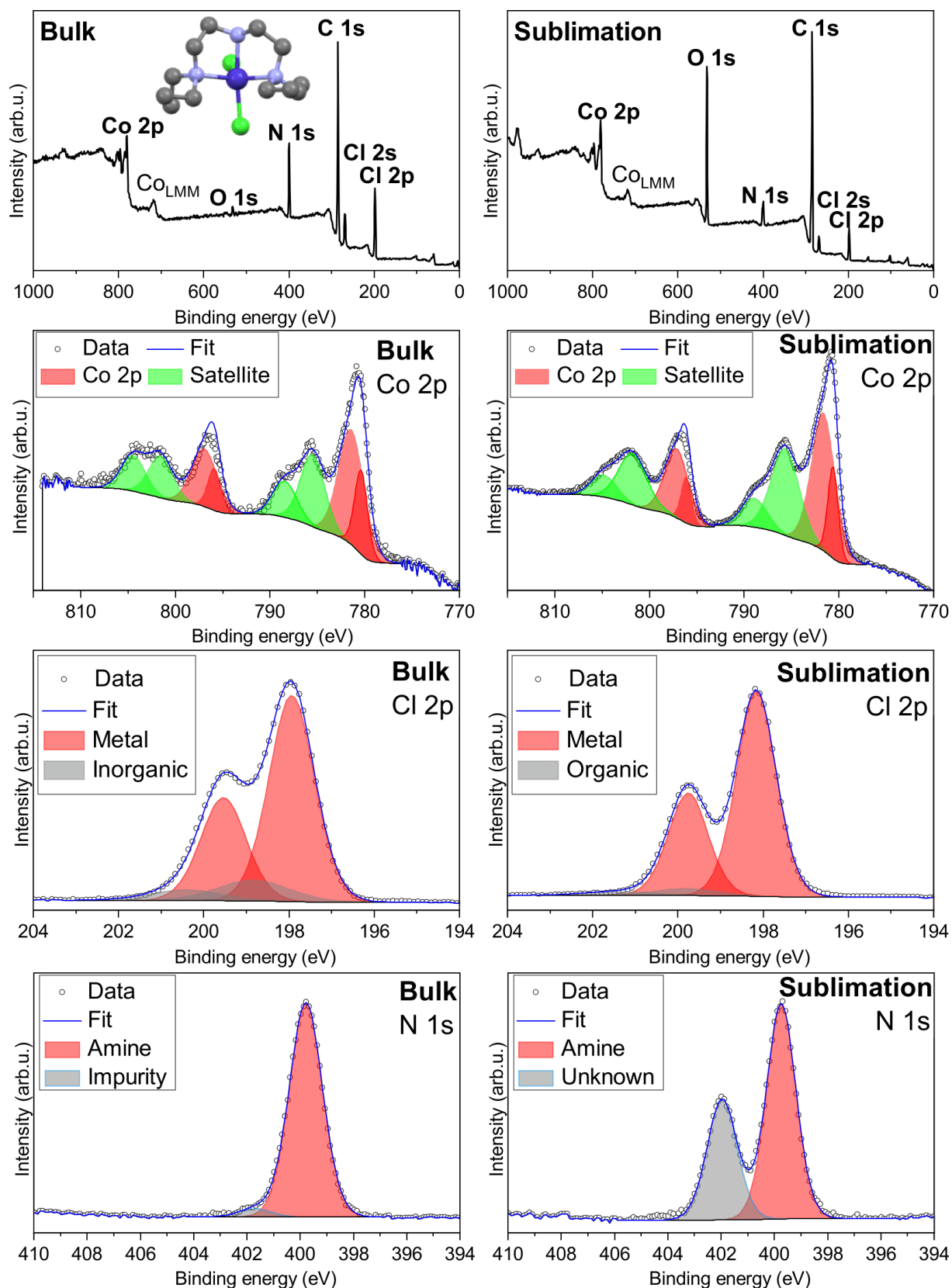


Fig. 3.38: Comparison of XPS spectra of the bulk (3b) and sublimated (3b) on graphene.

4. Conclusions

The aim of this thesis was to perform the deposition of cobalt SIMs on graphene and to characterize the resulting hybrid material in terms of morphology, and chemical and magnetic properties.

In the theoretical part, the topic of SMMs and deposition methods were outlined. Graphene and the motivation for its use were then introduced. The physical principles of the characterization methods used in the experimental part (AFM, SEM, Raman spectroscopy, XPS and EPR) were also explained.

In the experimental part, the preparation of a hybrid material consisting of CVD graphene on silicon and a layer of SIMs was described. Six different cobalt(II)-based SIMs were selected for investigation in this work. Based on their similarity, they could be divided into pairs, in which they were always denoted as (a) and (b). The magnetic nature of these molecules has already been verified by VSM measurements and could also be observed in the XPS spectra. All six SIMs were deposited by thermal sublimation. Drop-cast deposition, belonging to the wet chemistry techniques, was also performed for two of them due to the expected high stability. Subsequently, the samples were characterized using the methods mentioned above.

For the first pair of compounds, (1a) and (1b), it was determined from XPS and Raman spectra that decomposition must have occurred during sublimation. This was carried out at a temperature of about 340 °C when a significant increase in the rate of sublimation could be observed. TGA analysis measured later revealed decomposition of the molecules at this temperature. The coverage of the sample observed by SEM and AFM was very weak in the order of nanometers in the case of (1a), even though a 15 nm thick layer was deposited according to QCM. For compound (1b), the coverage was in the form of coalescing irregular islands up to 100 nm in height, where 50 nm was deposited according to QCM.

The second pair of compounds (2a) and (2b) were successfully deposited by both drop-casting under ambient conditions and thermal sublimation with the agreement of Raman and XPS spectra. In the case of drop-casting, these compounds formed micrometer-sized crystals, and in the case of sublimation, they formed separate islands resembling the shape of flakes. These reached heights of up to 100–150 nanometres, whereas the QCM suggested that there should be a 20 nm thick layer.

In the case of the third pair of compounds (3a) and (3b), no change in spectra of bulk deposited molecules was observed for (3a), and therefore we expect that it remained unchanged during deposition. The substrate was covered with round islands up to 100 nm high with the occasional appearance of a larger crystal (QCM suggested 15 nm thick layer). For the second compound (3b), a chemical change in some of the molecules could be speculated from the change in the XPS spectrum of the nitrogen peak. TGA analysis did not show thermal decomposition at the temperature used for sublimation (216 °C). On the surface, it formed a thin layer (tens of nanometres) with inhomogeneously occurring pointed round islands up to 400 nm. The QCM showed 23 nm layer thickness after sublimation.

In this work, magnetically interesting and sufficiently stable Co(II) SIMs were identified that resisted both the air humidity and drop-cast deposition without a protective atmosphere. Therefore, these SIMs deserve further attention and study of the deposited layers, for example, by using a graphene bolometer in EPR. This work also revealed the

importance of verifying the thermal stability of the compound (e.g., by TGA analysis) prior to thermal sublimation to avoid decomposition of the molecules due to high temperature. However, such depositions had an educational role in learning how to recognize and identify unsuccessful depositions.

Bibliography

- [1] SESSOLI, Roberta, et al. Magnetic bistability in a metal-ion cluster. *Nature*, 1993, 365.6442: 141-143.
- [2] FROST, Jamie M.; HARRIMAN, Katie LM; MURUGESU, Muralee. The rise of 3-d single-ion magnets in molecular magnetism: towards materials from molecules?. *Chemical science*, 2016, 7.4: 2470-2491.
- [3] GUO, Fu-Sheng, et al. Magnetic hysteresis up to 80 kelvin in a dysprosium metal-locene single-molecule magnet. *Science*, 2018, 362.6421: 1400-1403.
- [4] BOGANI, Lapo; WERNSDORFER, Wolfgang. Molecular spintronics using single-molecule magnets. *Nanoscience and technology: a collection of reviews from nature journals*. 2010. p. 194-201.
- [5] SESSOLI, Roberta. Toward the quantum computer: magnetic molecules back in the race. *ACS Publications* 2015. p. 473-474.
- [6] CANESCHI, Andrea; GATTESCHI, Dante; TOTTI, Federico. Molecular magnets and surfaces: A promising marriage. A DFT insight. *Coordination Chemistry Reviews*, 2015, 289: 357-378.
- [7] ATANASOV, Mihail, et al. First principles approach to the electronic structure, magnetic anisotropy and spin relaxation in mononuclear 3d-transition metal single molecule magnets. *Coordination Chemistry Reviews*, 2015, 289: 177-214.
- [8] ST MARIE, Luke, et al. Nanostructured graphene for nanoscale electron paramagnetic resonance spectroscopy. *Journal of Physics: Materials*, 2020, 3.1: 014013.
- [9] NEESE, Frank; PANTAZIS, Dimitrios A. What is not required to make a single molecule magnet. *Faraday discussions*, 2011, 148: 229-238.
- [10] CHRISTOU, George, et al. Single-molecule magnets. *Mrs Bulletin*, 2000, 25.11: 66-71.
- [11] AKO, Ayuk M., et al. A ferromagnetically coupled Mn₁₉ aggregate with a record S=83/2 ground spin state. *Angewandte Chemie*, 2006, 118.30: 5048-5051.
- [12] ISHIKAWA, Naoto, et al. Lanthanide double-decker complexes functioning as magnets at the single-molecular level. *Journal of the American Chemical Society*, 2003, 125.29: 8694-8695.
- [13] FREEDMAN, Danna E., et al. Slow magnetic relaxation in a high-spin iron (II) complex. *Journal of the American Chemical Society*, 2010, 132.4: 1224-1225.
- [14] LIS, Thomas. Preparation, structure, and magnetic properties of a dodecanuclear mixed-valence manganese carboxylate. *Acta Crystallographica Section B: Structural Crystallography and Crystal Chemistry*, 1980, 36.9: 2042-2046.

BIBLIOGRAPHY

- [15] ZHU, Xiaochen, et al. Electronegative ligands enhance charge transfer to Mn12 single-molecule magnets deposited on graphene. *Journal of Applied Physics*, 2020, 127.6: 064303.
- [16] CAVALLINI, Massimiliano, et al. Single molecule magnets: from thin films to nanopatterns. *Physical Chemistry Chemical Physics*, 2008, 10.6: 784-793.
- [17] CLEMENTE-LEÓN, Miguel, et al. Langmuir–Blodgett Films of Single-Molecule Nanomagnets. *Angewandte Chemie International Edition*, 1998, 37.20: 2842-2845.
- [18] SEO, Di. M., et al. Enhanced magnetic anisotropy of Mn12-acetate. *Journal of magnetism and magnetic materials*, 2006, 301.1: 31-36.
- [19] LANZILOTTO, Valeria, et al. The challenge of thermal deposition of coordination compounds: Insight into the case of an Fe4 single molecule magnet. *Chemistry of materials*, 2016, 28.21: 7693-7702.
- [20] O’SULLIVAN, Ciara. K.; GUILBAULT, George. G. Commercial quartz crystal microbalances—theory and applications. *Biosensors and bioelectronics*, 1999, 14.8-9: 663-670.
- [21] SAYWELL, Alex, et al. Self-assembled aggregates formed by single-molecule magnets on a gold surface. *Nature communications*, 2010, 1.1: 1-8.
- [22] PASCHKE, Fabian, et al. Electrospray Deposition and Magnetic Properties of Prototypical Molecular Magnets. *Quantum Materials Research*, 2020, 1.
- [23] BELLIDO, Elena, et al. Mn 12 single molecule magnets deposited on -SQUID sensors: the role of interphases and structural modifications. *Nanoscale*, 2013, 5.24: 12565-12573. 306.5696: 666-669.
- [24] NOVOSELOV, Kostya S., et al. Electric field effect in atomically thin carbon films. *Science*, 2004, 306.5696: 666-669.
- [25] NETO, AH Castro, et al. The electronic properties of graphene. *Reviews of modern physics*, 2009, 81.1: 109.
- [26] DO, Thi-Nga, et al. Atomistic Band-Structure Computation for Investigating Coulomb Dephasing and Impurity Scattering Rates of Electrons in Graphene. *Nanomaterials*, 2021, 11.5: 1194.
- [27] MAYOROV, Alexander S., et al. Micrometer-scale ballistic transport in encapsulated graphene at room temperature. *Nano letters*, 2011, 11.6: 2396-2399.
- [28] BALANDIN, Alexander A. Thermal properties of graphene and nanostructured carbon materials. *Nature materials*, 2011, 10.8: 569-581.
- [29] NAIR, Rahul Raveendran, et al. Fine structure constant defines visual transparency of graphene. *Science*, 2008, 320.5881: 1308-1308.
- [30] LEE, Changgu, et al. Measurement of the elastic properties and intrinsic strength of monolayer graphene. *Science*, 2008, 321.5887: 385-388.

- [31] MORTAZAVI, Bohayra, et al. Mechanical responses of borophene sheets: a first-principles study. *Physical Chemistry Chemical Physics*, 2016, 18.39: 27405-27413.
- [32] NOVOSELOV, Konstantin S., et al. A roadmap for graphene. *Nature*, 2012, 490.7419: 192-200.
- [33] FERRARI, Andrea C.; BASKO, Denis M. Raman spectroscopy as a versatile tool for studying the properties of graphene. *Nature nanotechnology*, 2013, 8.4: 235-246.
- [34] DENG, Bing; LIU, Zhongfan; PENG, Hailin. Toward mass production of CVD graphene films. *Advanced Materials*, 2019, 31.9: 1800996.
- [35] FERRARI, Andrea C., et al. Raman spectrum of graphene and graphene layers. *Physical review letters*, 2006, 97.18: 187401.
- [36] BLAKE, Peter., et al. Making graphene visible. *Applied physics letters*, 2007, 91.6: 063124.
- [37] EL FATIMY, Abdel, et al. Epitaxial graphene quantum dots for high-performance terahertz bolometers. *Nature nanotechnology*, 2016, 11.4: 335-338.
- [38] Atomic Force Microscope. Atomic Force Microscope - an overview | ScienceDirect Topics. (n.d.). Retrieved May 16, 2022, from <https://www.sciencedirect.com/topics/engineering/atomic-force-microscope>
- [39] BINNIG, Gerd; QUATE, Calvin F.; GERBER, Ch. Atomic force microscope. *Physical review letters*, 1986, 56.9: 930.
- [40] ISRAELACHVILI, Jakob. *Intermolecular and surface forces*. 2nd ed. London: Academic Press, 1992. ISBN 0-12-375181-0.
- [41] TURČAN, Igor. *Mikroskopie magnetických sil v proměnném magnetickém poli*. 2014. ISBN 9780874216561.
- [42] HAUGSTAD, Greg. *Atomic force microscopy exploring basic modes and advanced applications*. First edition. Hoboken, N.J: John Wiley & Sons, Inc., 2012. ISBN 978-111-8360-668.
- [43] DE BROGLIE, Louis. *Recherchessur la théoriesdesquanta* (Doctoraldissertation), Migration-université en cours d'affectation. 1924.
- [44] REIMER, Ludwig. *Scanning electron microscopy: physics of image formation and microanalysis*. 2000.
- [45] UPPUTURI, Paul Kumar; PRAMANIK, Manojit. Microsphere-aided optical microscopy and its applications for super-resolution imaging. *Optics Communications*, 2017, 404: 32-41.
- [46] ZWORYKIN, Vladimir K. The scanning electron microscope. *Scientific American*, 1942, 167.3: 111-113.
- [47] "The Scanning Electron Microscope." *Engineering Atoms*, June 25, 2015. Available from: <https://www.eng-atoms.msm.cam.ac.uk/RoyalSocDemos/SEM>.

BIBLIOGRAPHY

- [48] WALOCK, Michael. *Nanocomposite coatings based on quaternary metalnitrogen*. Paris, 2012. Doctoral thesis. Ecole nationale supérieure d'arts et métiers - ENSAM; University of Alabama at Birmingham.
- [49] RAMAN, Chandrasekhara Venkata; KRISHNAN, Kariamanikkam Srinivasa. A new type of secondary radiation. *Nature*, 1928, 121.3048: 501-502.
- [50] LARKIN, Peter. *Infrared and Raman spectroscopy: principles and spectral interpretation*. Elsevier, 2017.
- [51] SMITH, Ewen; DENT, Geoffrey. *Modern Raman spectroscopy: a practical approach*. John Wiley & Sons, 2019.
- [52] KLASSEN, Stephen, et al. Portrayal of the history of the photoelectric effect in laboratory instructions. *Science & Education*, 2012, 21.5: 729-743.
- [53] MOULDER, John F. et al. *Handbook of X-Ray Photoelectron Spectroscopy: A Reference Book of Standard Spectra for Identification and Interpretation of XPS Data*. 1st ed. Perkin-Elmer Corporation, 1992. ISBN 978-0964812413.
- [54] "XPS and UPS Background." Grimmgroup Research. Accessed May 9, 2022. Available from: <https://grimmgroup.net/research/xps/background/>.
- [55] WEIL, John A.; BOLTON, James R. *Electron paramagnetic resonance: elementary theory and practical applications*. John Wiley & Sons, 2007.
- [56] HRUBÝ, Jakub. *High Frequency Electron Spin Resonance Spectroscopy*. Brno, 2021. 119 s. Doctoral thesis. Brno University of Technology. Central European Institute of Technology BUT. Supervisor: Petr NEUGEBAUER.
- [57] SHIRLEY, Dave A. High-resolution X-ray photoemission spectrum of the valence bands of gold. *Physical Review B*, 1972, 5.12: 4709.
- [58] STOLL, Stefan.; SCHWEIGER, Arthur. EasySpin, a comprehensive software package for spectral simulation and analysis in EPR. *Journal of Magnetic Resonance*, 2006, 178, 42–55.
- [59] SPIZZIRRI, Paul. et al. Nano-Raman spectroscopy of silicon surfaces. *arXiv preprint arXiv:1002.2692*, 2010.
- [60] HULMAN, Martin. Raman spectroscopy of graphene. *In: Graphene*. Woodhead Publishing, 2021. p. 381-411.
- [61] JIANG, Hui, et al. Syntheses, structures and characterization of cobalt (II) and cobalt (III) complexes with N-benzylated polyamines and a terminal azido ligand. *Journal of Coordination Chemistry*, 2003, 56.9: 825-832.
- [62] YOFFE, A. D. Thermal decomposition and explosion of azides. Proceedings of the Royal Society of London. *Series A. Mathematical and Physical Sciences*, 1951, 208.1093: 188-199.

- [63] MAZILU, Michael, et al. Optimal algorithm for fluorescence suppression of modulated Raman spectroscopy. *Optics express*, 2010, 18.11: 11382-11395.
- [64] SOCRATES, George. *Infrared and Raman characteristic group frequencies: tables and charts*. John Wiley & Sons, 2004.
- [65] PONETI, Giordano, et al. Magnetic and spectroscopic investigation of thermally and optically driven valence tautomerism in thioether-bridged dinuclear cobalt–dioxolene complexes. *Inorganic Chemistry*, 2013, 52.20: 11798-11805.
- [66] FIEDLER, Rainer; HERZSCHUH, Rainer. An XPS investigation of the effects of heat treatment on the chlorine surface chemistry of some lignites. *Fuel*, 1993, 72.11: 1501-1505.
- [67] SOLOMON, Edward I., et al. Variable energy photoelectron spectroscopy: electronic structure and electronic relaxation. *Coordination chemistry reviews*, 2005, 249.1-2: 229-253.
- [68] LANGE, Stefanie C., et al. Efficient and tunable three-dimensional functionalization of fully zwitterionic antifouling surface coatings. *Langmuir*, 2016, 32.40: 10199-10205.
- [69] XU, Li., et al. A new Co (II) complex with N, O-donor Schiff base: Synthesis, structure and characterization. *Journal of Structural Chemistry*, 2006, 47.5: 998-1001.
- [70] ZHAN, H. J., et al. Microwave Irradiation Synthesized Cobalt-Loaded Nitrogen-Doped Active Carbon as an Efficient Catalyst for Selective Oxidation of Ethylbenzene. *IOP Conference Series: Materials Science and Engineering*. IOP Publishing, 2019. p. 012004.
- [71] GOLDMANN, Anja S., et al. Surface modification of poly (divinylbenzene) microspheres via thiol–ene chemistry and alkyne–azide click reactions. *Macromolecules*, 2009, 42.11: 3707-3714.
- [72] MAY, Benjamin, et al. Surface-induced changes in the thermochromic transformation of an ionic liquid cobalt thiocyanate complex. *The journal of physical chemistry letters*, 2017, 8.6: 1137-1141.
- [73] LAHAYE, Jacques., et al. Porous structure and surface chemistry of nitrogen containing carbons from polymers. *Carbon*, 1999, 37.4: 585-590.
- [74] BINIAK, Stanislaw, et al. The characterization of activated carbons with oxygen and nitrogen surface groups. *Carbon*, 1997, 35.12: 1799-1810.
- [75] DORI, Zvi; EISENBERG, Richard; GRAY, Harry B. Crystal and molecular structure of the five-coordinate complex dichloro-1, 1, 7, 7-tetraethyldiethylenetriaminecobalt (II). *Inorganic Chemistry*, 1967, 6.3: 483-486.
- [76] BABA, Kamal, et al. Conductive Directly Fused Poly (Porphyrin) Coatings by Oxidative Chemical Vapour Deposition–From Single-to Triple-Fused. *European Journal of Organic Chemistry*, 2019, 2019.13: 2368-2375.

BIBLIOGRAPHY

- [77] WANG, Haibo; MAIYALAGAN, Thandavarayan; WANG, Xin. Review on recent progress in nitrogen-doped graphene: synthesis, characterization, and its potential applications. *AcS catalysis*, 2012, 2.5: 781-794.

5. Attachments

5.1. Synthesis

Compound (1a)

[Co(trenb)(N₃)]Cl was prepared as described in the literature [61]. 1 mmol of the ligand tris[benzyl(amino)ethyl]amine was dissolved in 10 ml of methanol. To the stirring solution of ligand was dropwise added a solution of 1 mmol of CoCl₂·6H₂O in 10 ml of methanol. To the stirring solution was added 1 mmol of NaN₃ in 5 ml of methanol. The stirring green solution was refluxed overnight than filtered and left to crystalize. Good quality crystals suitable for X-ray experiment were obtained by slow diffusion of diethylether after two weeks.

Analytical characterization: [Co(trenb)(N₃)]Cl (C₂₇H₃₆Cl₁CoN₇, M_r = 553.01)

Calculated composition: C: 58.64; H: 6.56; N: 17.73; Experimental data: C: 58.48; H: 6.62; N: 17.33.

Infrared spectroscopy: selected characteristic IR vibrations (cm⁻¹): 3155, 3077, 3031, 2881, 2867, 2055.

Compound (1b)

[Co(trenb)(NCS)]Cl was synthesized similarly to [Co(trenb)(N₃)]Cl with a change in the last step of synthesis where was used 1 mmol of a corresponding salt KNCS dissolved in 5 ml of methanol and added to the stirring solution. The solution was refluxed overnight, filtered and left to crystalize. Good quality crystals suitable for X-ray experiment were obtained by slow diffusion of diethylether after two weeks.

Analytical characterization: Co(trenb)(NCS)]Cl (C₂₈H₃₆ClCoN₅S, M_r = 569.07)

Calculated composition: C: 58.18; H: 6.45; N: 12.11; Experimental data: C: 58.05; H: 6.23; N: 12.05. Selected characteristic

Infrared spectroscopy: selected characteristic IR vibrations (cm⁻¹): 3167, 3087, 3026, 2878, 2886, 2054.

Compound (2a)

[Co(salapi)₂] was prepared as described in the literature [69]. To the solution of 2-amino-6methylpyridine (4.62 mmol, 500 mg) in 50 mL of methanol 565 mg of salicylaldehyde (4.62 mmol) was added. The solution was heated to 50°C, and then, 550 mg of CoCl₂·6H₂O (2,31 mmol) was added and after five minutes 468 mg of triethylamine (4,62 mmol) was added. The brown-orange solution was refluxed for 30 minutes and by filtration 142 mg of red-orange microcrystalline powder was obtained. Finally, 559 mg of X-ray quality monocrystals were obtained by slow diffusion of Et₂O into filtrate after one day. (Yield = 63 %).

Mw = 481.4258 g/mol Analytical characterization: [Co(salapi)₂] (C₂₆H₂₂CoN₄O₂)

Calculated composition: C, 64.87; H, 4.61; N, 11.64; Experimental data: C, 64.76; H, 4.59; N, 11.73.

Infrared spectroscopy (cm⁻¹): 395w, 460w, 502w, 544w, 605w, 727m, 753m, 786m, 812w, 844w, 911w, 940w, 980w, 1033w, 1096w, 1122w, 1140s, 1182m, 1215w, 1229w,

5.2. VSM MEASUREMENTS

1285w, 1331m, 1353w, 1385m, 1434s, 1457w, 1522s, 1564m, 1588m, 1603s, 2919w, 3017w, 3050w.

Compound (2b)

The same procedure was followed for complex (2a), by using corresponding equivalence of 5-methylsalicylaldehyde in place of salicylaldehyde to obtain orange X-ray quality crystals. (Yield = 58 %).

Mw = 509.480 g/mol Analytical characterization: [Co(mesalapi)₂] (C₂₈H₂₆CoN₄O₂)
Calculated composition: C, 66.01; H, 5.14; N, 11.00%; Experimental data: C, 65.75; H, 5.12; N, 10.98.

Infrared spectroscopy (cm⁻¹): 390w, 465w, 481w, 514w, 546w, 578w, 729w, 747w, 784m, 824w, 942w, 980w, 1020w, 1135m, 1150m, 1170w, 1202w, 1248w, 1323w, 1381s, 1425s, 1447s, 1520s, 1565m, 1589s, 1602m, 2859w, 2914w, 2995w, 3038w.

Compound (3a)

[Co(me₅dien)Cl₂] was synthesized identically to [Co(et₄dien)Cl₂], only instead of 1,1,7,7 – tetraethyldiethylenetriamine was used 1,1,4,7,7 – pentamethyldiethylenetriamine. The ligand was mixed with CoCl₂·6H₂O forming dark-blue solution. The solution was stirred and refluxed overnight forming microcrystalline powder. The solution was filtered and good quality crystals suitable for X-ray experiment were obtained by slow diffusion of diethylether after a week.

Analytical characterization: [Co(Me₅dien)Cl₂] (C₉H₂₃Cl₂CoN₃, M_r = 303.14)

Calculated composition: C: 35.66; H: 7.65; N: 13.86; experimental data: C: 36.14; H: 8.54; N: 13.79.

Compound (3b)

[Co(et₅dien)Cl₂] was prepared according to literature [75]. 1 mmol of the ligand 1,1,7,7 – tetraethyldiethylenetriamine was dissolved in 10 ml of methanol and 1 mmol of CoCl₂·6H₂O in 10 ml of methanol was added. Resulting dark-purple solution was refluxed overnight, filtered and left to crystallize. Very good quality crystals in form of purple needles suitable for X-ray experiment were obtained by slow diffusion of diethylether after a week.

Analytical characterization: [Co(Et₄dien)Cl₂] (C₁₂H₂₉Cl₂CoN₃, M_r = 505.03)

Calculated composition: C: 41.75; H: 8.47; N: 12.17; Experimental data: C: 41.53; H: 8.31; N: 12.04.

Selected characteristic IR vibrations (c⁻¹): 3243, 2965, 2928, 2881.

5.2. VSM measurements

By measuring and fitting the VSM data, the magnetic properties of (1a) were determined as $g_{\text{iso}} = 2.24$ $D = -5.64 \text{ cm}^{-1}$ and $E/D = 0$.

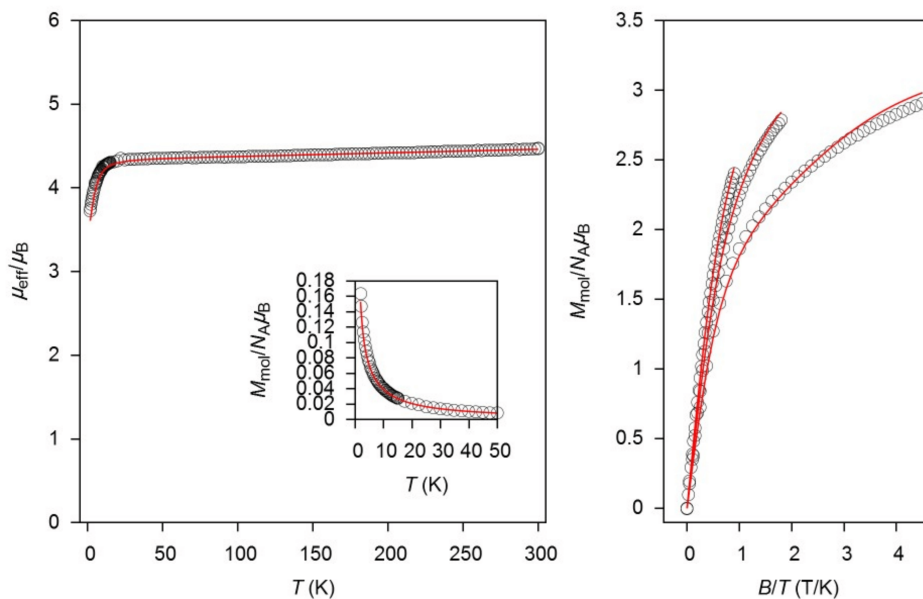


Fig. 5.1: VSM measurement of the bulk (1a). Black circles represent experimental data, and red lines represent fitting.

By measuring and fitting the VSM data, the magnetic properties of (1b) were determined as $g_{\text{iso}} = 2.192$, $D = -1.5 \text{ cm}^{-1}$ and $E/D = 0.33$.

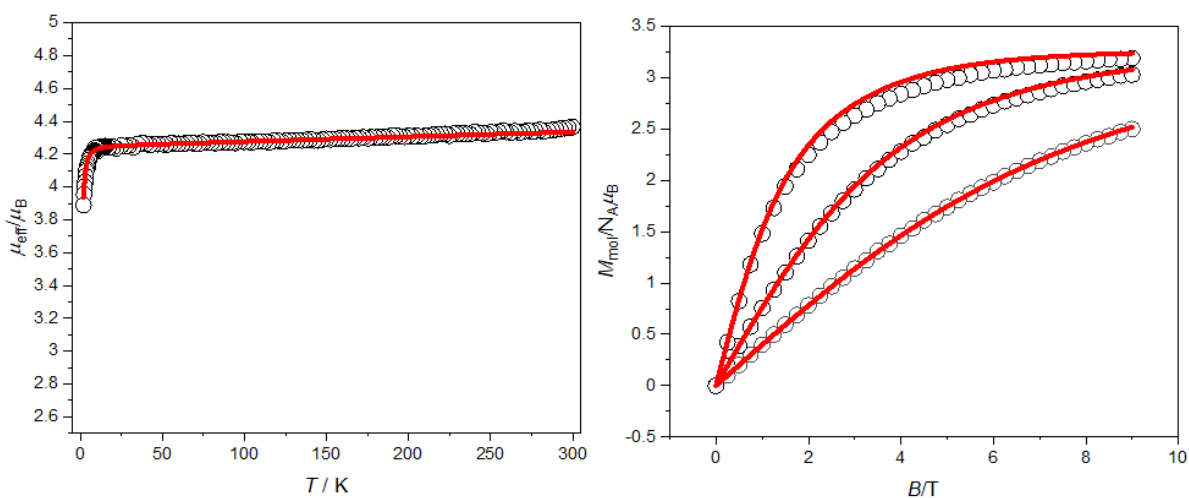


Fig. 5.2: VSM measurement of the bulk (1b). Black circles represent experimental data, and red lines represent fitting.

By measuring and fitting the VSM data, the magnetic properties of (2a) were determined as $g_{\text{iso}} = 2.20$, $D = -19.2 \text{ cm}^{-1}$ and $E/D = 0.079$.

5.2. VSM MEASUREMENTS

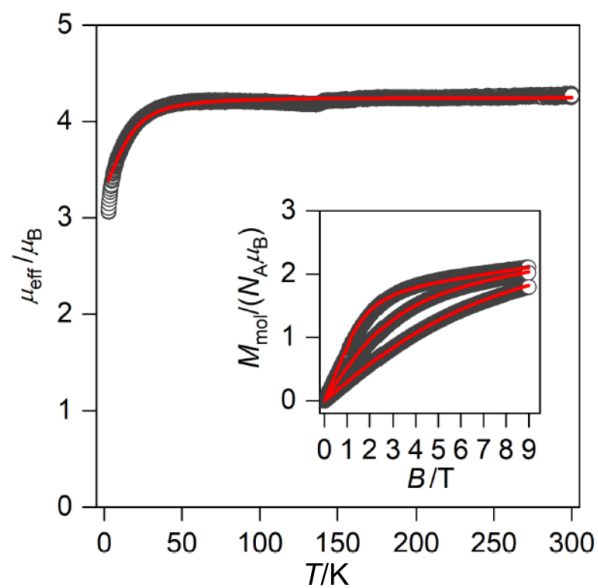


Fig. 5.3: VSM measurement of the bulk (2a). Black circles represent experimental data, and red lines represent fitting.

By measuring and fitting the VSM data, the magnetic properties of (3a) were determined as $g_{\text{iso}} = 2.166$, $D = -20.60 \text{ cm}^{-1}$ and $E/D = 0.23$.

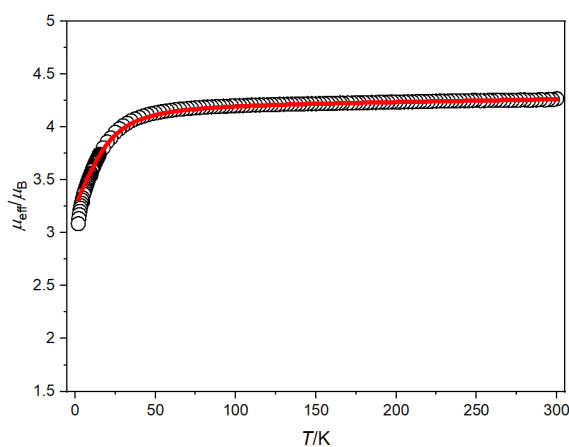


Fig. 5.4: VSM measurement of the bulk (3a). Black circles represent experimental data, and red lines represent fitting.

By measuring and fitting the VSM data, the magnetic properties of (3b) were determined as $g_{\text{iso}} = 2.32$, $D = -13.0 \text{ cm}^{-1}$ and $E/D = 0.26$.

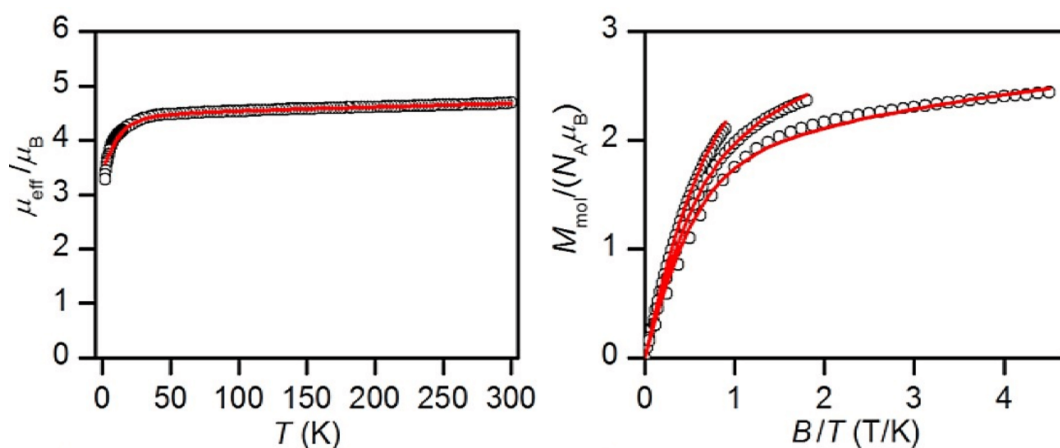


Fig. 5.5: VSM measurement of the bulk (3b). Black circles represent experimental data, and red lines represent fitting.

5.3. TGA measurements

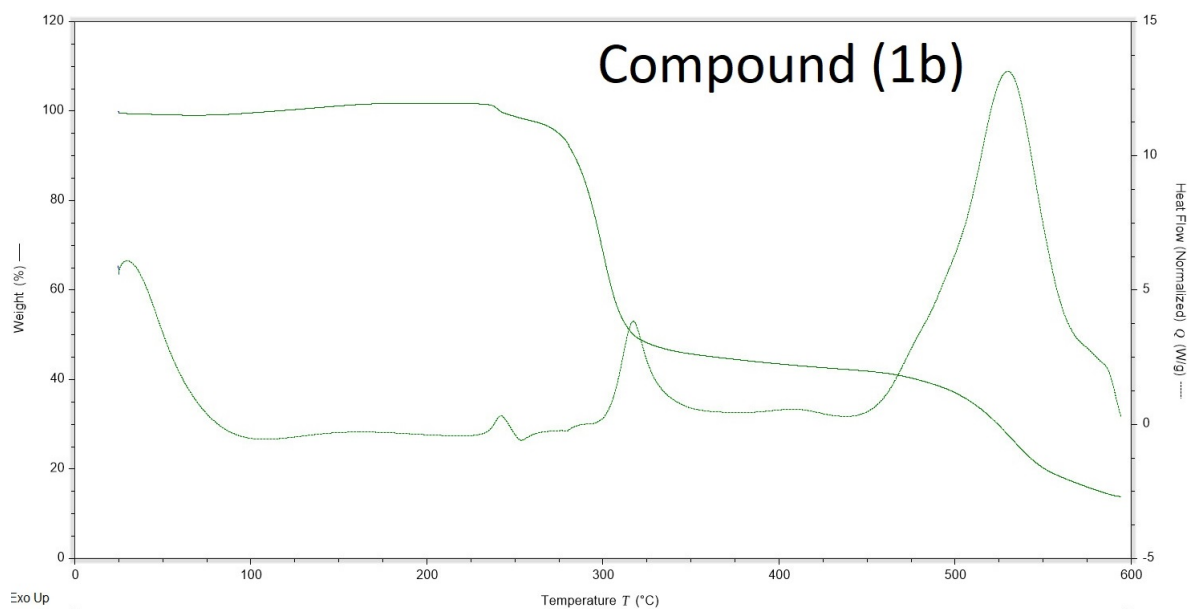


Fig. 5.6: TGA measurement of the compound (1b).

5.3. TGA MEASUREMENTS

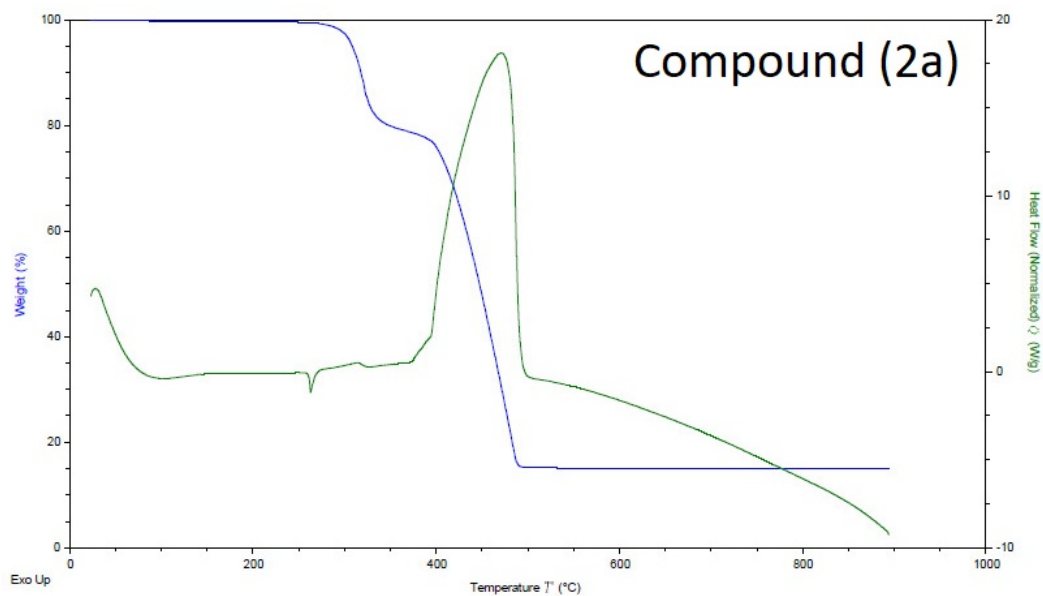


Fig. 5.7: TGA measurement of the compound (2a).

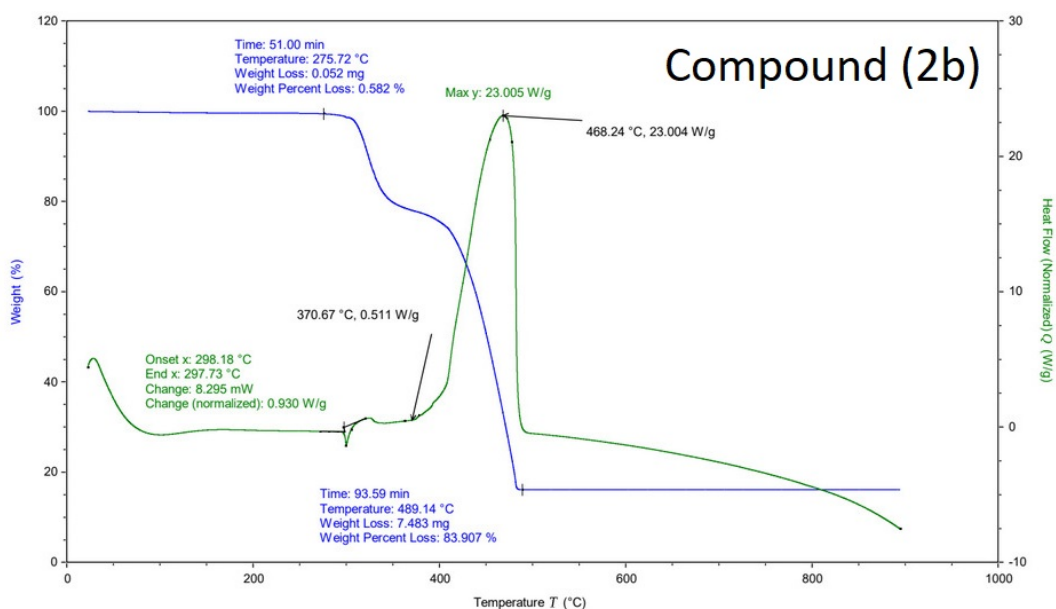


Fig. 5.8: TGA measurement of the compound (2b).

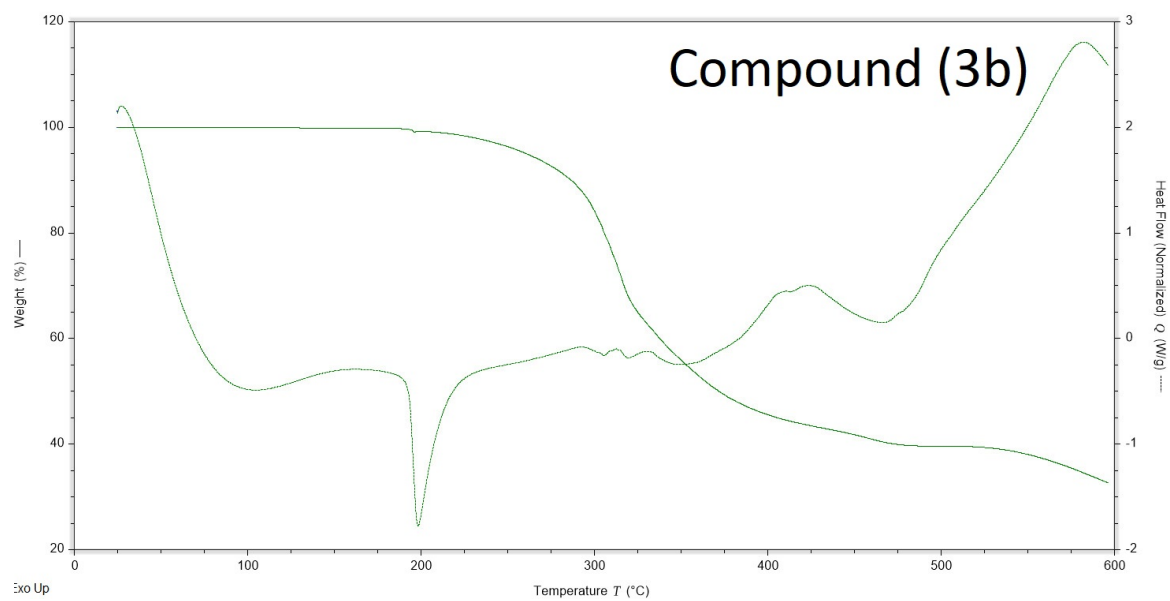


Fig. 5.9: TGA measurement of the compound (3b).